Modelling electromechanical properties of 2D materials and heterostructures

A thesis submitted for the degree of Doctor of Philosophy

School of Physics

Trinity College Dublin

March 2024

Nina Georgoulea

Declaration of Authorship

I declare that this thesis has not been submitted as an exercise for a degree at this or any other university and it is entirely my own work.

I agree to deposit this thesis in the University's open access institutional repository or allow the Library to do so on my behalf, subject to Irish Copyright Legislation and Trinity College Library conditions of use and acknowledgement.

I consent to the examiner retaining a copy of the thesis beyond the examining period, should they so wish (EU GDPR May 2018).

Abstract

Strain, both naturally occurring and deliberately engineered, can have a considerable effect on the structural, electronic, and transport properties of 2D and layered materials. Uniaxial or biaxial heterostrain (i.e. different strain applied to different layers) modifies the stacking arrangement of bilayer graphene (BLG) forming Moiré superlattices. This subsequently influences the electronic structure and the transport properties of the bilayer. We performed Density Functional Theory (DFT) calculations to investigate the interplay between heterostrain and the resulting stacking in BLG. We found that above a critical strain of 1%, it is energetically favorable for the free layer to be unstrained, indicating a transition between uniform AB stacking and non-uniform mixed stacking. This suggests that even small levels of strain can provide a platform to reversibly engineer stacking order and Moiré features in BLGs, providing a viable alternative to twistronics to tune the stacking order of the system, and consequently its properties.

The domain walls between the AB and BA-stacked gapped BLG have garnered intense interest, as they host topologically protected, valley-polarised transport channels. The introduction of a twist angle θ between the bilayers and the associated formation of a Moiré pattern has been the dominant method used to study these topological channels, but heterostrain can also give rise to similar stacking domains and interfaces. We theoretically investigated the electronic structure of a uniaxially heterostrained BLG. We discussed the formation and evolution of interface localized channels in the one-dimensional Moiré pattern that emerges due to the different stacking registries between the two layers. We found that a uniform heterostrain is not sufficient to create one-dimensional topological channels in biased BLG. Instead, using a simple model to account for the in-plane atomic reconstruction driven by the changing stacking registry, we showed that the resulting ex-

panded Bernal-stacked domains and sharper interfaces are required for robust topological interfaces to emerge. These states are highly localized in the AA- or SP-stacked interface regions and exhibit differences in their layer and sublattice distribution depending on the interface stacking. We conclude that heterostrain can be used as a mechanism to tune the presence and distribution of topological channels in gapped BLG systems, complementary to the field of twistronics.

We then investigated the effect of the Poisson contraction, which can occur with the application of uniaxial heterostrain for heterostrained BLG. In this initial investigation, we do not include the effect of atomic relaxation on the electronic and transport properties of the interface channels. The inclusion of Poisson contraction ν with the application of heterostrain leads to the formation of 2D Moiré superlattices, similar to the ones created in twisted BLG. For low energies, the states in the AA-stacked regions are highly localized, whereas the SP-stacked regions host states that form a network throughout the lattice (topological channels). Moreover, the SP-stacked interface channels occur over a range of energies (dispersive channels), but they do not have the expected pattern. We explained this, due to the fact that different strains are applied along x and y directions. The overall transmission has very low values due to the existence of the AB/BA-stacked gapped domains in heterostrained BLG with the application of large interlayer bias, compared to no bias. Consequently, heterostrained untwisted BLG is an alternative way to tune the electronic and transport properties of BLG, compared to twisted BLG, overcoming limitations relevant to achieving precise twist angle θ. In future work, we will extend this study for lower and larger values of heterostrain to investigate how the localization of states is affected. Also, we could study how transmission is modified by changing the value of heterostrain for this system, as similar studies have been done for twisted BLG.

Acknowledgements

During my Ph.D. I have received a lot of encouragement and support from many people. This work could not have been done without their help. First of all, I would like to give special thanks to my supervisors Dr. Stephen Power and Dr. Nuala Caffrey for all their support of my projects, their encouragement, and their kindness. Their guidance and fruitful comments are of significant importance for the completion of this work. I had the opportunity to work on many interesting projects concerning physics and use different theoretical tools. Also, I would like to thank my co-supervisor Prof. Stefano Sanvito, for his useful feedback concerning my work and his eagerness to help whenever I needed it.

I am grateful for the help and support that I received from Dr. Urvesh Patil, Dr. Zahra Khatibi, and Dr. Meric Kucukbas during my Ph.D., as well as for their friendship. I would like also to thank my colleagues Dr. Simone Koecher, Lorien MacEnulty, Declan Nell, Andrew Burgess, Dr. Reena Gupta, Dr. Daniel Lambert, Eoin Butler, Luisa Tude, and Dr. Shardul Mukim for their company and our discussions concerning research.

I am grateful to the AMBER (Advanced Materials and Bioengineering Research) Center for their financial support during my Ph.D. studies and for making this work possible. I would like to thank the Trinity Center for High-Performance Computing (TCHPC) and the Irish Center for High-End Computing (ICHEC) and its administration for their computational facilities and for resolving relevant computational issues. Next, I would like to thank Ms. Stefania Negro who took care of my administrative work.

Last, I would like to thank deeply my parents for their encouragement and support during my Ph.D. studies.

Contents

Chapter 1 Introduction

1.1 Properties of 2D materials and fabrication

Two-dimensional (2D) materials consist of single or few-layer atoms and have many applications, thanks to their unique electromechanical, electrical, optical and piezoelectric properties compared to their 3D counterparts. Monolayer graphene (MLG) is the first 2D material that was investigated. It is a one-atom-thick layer of graphite. Wallace investigated theoretically the electronic structure of MLG in 1947 [1] and this was later isolated from graphite in 2004 by Novoselov et al. [2]. Since then, other 2D materials have been fabricated, such as Transition Metal Dichalcogenides (TMDs), including MoS_2, $MoSe_2$, WS_2 and WSe_2, hexagonal Boron-Nitride (h-BN) and phosphorene.

2D materials host a wide range of physical properties. For example, graphene is a conductor [1], MoS_2 is a semiconductor [3] and h-BN is an insulator [4]. MLG exhibits unique mechanical properties with high in-plane stiffness and strength [2, 5–8].

Interlayer interactions can be tuned by changing the relative arrangement of atoms between the layers (stacking) when there is more than one layer. This allows a wide range of different behaviors to be observed, even in structures with multiple layers of the same material. For example, the Young modulus E_{Y}, which shows how easily a material can be stretched and deformed, for MLG is bigger than that of BLG [9]. Concerning the electronic properties, MLG is a conductor, whereas BLG and trilayer graphene with certain stackings have an electrically tunable band gap [10]. The band gap refers to an energy range in the electronic band structure near Fermi level E_{F}, with no electronic states. It is the energy difference between the highest occupied energy state of the valence band and the lowest

unoccupied state of the conduction band. There is also a tunable transport gap for bilayer and trilayer graphene with specific stackings, which does not exist for MLG [11, 12]. A transport gap is a gap in the transmission that occurs with the application of an electric field and it affects the transport of charge carriers (electrons or holes).

2D materials can be further combined to create heterostructures that can have different properties to their component layers due to interlayer interactions [13, 14]. For instance, the elastic moduli of bilayer heterostructures, such as graphene/MoS_2 and MoS_2/WS_2, are smaller than the sum of the moduli of the individual layers [15]. The electronic structure can vary as well. For example, there is a band gap for the heterostructures MLG/SnO/MLG and for the heterostructure SnO/MLG/SnO [16].

The stacking of 2D materials can be achieved experimentally using several different techniques, including metal-assisted transfer methods, polymer-assisted transfer methods, wet transfer methods, and dry methods. For example, in the polymer-assisted transfer method, the micrometre-sized 2D crystals can be isolated on top of a polymer. The resulting 2D crystal can be put face down onto a chosen target and then the film can be removed or dissolved. The same procedure can be repeated several times until the desired stacking is achieved [17]. It is possible to place different 2D materials over each other with micrometer accuracy. This can be done with micromanipulators.

Novoselov et al. used mechanical exfoliation in bulk graphite for the production of monolayer graphene [2], but this technique has relatively low efficiency and the samples that are produced are low in size. Other experimental techniques have been used for the production of 2D materials since then, like Epitaxial Growth, Chemical Vapour Deposition (CVD) [18–21] and Liquid Phase Exfoliation (LPE) [22–24]. In the CVD method, the precursors react with the substrate or decompose on the substrate and produce the desired deposit. The substrate is the base material on which a material is deposited for its fabrication. A subclass of CVD is atomic layer deposition. The CVD method produces large area monolayers, but there are some defects and there is also the requirement for high temperatures, such as 650°C [25]. The best experimental technique so far for the production of 2D materials is LPE, which is a very easy method, low-cost, and environmentally friendly. The same techniques have been used for the production of other 2D materials [26–28].

1.2 Graphene

Graphene is a very promising 2D material. It is the strongest material that has been discovered so far (E_{Y}=2.4$\pm$0.4 TPa) [29], it has very high electron mobility ($\sim$2.5$\cdot 10^5$cm^2 V^{-1}s^{-1}) [30] and it is very flexible material (bending rigidity $\sim$1.44 eV) [31]. It has other tremendous properties, like high charge carrier mobility, ultrahigh specific surface area, and high optical transmittance [32–36]. Consequently, it could have applications in supercapacitors, transistors, solar cells, resonators, batteries, and energy harvesting devices [37–39].

1.2.1 Structure of monolayer graphene

In graphene carbon atoms are structured in a honeycomb lattice periodically. In this structure, there are two types of bonds, which are sp^2 hybridized. The s, p_x and p_y orbitals are combined to form the in-plane σ bonding and the σ^* antibonding orbitals. The σ bonds are strong covalent bonds that determine the energetic stability and the elastic properties of graphene. Lateral interactions between the p_z orbitals form localized π bonding and π^* antibonding orbitals. Figure 1.1 (a) shows the σ and π orbitals in graphene. Figure 1.1 (b) shows the energetics of σ, σ^*, π and π^* carbon valence orbitals. The π and π^* states are close to Fermi level E_{F}. The lattice structure of graphene is hexagonal and consists of two sublattices, A and B. There are two atoms in the unit cell of graphene that belong to different sublattices respectively. The unit cell is the smallest part of the lattice structure, which is repeated in real space. Figure 1.1 (c) shows the hexagonal lattice structure of graphene in real space and (d) in reciprocal space. The shaded area in Figure 1.1 (d) corresponds to the First Brillouin Zone (BZ).

Figure 1.1 (c) shows the primitive lattice vectors $\mathbf{a}_1$ and $\mathbf{a}_2$ of graphene in real space and Figure 1.1 (d) shows the reciprocal lattice vectors $\mathbf{b}_1$ and $\mathbf{b}_2$:

$$\mathbf{a}_1 = a_{\text{const}}\big(\tfrac{\sqrt{3}}{2}, \tfrac{1}{2}, 0\big), \quad \mathbf{a}_2 = a_{\text{const}}\big(\tfrac{\sqrt{3}}{2}, -\tfrac{1}{2}, 0\big),$$

$$\mathbf{b}_1 = b\big(\tfrac{1}{2}, \tfrac{\sqrt{3}}{2}, 0\big), \quad \mathbf{b}_2 = b\big(\tfrac{1}{2}, -\tfrac{\sqrt{3}}{2}, 0\big) \tag{1.1}$$

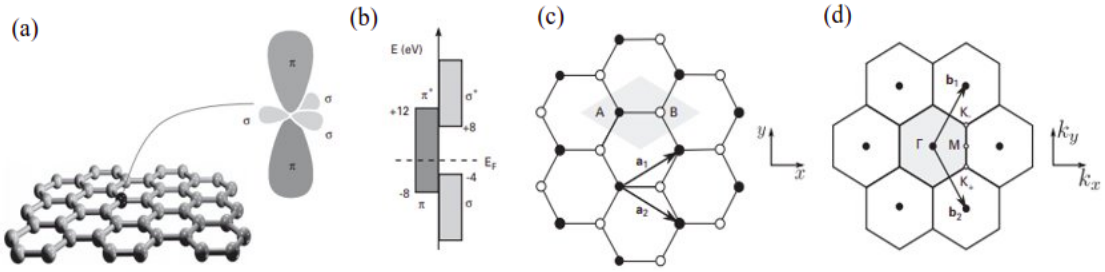

Figure 1.1: *(a) The σ and π orbitals in graphene. (b) The energetics of σ, σ^*, π and π^* states. (c) The hexagonal lattice structure of graphene in real space. (d) The hexagonal lattice structure of graphene in reciprocal space. Figures (a)–(d) adapted from [40].*

where a_{const} is the value of graphene's lattice constant and $b = \frac{4\pi}{a_{\text{const}}\sqrt{3}}$. The high symmetry points for unstrained graphene shown in Figure 1.1 (d) are the following:

$$\Gamma = (0,0,0), \quad K_+ = K = \tfrac{4\pi}{3a_{\text{const}}}\big(\tfrac{\sqrt{3}}{2}, -\tfrac{1}{2}, 0\big),$$
$$K_- = K' = \tfrac{4\pi}{3a_{\text{const}}}\big(\tfrac{\sqrt{3}}{2}, \tfrac{1}{2}, 0\big), \quad M = \tfrac{2\pi}{\sqrt{3}a_{\text{const}}}(1,0,0) \tag{1.2}$$

1.2.2 Stackings of bilayer graphene

Two MLG layers can be stacked to form bilayer graphene (BLG) [10]. In the ground state AB stacking, half of the carbon atoms on each layer are directly above the center of a hexagon on the other layer and the other half are directly on top of another carbon atom [41, 42] (Figure 1.2 (a)). There are two equivalent possibilities, AB and BA stackings, depending on which sublattices from each layer form dimers (when an atom sits on top of an atom from the other layer). The least favorable stacking possibility is AA stacking, where the two layers are perfectly aligned and each atom sits on top of an atom from the same sublattice in the other layer (Figure 1.2 (b)). Between the low-energy AB and high-energy AA extremes lie a range of stacking options which can be achieved by varying the amount and direction by which one layer is shifted relative to the other. The sublattice symmetric SP (or Saddle Point) stacking, shown in Figure 1.2 (c) is of interest in this work as it occurs for shifts halfway between AB and BA stackings, and corresponds to a local energy maximum along this direction. The total energy differences for the shifted stackings E and the ground state energy of AB stacking E_{AB} for different initial stackings (AA or

AB) and shifts along different directions (AC or ZZ) are shown in Figure 1.3 as a function of the relevant shifts. Twisted BLG (tBLG) is when one of the two layers of BLG is rotated by a twist angle θ (Figure 1.2 (d)).

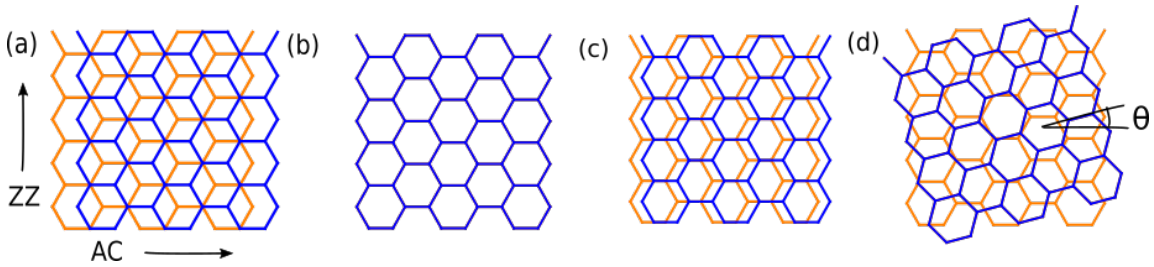

Figure 1.2: *Atomic structure of (a) AB-stacked BLG, (b) AA-stacked BLG, (c) SP-stacked BLG, and (d) tBLG with twist angle θ. In (a) the high symmetry directions ZZ and AC are shown.*

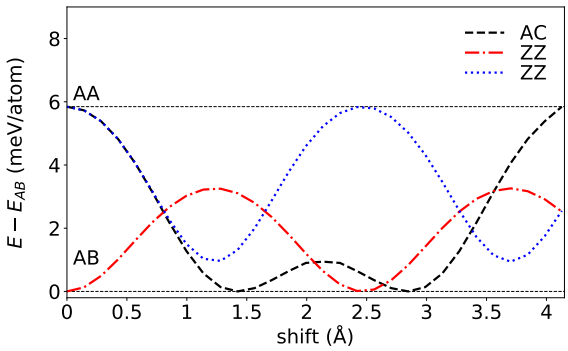

Figure 1.3: *Energy difference $E - E_{\mathrm{AB}}$ per atom as a function of the relative shift between layers in BLG for different initial stackings (AA and AB stackings). Shifts along both ZZ and AC directions are shown.*

1.2.3 Electronic, topological and transport properties of graphene

MLG has interesting electronic properties because it is a zero-gap semiconductor [43]. It has linear bands near Fermi level E_{F} at the K and K' points (Figure 1.4) and it hosts a so-called Dirac cone there. This is the reason why the K and K' points are called valleys. The Dirac cone, due to its linear bands, exhibits high electron mobility, which means that electrons can move faster with the application of an electric field. This way energy loss is reduced, which is desirable in devices. Also, the Dirac cone is topologically protected,

which means that it is robust against scattering effects and perturbations. This stems from the topology of the material's band structure. Thus, improved performance is achieved.

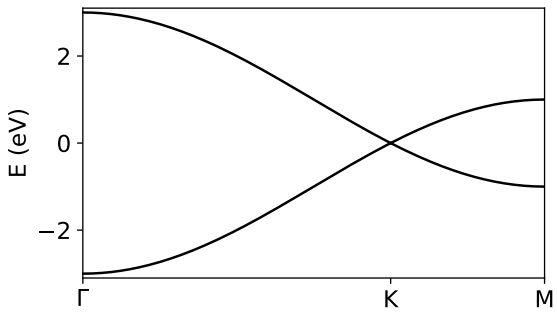

Figure 1.4: *Electronic band structure of MLG along the high symmetry points* $\Gamma \rightarrow K \rightarrow M$.

However, when there are two or more graphene layers, the electronic properties depend on the relevant stacking. For instance, AB-stacked BLG has parabolic electronic bands (Figure 1.5 (b)), whereas the bands of AA-stacked (Figure 1.5 (a)) and SP-stacked BLGs (Figure 1.5 (c)) are linear near Fermi level E_{F}. The electronic band structures in Figures 1.5 (a)–(c) are near high-symmetry point K along k_x-direction and for k_y=0. For $k_y \neq$0 AA-stacked BLG has more than two crossings at E=0. The linear bands lead to higher mobility compared to the parabolic bands. Also, the Density of States in the case of linear bands is almost constant near Fermi level E_{F}, which affects the electrical conductivity and thus transport properties. In the case of parabolic bands, the Density of States changes continuously with the energy E near Fermi level E_{F}. The electronic structure for various stackings of BLG has been investigated both theoretically [44, 45] and experimentally [46] by performing Angle-resolved photoemission spectroscopy (ARPES) measurements [47]. ARPES is an experimental technique to probe the allowed energies and momenta of the electrons in a material and is mostly used for the electronic structure of 1D or 2D materials.

Concerning the BLGs, where one layer is allowed to slide ('shifted BLGs'), DFT calculations showed that for perfect AA and AB/BA stacking, there is no band gap along the high symmetric lines in BZ, while for other stackings there is a pseudo band gap [48]. This is because the band crossing points move away from the high symmetric lines for these stackings. The change in the electronic structure influences the topology of the Fermi surface of low energy bands in BLG (Lifshitz transition) [49].

Concerning the transport properties of shifted BLGs, DFT studies showed that sliding was found not to affect the transmission for low energies, but for larger (above 1.23 eV and below -1.9 eV) it does [48]. For large energies, there is a big change in the transmission predicted for AA initial stacking and sliding along AC direction and for sliding and AB initial stacking and sliding along ZZ direction. For AA initial stacking and sliding along the ZZ direction, the transmission first increases in the energy range from 1.5 eV to 2.4 eV and from -2.5 eV to -1 eV. Beyond this energy range, the transmission value is below this of AA stacking. Also, they found that transmission for AB initial stacking and sliding along the ZZ direction is lower than the transmission for AA initial stacking and sliding along the ZZ direction. Thus, manipulating the stacking of a bilayer is a powerful tool to tune its electronic and transport behavior.

The application of interlayer bias has an effect on the electronic structure. Interlayer bias occurs when there are different potentials on each layer. It is possible experimentally by depositing metal electrodes on the top and bottom layer of 2D layered materials, which allows the application of interlayer bias. The electronic structure of BLG, depending on its stacking, is very different under the application of large interlayer bias. There is a band gap opening proportional to the relevant bias for AB/BA stacking (Figure 1.5 (e)), while the AA-stacked (Figure 1.5 (d)) and the SP-stacked systems remain semimetallic (Figure 1.5 (f)).

The electronic structure of gated BLGs has been investigated theoretically with Tight-Binding (TB) calculations [50] and DFT calculations [45, 51]. Experimentally, AB-stacked BLG has been grown on SiC(0001) substrate, which induces doping in BLG due to the substrate [10, 52]. This way, the carrier concentration was adjusted on each layer and there were changes in the Coulomb potential (interlayer bias) that created a small band gap with ARPES measurements. The gaps opened by an interlayer bias in AB- and BA-stacked BLGs are equal in magnitude, but are topologically non-equivalent, as continuum-model calculations showed for BLG [53] and for tBLG [54]. This means that the valley Chern number has opposite signs for AB- and BA-stacked BLGs respectively. However, for tBLG, the application of an external electric field does not lead to a band gap opening, according to theoretical studies [55].

Chern number is an integer number, which is related to the topology of the electronic bands. It is defined as the integral of the Berry curvature over the Brillouin zone, $C = \frac{1}{2\pi}\int \Omega(\mathbf{k})d\mathbf{k}$, where $\Omega(\mathbf{k})$ is the Berry curvature. Berry curvature is the curvature of a vector and is defined as $\Omega(\mathbf{k}) = \mathrm{Im}\langle\Psi|\boldsymbol{\nabla}_{\boldsymbol{k}} \times [i^{-1}\langle\boldsymbol{\nabla}_{\mathbf{k}}H|\Psi]\,|\Psi\rangle$, where Ψ is the wavefunction of the system and i is the imaginary number. The Chern number is equivalent to finding the 'flux' of the Berry curvature through the entire surface of the Brillouin Zone. When the Chern number is zero for a system, the system is a trivial insulator; if it is non zero, it is a topological (non-trivial) insulator. This is a gapped system with non-trivial edge states. When the integral is restricted to regions around each valley, then the 'valley Chern number' is the difference between the integral calculated at each valley.

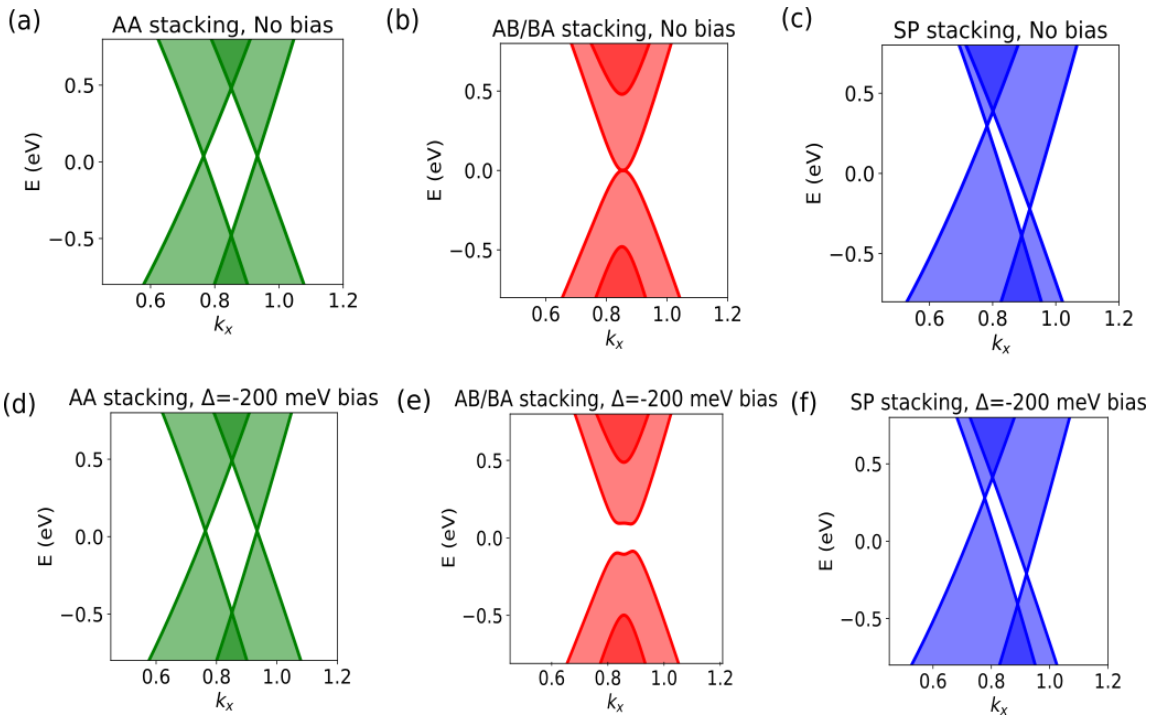

Figure 1.5: *Electronic band structure without bias for (a) AA-stacked, (b) AB/BA-stacked and (c) SP-stacked BLG and with the application of Δ=-200 meV interlayer bias for (d) AA-stacked, (e) AB/BA-stacked and (f) SP-stacked BLG respectively near K point along k_x-direction and k_y=0.*

1.2.4 Effect of strain in graphene

Strain can be intentionally created and controlled in graphene experimentally by depositing graphene on a substrate, due to the lattice mismatch. This was shown for a graphene flake deposited on top of an epoxy-based photoresist (SU8)/poly(methyl methacrylate) (PMMA) substrate with Raman spectroscopic measurements [56]. For no strain and for ε=0.3%, ε=0.6% and ε=1% strain applied on the graphene flake, the final distribution of strain was non-uniform, because of the lattice mismatch between the graphene flake and the substrate. Also, already strained graphene was grown on a h-BN substrate by the Molecular Beam Epitaxy method and MLG was found to be non-uniformly strained due to the lattice mismatch [57].

A flexible substrate can be used as well for the application of strain (Figure 1.6). Flexible substrate means that the substrate can be bent or stretched, which causes strain to be transferred to the layer that is in direct contact with the substrate. For example, studies showed for MLG, which was deposited on a flexible substrate, that tensile strain was transferred to MLG by bending [58] or stretching [59] the polyethylene terephthalate (PET) substrate or the polydimethylsiloxane (PDMS) substrate [60], shown by Raman measurements. It was found that strain up to 0.8% was transferred to MLG [59]. Strain transfer can also be achieved between the polymer substrate (PMMA) and the bottom layer of BLG when PMMA is bent, as Raman spectroscopic studies showed [61].

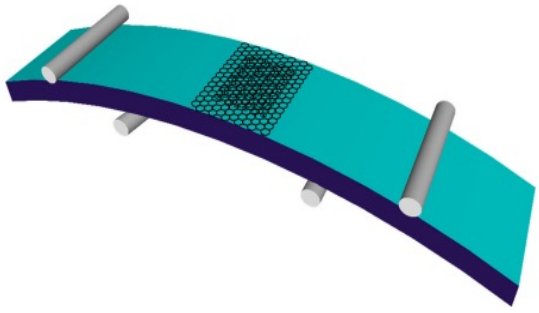

Figure 1.6: *Flexible substrate for applying uniaxial strain on the bottom layer of a bilayer system. Figure adapted from [61].*

The simplest type of strain is uniaxial strain, which is a strain applied only to one direction and can be applied experimentally by using a flexible substrate [58–61] (Figure 1.6).

Biaxial tensile strain is applied to two perpendicular directions and can be applied experimentally by bending a plastic substrate with a cruciform shape [62]. This way, biaxial strain was transferred to MLG or the bottom layer of multilayered graphene.

Strain can tune the electronic properties of graphene. For MLG there is theoretically the prediction that the application of more than 23% uniaxial strain along ZZ on MLG opens a small band gap [63]. However, this is not an efficient way to open a band gap, because 23% is too large a value of strain to be applied experimentally as graphene will fracture. Raman spectroscopic studies have shown that MLG deposited on a flexible substrate can experience strains up to 1.3%-1.8% [59, 64–67]. However, adding formvar resins as a buffer layer allows strains of up to 3.3% to be achieved [68], which is close to the theoretical limit for flexible substrates. Thus, other ways should be used to open a band gap in MLG. Strain can also affect the topology of Fermi surfaces of graphene for low energies, leading to Lifshitz transition, as TB calculations showed [69].

Also, the transport properties of graphene depend on the applied strain [70]. In experiments in which two electrodes and a back gate were used, a bias voltage was applied between them, and this way strain was applied to graphene (MLG or BLG). For MLG, the conductivity and its minimum value as a function of the gate voltage were slightly improved. However, for BLG conductivity was found to decrease by 10%-15%.

The properties of 2D multilayers can be tuned by applying different strain on each layer (heterostrain). Theoretical studies have been done for heterostrained BLG (hBLG), showing the strain transfer between the graphene layers. There is the possibility of commensurate-incommensurate transition in BLG with the one layer being stretched or compressed along the AC direction, shown by the Frenkel-Kontorova model and DFT calculations [71]. The Frenkel-Kontorova model is a theoretical model used for the study of 1D systems [72], but now is extended to 2D systems as well. It regards a chain of atoms or particles which are arranged in a periodic lattice potential, usually described by a sinusoidal or a periodic function. The atoms or particles in the chain interact with their nearest neighbours, through a potential energy function, which defines the interatomic or interparticle forces. There are variations of this model, such as with the inclusion of external forces or the inclusion of anharmonic potentials. The Frenkel-Kontorova model can be useful for

studying the dynamics and the crystal lattices near a dislocation (such as the application of heterostrain in BLG) where the arrangement of atoms changes periodicity. For example, this model could be used to determine the energetics of hBLG and to find the critical strain in the calculations (explained in Chapter 3). Additionally, the Frenkel-Kontorova could be used to relax the atomic positions of hBLG (explained in Chapter 4).

Heterostrain can be applied intentionally by placing a multilayer on a flexible substrate, which can be stretched or compressed. In Raman spectroscopic measurements uniaxial strain lower than 1% was applied to the polymer substrate PMMA and BLG was strained because it was deposited on this substrate [61]. It was found that the interfacial stress transfer between the substrate and the bottom layer of BLG was three to four times higher than the interlayer stress transfer between the two graphene layers. It is reasonable to expect that if the applied strain is sufficiently small, it will be entirely transferred to the second graphene layer, i.e., both layers will experience the same strain. However, for larger applied strains the second layer can exhibit a different strain profile. Raman spectroscopic measurements showed that for applied heterostrain on BLG, stacking is non-uniform anymore [66]. This provides some evidence for non-uniform stress distributions across the bilayer, but the threshold is unknown. Thus, the change of stacking affects the electronic, transport, and optical properties of BLG, as discussed in Subsection 1.2.3.

By applying heterostrain in BLG, is an alternative way to twistronics for engineering its stacking order. Twistronics is the field of physics that studies how the twist angle between adjacent layers of 2D materials affects their electronic properties. This is because the electronic properties depend on the relevant stacking of the combined 2D heterostructure (Subsection 1.2.3). Twistronics has applications in tuning the properties of 2D materials, due to the creation of Moiré domains (explained in Subsection 1.2.5). Twistronics can be related to other fields, like valleytronics or spintronics. Valleytronics is the field of physics, which focuses on the electronic properties of the relevant valleys formed in the band structures of 2D materials for their use in information processing and storage. Valleytronics is related to twistronics, because the Moiré pattern resulting from the twist angle can affect the electronic valleys in the relevant material. For example, in tBLG there is the formation of valley-dependent transport channels [53, 73]. Valleytronics has applications

in valley filters and diodes, where the flow of the charge carrier is based on the valley indices. Spintronics on the other hand is the field of physics where the spin (intrinsic property of elementary particles, such as electrons) is used for the processing and storage of information. The spin of an electron can have two possible orientations, either 'up' or 'down'. Also, spintronics is related to twistronics, because the Moiré pattern resulting from the twist angle can modify the spin-orbit coupling, like in the twisted heterostructure graphene/TMD [74].

There are also other ways to tune the electronic and transport properties of BLG except for the application of strain, like the inclusion of Stone-Wales (SW) defects, single vacancy defects, multiple vacancy defects, line defects or adding carbon adatoms. For example, the SW defect, which is obtained when there is a rotation of two adjacent carbon atoms in graphene, resulting in the formation of a pentagon and a heptagon (Figure 1.7), can influence the electronic properties of BLG with and without the application of interlayer bias. DFT calculations showed for a SW on the one of the two layers of BLG there is a band gap of 0.1 eV at the K-valley point, while for perfect AB-stacked BLG there is no [75]. With the application of electric field (0.25 V/Å) for no defects there is a band gap of 0.45 eV and for a SW defect the band gap also increased (0.46 eV). Thus, the inclusion of a SW defect affects the electronic properties of BLG.

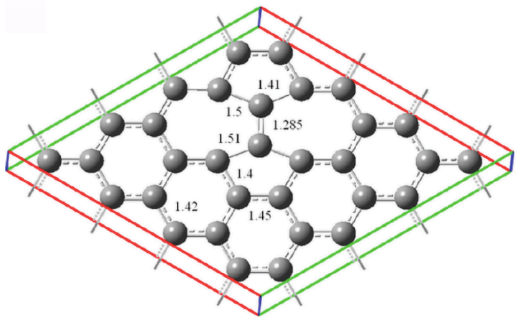

Figure 1.7: *MLG structure with a SW defect. Figure adapted from [75].*

1.2.5 Moiré superlattices

Moiré superlattices are the structures that arise when two or more layers with a slight mismatch in lattice constant or lattice orientation are stacked on top of each other. This

creates an interference pattern, which has larger periodicity. An example of Moiré superlattice that is created due to lattice mismatch is graphene/MoS_2 heterostructure, and its top and side views are depicted in Figure 1.8 (a) and (b) respectively. This is because graphene has lattice constant a_{const}=2.46 Å, while MoS_2 has lattice constant a_{const}=3.18 Å.

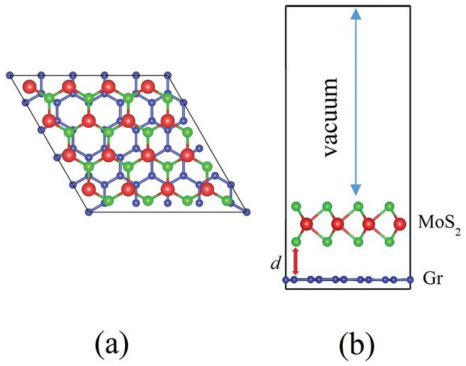

Figure 1.8: *(a) Top view and (b) side view of Moiré unit cell of graphene/MoS_2 heterostructure. Figures (a) and (b) adapted from [76].*

Examples of Moiré superlattices due to the lattice orientation are the twisted systems, like tBLG [77]. The smaller the twist angle, the bigger the Moiré pattern that arises, as shown in Figures 1.9 (a) and (b) that depicts structures of tBLG with twist angle θ=21.79° and θ=38.21° respectively. In Figures 1.9 (a) and (b), $\mathbf{L}_1$ and $\mathbf{L}_2$ are the primitive superlattice vectors for tBLGs.

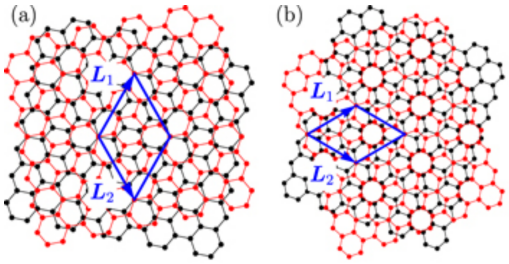

Figure 1.9: *Moiré structures of tBLG with twist angle (a) θ=21.79° and (b) θ=38.21°. Here, $\mathbf{L}_1$ and $\mathbf{L}_2$ are the primitive superlattice vectors for tBLGs. Figures (a) and (b) adapted from [77].*

In tBLG there is a Moiré pattern with periodic modulation of AA-, AB/BA-, and SP-stacked domains. The interfaces between AB- and BA-stacked domains form a triangular superlattice with AA-stacked vertices connected by SP-stacked edges (Figure 1.10). These transport channels are called networks of interface channels.

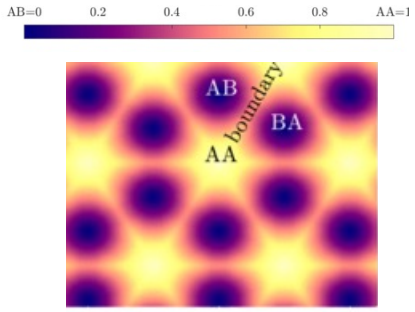

Figure 1.10: *Networks of interface channels ('boundary') and Moiré patterns in tBLG. Figure adapted from [78].*

Similar to the twist angle in tBLG, the application of heterostrain leads to the creation of Moiré superlattices. The smaller the twist angle and the application of heterostrain, the bigger the Moiré that arises. Figures 1.11 (a)–(c) show how the Moiré superlattices are modified for different heterostrain. They include the atomic structures for applied uniaxial heterostrain 10%, 20% and 30%, and the length of the Moiré pattern is y_{cell}=27.06 Å, y_{cell}=14.76 Å and y_{cell}=9.84 Å respectively (dashed boxes). The dashed circles highlight the two extremes of energy: AB-stacked and 'Shifted' regions, which are also shown in Figure 1.11 (a). For some rare cases though the application of heterostrain or the twist angle between the two layers may lead to stackings that do not have periodicity. These are called incommensurate stackings [79].

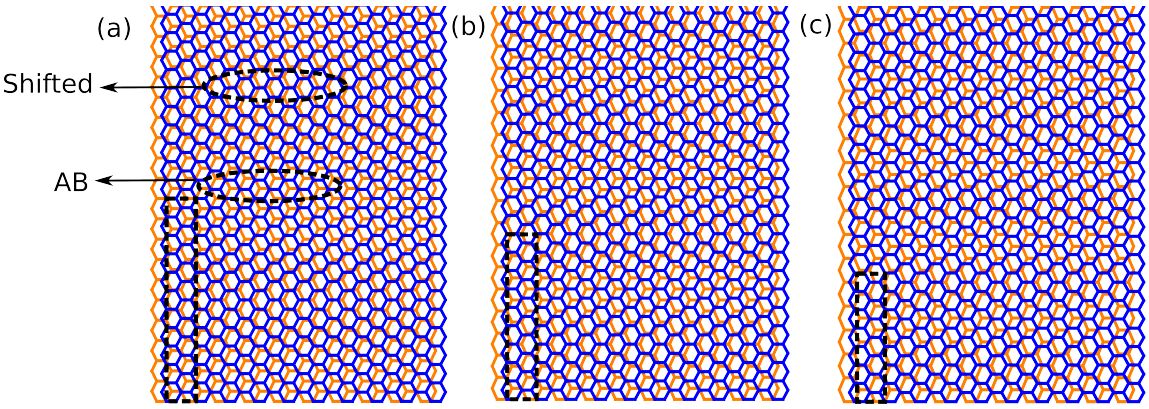

Figure 1.11: *hBLG with the relevant unit cells shown in dashed boxes with uniaxial strain applied on the bottom layer and relevant size of the unit cell along y-direction respectively (a) 10% and y_{cell}=27.06 Å, (b) 20% and y_{cell}=14.76 Å and (c) 30% and y_{cell}=9.84 Å. The AB-stacked and 'Shifted' regions that correspond to the two extremes of energy are shown as well, in dashed circles.*

In Moiré superlattices, the applied strain can be uniform and non-uniform. tBLG undergoes a spontaneous lattice in-plane relaxation, which leads to local strain. This has been shown theoretically, with continuum model calculations [80] and experimentally with the use of piezoresponse force microscopy, which locally measures the electromechanical surface deformations [81]. In tBLG with small twist angles, the AA-stacked domains are minimized, the AB/BA-stacked domains are maximized and the SP-stacked domains appear to be sharper after this in-plane relaxations [80–84, 84–88]. This is because the AA-stacked domains are not energetically favorable, while the AB/BA-stacked domains are (Figure 1.3).

These in-plane relaxations were overlooked until it was discovered that it was not possible to get agreement with experiments concerning the electronic properties. They affect the electronic band structure, for small twist angles θ<3° [81, 84, 86, 89–93] in low energies. For Magic-Angle tBLG, which has twist angle $\theta \sim$1.1° twist angle, there are flat bands close to Fermi level E_{F} [94, 95], only when relaxation is allowed [93]. The flat bands lead to enhanced DOS and correlated insulating states at half-filling. These flat bands also can lead to superconductivity, like in this case, which means that below a certain temperature, the material conducts electricity without resistance. Zero-resistance states were observed for Magic-Angle tBLG with critical temperature T_{c}=1.7 K.

We expect to have in-plane relaxation in hBLG, which grows AB/BA-stacked domains at the expense of AA- and SP-stacked interfaces. Atomistic and first-principles calculations for hBLG, that took into account the out-of-plane relaxation, showed the formation of flat electronic bands around the Fermi level E_{F} at values of strain approximately $\varepsilon \pm 1\%$ [96]. The calculations included both tensile and compressive uniaxial heterostrain, for strain range from -5% to +5%, and the out-of-plane relaxation was mostly useful for the compressive heterostrain, due to the rippling. Thus, both tBLG for small twist angles ($\theta \sim 1°$) and hBLG for small heterostrain ($\varepsilon \sim 1\%$) show interesting electronic properties, that can be investigated further. In particular, we extended the studies concerning the local electronic properties of hBLG for 1% tensile uniaxial heterostrain.

1.2.6 Topological interface channels in bilayer graphene

Interfaces are regions in which different materials meet or the same material with different orientations. Interfaces between AB- and BA-stacked domains occur in a number of systems. These interface channels when biased are called 'topological' because the AB- and BA-stacked domains have technically, different 'valley Chern' numbers, so different topological properties, give rise to interesting electronic and transport properties for these channels. Topological properties are directly related to the band structure of the investigated material and characterize the properties of the material's electronic states. Interfaces around domains with changing valley Chern number are topologically protected, if the valley index is conserved. This means that the electrons do not scatter from one valley to another.

The simplest example is a change in the stacking registry caused by a grain boundary in one of the layers. The grain boundary is the interface between two grains in a polycrystalline material. This type of system has already been investigated for BLG theoretically with TB calculations, by including a line of octagon and double-pentagon defects in one of the layers (Figure 1.12) [97]. Due to the grain boundary, there are flat bands around Fermi level E_F, and the states that belong to this boundary around this energy are found to be localized. Experimentally, MLG with distinguishable grain boundaries created by doping was deposited with the CVD method on an amorphous SiO_2 substrate [98]. With Raman spectroscopic measurements, the presence of local transport gaps was found.

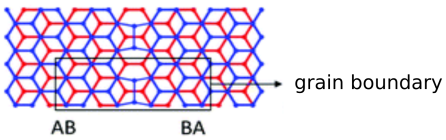

Figure 1.12: *Interface channel induced by a grain boundary in AB-stacked BLG. Figure adapted from [97].*

Topological interfaces between AB- and BA-stacked domains can be created as well when a relative twist angle is introduced between the layers, as for tBLG. The formation of interface states in tBLG, which are localized, is a topic of huge interest. With the applica-

tion of large enough interlayer bias, gapped (depleted electronically) and conducting states. The gapped states are in AB/BA-stacked domains and the conducting states are in the AA- and SP-stacked domains, as is expected with the application of interlayer bias (Figures 1.5 (d)–(f)). This was shown with continuum model and TB calculations [54, 89, 99, 100] for small twist angles (θ<1.5°) and applied interlayer bias lower than 200 meV. The same was shown from experimental studies, in which STM measurements and fast Fourier transform were used to the extracted topography [101] and with spectroscopic measurements [102]. The flow of the current can thus be controlled, because of the localized and gapped states. As a consequence, tBLG could be used as a transistor.

The interface channels in tBLG host topologically protected states. These are electronic states, which are robust and stable against perturbation due to the topology of the material. STM measurements and the application of a fast Fourier transform to the extracted topology showed the existence of topologically protected edge states in gated BLG [103]. Also, STS measurements with STM images showed that [102] and it was achieved enhanced LDOS in these domain walls (interface channels). This was found by calculating the contrast $C = [I(DW) - I(AB)]\,/I(AB)$, where $I(DW)$ and $I(AB)$ are the intensity of DOS for the domain wall and the BA-stacked region respectively, and it appears to be enhanced due to the existence of topologically-protected states.

These topological interface channels in tBLG are valley-polarised, with the application of interlayer bias [53, 73]. This means that they host counterpropagating states from each valley. The band structure of tBLG systems, there are pairs of bands, for each valley, K and K', which connect the otherwise gapped Dirac cones (Figure 1.13). These valleys have local minima and maxima in the energy dispersion and the electrons occupy states in these energy bands. Heterostrain can also break the stacking registry and give rise to different stacking domains and interfaces between them. We expect to have similar properties for the interface channels of hBLG, which have not been investigated yet.

The hBLG exhibits interfaces (stacking domains) that are strain solitons, as they separate two domains that are topologically opposite (AB- and BA-stacked domains) with the application of interlayer bias [104]. Solitons are localized waves, which maintain their shape and speed as they propagate. STEM images, simulations, and atomic structures

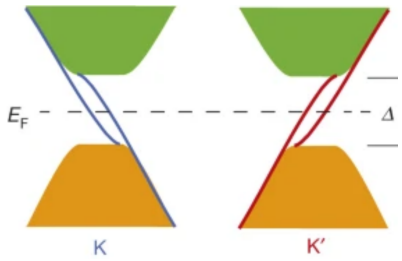

Figure 1.13: *Band structure for tBLG along the high symmetry points K and K'. Here, E_F denotes the Fermi level and Δ is the relevant band gap. Figure adapted from [73].*

showed these boundaries due to the application of shear uniaxial heterostrain (Figures 1.14 (A)–(C)) and tensile uniaxial heterostrain (Figures 1.14 (D)–(F)) respectively. The widths of the solitons depend on the competition between strain energy in the interface and the energy cost per unit length of the soliton due to the misalignment.

There are topological defects at these interface boundaries of hBLG for both tensile and shear uniaxial applied heterostrain, because the order parameter changes [104]. The order parameter is used to describe topological transitions and the topological defects arise due to the nontrivial topology.

Topological channels/interfaces can have multiple applications. For instance, the topological channels in tBLG could have applications in electronic devices, as they open conducting channels in a system that would otherwise have a bandgap (biased BLG) and this way carrier density can be controlled. Also, by leveraging the topological protection of edge/interface states in the topological channels, it could be feasible to engineer transistors, interconnects, and other electronic components. This way, the scattering is minimized, and thus energy efficiency is enhanced. Moreover, topological channels can ease valley-selective transport and manipulation, paving the way to valleytronic devices capable of encoding and processing information in the valley degree of freedom.

1.3 Aim of thesis

Inspired by the electronic and transport properties of tBLG due to the creation of topological channels, we examined the local and total electronic properties and the transport properties of hBLG. In Section 1.2 we explained the importance of studying these prop-

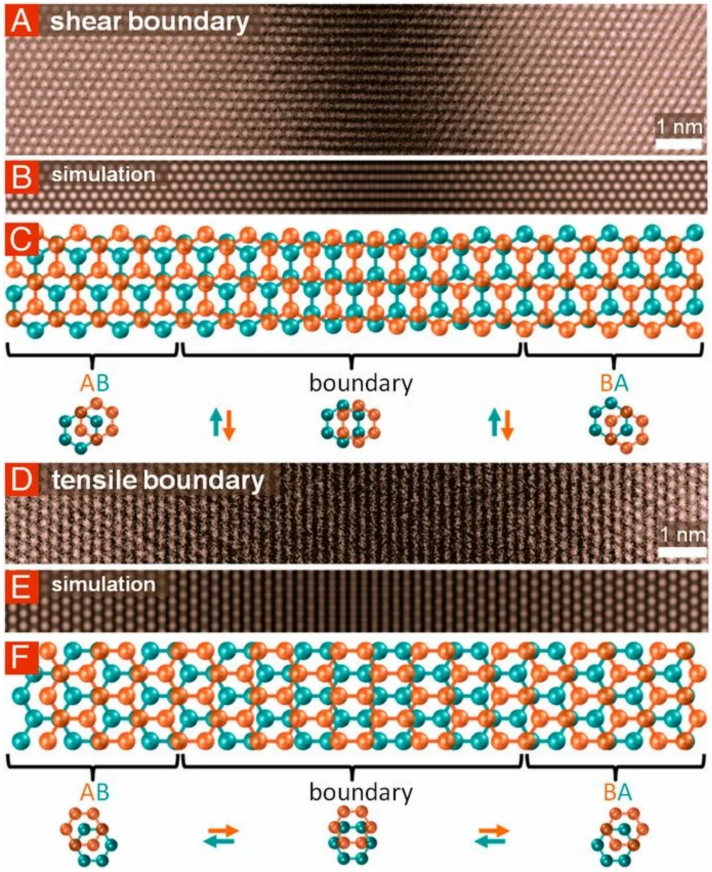

Figure 1.14: *(A)–(C) Shear boundary in BLG observed for STEM, simulations, and the atomic structure respectively. (D)–(F) Depict the same for tensile boundary. Figures (A)–(F) adapted from [104].*

erties for tBLG, and consequently for hBLG. First, we investigated the interplay between uniaxial heterostrain and stacking effects in BLG, in order to tune its stacking. Next, we investigated the local electronic properties of the topological channels for hBLG that are created due to heterostrain. Also, including the Poisson contraction ν in the calculations for hBLG, we investigated its electronic and transport properties. We concluded that hBLG could be used potentially as a transistor, because of the creation of these topological channels due to the application of heterostrain. For the study of these properties, we used a combination of computational and analytical methods.

The thesis is organized as follows:

- In Chapter 2 we included the mathematical and computational methods that were used for our calculations, concerning the energetics, electronic, and transport properties of hBLG.

- In Chapter 3 we introduced the study of strain-induced stacking transition in hBLG. In particular, we determined the interplay between strain and stacking, by straining one of the layers of BLG. We investigated the behavior of the top or else 'free' layer by performing Density Functional Theory calculations. We already mentioned in Section 1.2 that stacking is important, as it affects many properties, such as electronic and transport. Thus, it is useful to find ways to control the relevant stacking of the studied system. The application of strain could do this, but we need to understand fully the interplay between strain and stacking. We determined the critical strain required to be applied to one of the two layers of BLG which affects the stacking, considering the energetic cost of changing stacking and the cost of straining. We found that for $\varepsilon \sim$1% strain applied on the bottom layer stacking changes. This is an alternative way to twistronics for engineering stacking order, which affects the electronic, transport, and optical properties of BLG.

- In Chapter 4 we included the study of local electronic properties of heterostrained and biased BLG, by applying 1% strain only on the bottom layer and using TB calculations. There are studies so far which show that heterostrain tunes the stacking and the electronic properties of BLG, but there is not yet clear understanding of whether

interface channels, like those in tBLG, would emerge in hBLG and how robust they would be. To make the system more realistic we added the effect of relaxations in our calculations. We found that similar to tBLG, the states at the interface channels (AA- and SP-stacked regions) are highly localized. We found gapped and conducting (localized) states with the application of big enough interlayer bias and by adding the effect of relaxation. This is a way to tune the electronic properties of the system, by controlling the flow of the current. Thus, hBLG could be used as a transistor.

- Chapter 5 contains the results of transport and electronic properties (total and local) of heterostrained and biased BLG, after having included Poisson contraction ν. There are limited studies so far for hBLG with the inclusion of Poisson contraction for the electronic and transport properties of this system. The Moiré pattern created due to the heterostrain depends on many factors and affects the electronic and transport properties. There are studies for tBLG [54, 89, 99, 100] and we were motivated by this system. Because of the high computational cost, we used Recursive Green's Functions Method and we determined the Total Density of States, the Local Density of States, and the transmission, T, across hBLG. We concluded that the application of heterostrain is an alternative way to tune the electronic and transport properties of BLG, similar to twistronics.

- The results and conclusions of these calculations are summarised in Chapter 6, where possible extensions of this work are also discussed.

There are various experimental techniques to enable precise control over the twist angle θ between the two graphene layers. The first step is to grow MLG using the CVD method (Section 1.1), and then to be transferred onto a target substrate, using metal-assisted transfer methods, polymer-assisted transfer methods, wet transfer methods, and dry methods (Section 1.1). The specific alignment of the layers is achieved with optical microscopy techniques. Then, it can used for the fabrication of electronic or optoelectronic devices, by utilizing lithography techniques for the electrodes, contacts, and channels. These devices are characterized to evaluate their electronic properties, such as conductivity, carrier mobility, and quantum transport phenomena. For the fabrication of hBLG, the CVD

method is used again to grow the graphene layers. Heterostrain can be applied experimentally in BLG through direct mechanical deformation using nanomanipulation techniques, through a flexible substrate [61] (Subsection 1.2.4) or with the use of Atomic Force Microscopy [105]. Again, with lithographic techniques, hBLG can be processed in a device, to define structures like electrodes, contacts, or channels. Finally, measurements of resistance and conductivity are taken, to assess the performance of the relevant device. Concerning the stability of tBLG, it is sensitive to external factors, like air or humidity. Additionally, the stability of the twist angle, as well as the stability of the heterostrained system can be influenced by mechanical stress or temperature changes. One solution to prevent these defects is to encapsulate tBLG and hBLG with h-BN.

Chapter 2 Theoretical and computational methods

2.1 Introduction

The aim of this Chapter is to introduce the mathematical and computational methods that are used throughout this thesis. Section 2.2 details the basic concepts behind Density Functional Theory (DFT) followed by a description of its implementation in the VASP code. DFT is an *ab initio* method, which is quantitative, and in our studies, it is used to determine the energetics of BLG. Section 2.2 explains the Born-Oppenheimer approximation that has been used to approximate the Hamiltonian of the investigated system and this way the computational cost was reduced. It also contains the Hohenberg-Kohn theorems that solve exactly the Schrödinger equation for inhomogeneous systems of interacting electrons. Hohenberg-Kohn theorems evaluate correctly the ground state energy of the investigated system after the application of the Born-Oppenheimer approximation. DFT method is based on the functional of the electron density and this way the computational cost of the calculations, is only for N_{e} instead of $3N_{\mathrm{e}}$ interactions, as Kohn-Sham formulated. Furthermore, it contains some basic approximate functionals for the exchange-correlation term, and Subsection 2.2.5 includes the vdW functions that have to do with the interlayer interactions. DFT calculations were performed in VASP code, which is self-consistent. The practical implementation of these calculations in VASP is also discussed.

Section 2.3 introduces the TB Approximation used to implement the electronic and transport properties of BLG. It is a semi-empirical method which gives qualitative results.

It is explained how it can be applied to give the energy dispersion of MLG, for BLG and how strain can be included in the relevant calculations concerning the energy dispersion relations of both MLG and BLG.

Section 2.4 explains how Green's Functions (GFs) are used to solve problems with the use of the Dyson equation within the Recursive Green's Function regime and with the use of the Rubio-Sancho method to calculate the total Density of States and the Local Density of States and the transmission, T.

2.2 Density Functional Theory

2.2.1 Born-Oppenheimer Approximation

Many-body systems consist of a large amount of atoms. Because of the large number of interactions, this system is often simplified in order to make calculations tractable. A useful approximation is the Born-Oppenheimer (BO) approximation, which is the assumption that the electronic and the nuclear motion in molecules can be separated [106]. The Schrödinger equation for a many-body system is written as:

$$\widehat{H}\Psi(\mathbf{r},\mathbf{R}) = E\Psi(\mathbf{r},\mathbf{R}) \rightarrow$$

$$\left[\widehat{T}_{\mathrm{e}}(\mathbf{r}) + \widehat{T}_{\mathrm{n}}(\mathbf{R}) + \widehat{V}_{\mathrm{ee}}(\mathbf{r}) + \widehat{V}_{\mathrm{nn}}(\mathbf{R}) + \widehat{V}_{\mathrm{en}}(\mathbf{r},\mathbf{R})\right]\Psi(\mathbf{r},\mathbf{R}) = E\Psi(\mathbf{r},\mathbf{R}) \qquad (2.1)$$

where $\widehat{H}$ is the Hamiltonian of the system, $\Psi(\mathbf{r},\mathbf{R})$ is the many-body wavefunction of the system, $\mathbf{r}$ refers to the electron positions and $\mathbf{R}$ refers to the nuclei positions, $\widehat{T}_{\mathrm{e}}(\mathbf{r}) = -\frac{1}{2}\sum_{i=1}^{N_{\mathrm{e}}}\nabla_{\mathbf{r}_i}^2$ is the kinetic energy of electrons, $\widehat{T}_{\mathrm{n}}(\mathbf{R}) = -\frac{1}{2M_I}\sum_{I=1}^{N_{\mathrm{n}}}\nabla_{\mathbf{R}_I}^2$ is the kinetic energy of nuclei, $\widehat{V}_{ee}(\mathbf{r}) = \frac{1}{2}\sum_{i\neq j}^{N_{\mathrm{e}}}\frac{1}{|\mathbf{r}_i-\mathbf{r}_j|}$ is the electron-electron Coulomb interaction energy, $\widehat{V}_{\mathrm{nn}}(\mathbf{R}) = \sum_{I\neq J}^{N_{\mathrm{n}}}\frac{Z_I Z_J}{|\mathbf{R}_I-\mathbf{R}_J|}$ is the nuclei-nuclei interaction energy, $\widehat{V}_{\mathrm{en}}(\mathbf{r},\mathbf{R}) = -\frac{1}{2}\sum_{i,I}^{N_{\mathrm{e}},N_{\mathrm{n}}}\frac{Z_I}{|\mathbf{r}_i-\mathbf{R}_I|}$ is the Coulomb interaction between electrons and nuclei and E is the energy of the system. The system is consisted of N_{e} electrons with mass m_{e} and N_{n} nuclei with mass M_I and atomic number Z_I. For convenience Hartree units have been used: $\overline{h}$=m_{e}=e=$4\pi\epsilon_0$=1.

Because nuclei are much heavier than electrons, nuclei are considered to be fixed.

Thus, $\widehat{T}_{\text{n}}(\mathbf{R})$ is much smaller than $\widehat{T}_{\text{e}}(\mathbf{r})$ by a factor of M_I/m_{e}. Consequently, for a fixed nuclear configuration, the Schrödinger equation, according to BO approximation, is written as:

$$\widehat{H}_{\text{el}}\psi(\mathbf{r},\mathbf{R}) = E_{\text{el}}\psi(\mathbf{r},\mathbf{R}) \rightarrow$$

$$\left[\widehat{T}_{\text{e}}(\mathbf{r}) + \widehat{V}_{\text{en}}(\mathbf{r},\mathbf{R}) + \widehat{V}_{\text{ee}}(\mathbf{r})\right]\psi(\mathbf{r},\mathbf{R}) = E_{\text{el}}\psi(\mathbf{r},\mathbf{R}) \rightarrow$$

$$\left[-\tfrac{1}{2}\sum_{i=1}^{N_{\text{e}}}\nabla^2_{\mathbf{r}_i} - \tfrac{1}{2}\sum_{i,I}^{N_{\text{e}},N_{\text{n}}}\tfrac{Z_I}{|\mathbf{r}_i-\mathbf{R}_I|} + \tfrac{1}{2}\sum_{i\neq j}^{N_{\text{n}}}\tfrac{1}{|\mathbf{r}_i-\mathbf{r}_j|}\right]\psi(\mathbf{r},\mathbf{R}) = E_{\text{el}}\psi(\mathbf{r},\mathbf{R}) \tag{2.2}$$

Equation (2.2) still contains $3N_{\text{e}}$ degrees of freedom, so solving it for systems with hundreds of atoms will be difficult. Thus, further approximations are required.

2.2.2 Hohenberg-Kohn Theorems

DFT uses the Hohenberg-Kohn (HK) theorems to solve the Schrödinger equation [107]. The formulation can be applied to a system with a Hamiltonian like in Equation (2.2). Now, instead of $3N_{\text{e}}$ wavefunction, the electron density is used which depends only on the three spatial coordinates. The electron density is defined as the probability of finding an electron at the position $\mathbf{r}$:

$$\rho(\mathbf{r}) = N_{\text{e}}\int|\Psi(\mathbf{r},\mathbf{r}_1,...,\mathbf{r}_{N_{\text{e}}})|^2 d\mathbf{r}_1...d\mathbf{r}_{N_{\text{e}}} \tag{2.3}$$

There are two HK Theorems and they state the following:

- **Theorem I:** For every system that has interacting particles in an external potential $V_{\text{ext}}(\mathbf{r})$, the potential $V_{\text{ext}}(\mathbf{r})$ is determined uniquely by the ground state density $\rho_0(\mathbf{r})$ except for a constant. This means that Hamiltonian is fully defined, except for a constant shift in energy. Thus, the many-body wavefunctions for all states are determined, including both ground and excited states.

- **Theorem II:** A universal functional for the energy $E[\rho]$ in terms of the density $\rho(\mathbf{r})$ can be defined, valid for any external potential $V_{\text{ext}}(\mathbf{r})$. For any particular $V_{\text{ext}}(\mathbf{r})$ the exact ground state energy of the system is the global minimum value of the functional and the density that minimizes the functional is the exact ground state

density $\rho_0(\mathbf{r})$. This means that the functional $E[\rho]$ alone is sufficient to determine the exact ground state energy and density. In general, the excited states of the electrons must be determined by other means.

The proofs of HK theorems are shown below:

Proof of Theorem I

Two different external potentials are assumed, $V_{\text{ext},1}(\mathbf{r})$ and $V_{\text{ext},2}(\mathbf{r})$, which differ by more than a constant and lead to the same ground state density $\rho(\mathbf{r})$. The two external potentials form different Hamiltonians, $\widehat{H}_1$ and $\widehat{H}_2$, which have different ground state wavefunctions Ψ_1 and Ψ_2, but they are assumed to have the same ground state density $\rho_0(\mathbf{r})$. It is:

$$E_1 = \langle \Psi_1 | \widehat{H}_1 | \Psi_1 \rangle < \langle \Psi_2 | \widehat{H}_1 | \Psi_2 \rangle \tag{2.4}$$

The inequality follows if the ground state is non-degenerate. The last term can be written as:

$$\langle \Psi_2 | \widehat{H}_1 | \Psi_2 \rangle = \langle \Psi_2 | \widehat{H}_2 | \Psi_2 \rangle + \langle \Psi_2 | \widehat{H}_1 - \widehat{H}_2 | \Psi_2 \rangle \rightarrow$$

$$\langle \Psi_2 | \widehat{H}_1 | \Psi_2 \rangle = E_2 + \int d^3r \big[V_{\text{ext},1}(\mathbf{r}) - V_{\text{ext},2}(\mathbf{r}) \big] \rho_0(\mathbf{r}) \tag{2.5}$$

It is consequently:

$$E_1 < E_2 + \int d^3r \big[V_{\text{ext},1}(\mathbf{r}) - V_{\text{ext},2}(\mathbf{r}) \big] \rho_0(\mathbf{r}) \tag{2.6}$$

For E_2 it is:

$$E_2 < E_1 + \int d^3r \big[V_{\text{ext},1}(\mathbf{r}) - V_{\text{ext},2}(\mathbf{r}) \big] \rho_0(\mathbf{r}) \tag{2.7}$$

From Equations (2.6) and (2.7) there is the contradictory inequality $E_1 + E_2 < E_2 + E_1$. Thus, two different external potentials cannot differ by more than a constant and the density uniquely determines the external potential within a constant.

Proof of Theorem II

Since all properties such as kinetic energy are uniquely determined if $\rho(\mathbf{r})$ is specified, the

Hamiltonian can be viewed as a functional of $\rho(\mathbf{r})$ as follows:

$$E_{\text{HK}}[\rho] = T[\rho] + E_{\text{int}}[\rho] + \int d^3r V_{\text{ext}}(\mathbf{r})\rho(\mathbf{r}) \tag{2.8}$$

A system with ground state density $\rho_1(\mathbf{r})$ corresponds to an external potential $V_{\text{ext},1}(\mathbf{r})$. From Theorem I the HK functional is equal to the expectation value of the Hamiltonian in the unique ground state which has wavefunction Ψ_1:

$$E_1 = E_{\text{HK}}[\rho_1] = \langle \Psi_1 | \widehat{H}_1 | \Psi_1 \rangle \tag{2.9}$$

A different density $\rho_2(\mathbf{r})$ is considered, that corresponds to a different wavefunction Ψ_2. It is:

$$E_1 = \langle \Psi_1 | \widehat{H}_1 | \Psi_1 \rangle < \langle \Psi_2 | \widehat{H}_1 | \Psi_2 \rangle = E_2 \tag{2.10}$$

Thus, the energy given by Equation (2.8), evaluated for the correct ground state density $\rho_0(\mathbf{r})$ is indeed lower than the value of this expression for any other density $\rho(\mathbf{r})$. This variational principle allows one to determine the ground state density assuming the form of the energy functional in Equation (2.2) is known. The variational principle states that the ground state energy E is always less than or equal to the other values of energy obtained for any other density $\rho(\mathbf{r})$. However, the HK Theorems do not prescribe any form of this functional.

2.2.3 Kohn-Sham scheme

DFT is based on a formulation of the energy functional that was formulated by Kohn and Sham [108]. Kohn and Sham replaced the original many-body problem by an auxiliary independent-particle problem. The ansatz of Kohn and Sham assumes that the ground state density of the original interacting system is equal to that of some chosen non-interacting system. That leads to independent-particle equations for the non-interacting system that can be considered exactly soluble. For a system of N_{e} independent electrons obeying the Hamiltonian, the ground state has one electron in each of the orbitals $\psi_i(\mathbf{r})$ with the lowest eigenvalues ϵ_i of the Hamiltonian. The term orbital means the wavefunction of one

electron. The total density of this system is given by:

$$\rho(\mathbf{r}) = \sum_{i=1}^{N_e} f_i |\psi_i(\mathbf{r})|^2 \tag{2.11}$$

The magnitude f_i determines the occupancy and it takes two values: 0 or 1.

The KS system of equations is:

$$\widehat{H}_{\text{KS}}\psi_i(\mathbf{r}) = \epsilon_i\psi_i(\mathbf{r}) \rightarrow$$

$$\big[-\tfrac{1}{2}\boldsymbol{\nabla}^2 + V_{\text{eff}}(\mathbf{r})\big]\psi_i(\mathbf{r}) = \epsilon_i\psi_i(\mathbf{r}) \tag{2.12}$$

where ϵ_i is the KS single-particle energy and the effective potential is a functional derivative of energy functional:

$$V_{\text{eff}}(\mathbf{r}) = V_{\text{ext}}(\mathbf{r}) + V_{\text{H}}[\rho(\mathbf{r})] + V_{\text{xc}}[\rho(\mathbf{r})] \tag{2.13}$$

where $V_{\text{H}}[\rho(\mathbf{r})] = \int d\mathbf{r}' \frac{\rho(\mathbf{r}')}{|\mathbf{r}-\mathbf{r}'|}$ is the Hartree potential and $V_{\text{xc}}[\rho(\mathbf{r})] = \frac{\delta E_{\text{xc}}}{\delta\rho(\mathbf{r})}$ is the exchange-correlation potential that is the derivative of the exchange-correlation energy with respect to density. The exchange-correlation effects arise due to the interactions between electrons. Electrons are fermions, which obey the Pauli exclusion principle. This states that two electrons cannot occupy the same quantum state. The exchange interaction guarantees that the total wavefunction of a many-body system is antisymmetric, which means a repulsion between electrons with the same spin and an attraction between electrons with opposite spins. This affects the arrangement of electrons within the electronic structure. The correlation interaction describes how the behaviour of electrons is influenced by the positions and motion of other electrons beyond the mean field approximation, which is not captured by the Hartree-Fock single determinant wavefunction. Understanding exchange-correlation effects is essential for predicting the electronic and structural properties of materials accurately. However, achieving precise descriptions of exchange-correlation effects in all situations is a difficult task and this is the reason why we use approximate methods to describe these interactions. The expression (2.12) describes a set of Schrödinger-like independent-particle equations that must be solved subject to the condition that the effective potential $V_{\text{eff}}(\mathbf{r})$ and the density $\rho(\mathbf{r})$ are consistent. This is a self-consistent problem.

The solution of the KS auxiliary system for the ground state can be viewed as the problem of minimization with respect to either the density $\rho(\mathbf{r})$ or the effective potential $V_{\text{eff}}(\mathbf{r})$. The KS approach applied to the full interacting system gives the total energy functional:

$$E_{\text{KS}}[\rho] = T_{\text{s}}[\rho] + \int d\mathbf{r} V_{\text{ext}}(\mathbf{r})\rho(\mathbf{r}) + E_{\text{H}}[\rho] + E_{\text{xc}}[\rho] \tag{2.14}$$

where $T_{\text{s}}[\rho]$ is the independent-particle kinetic energy :

$$T_{\text{s}}[\rho] = -\frac{1}{2}\sum_{i=1}^{N_{\text{e}}} \int d\mathbf{r} |\boldsymbol{\nabla}\psi_i(\mathbf{r})|^2 \tag{2.15}$$

$E_{\text{H}}[\rho]$ is the Hartree energy of the electron density $\rho(\mathbf{r})$ interacting with itself:

$$E_{\text{H}}[\rho] = \frac{1}{2}\int d\mathbf{r} d\mathbf{r}' \frac{\rho(\mathbf{r})\rho(\mathbf{r}')}{|\mathbf{r}-\mathbf{r}'|} \tag{2.16}$$

and $E_{\text{xc}}[\rho]$ is the term for the exchange-correlation energy.

2.2.4 Approximate exchange-correlation functionals

While the KS formalism is in principle exact, a major limitation is that the exact functionals for the exchange-correlation energy are not known, except for that of the free-electron gas [109, 110]. One of the simplest approximations is the Local Density Approximation (LDA), in which the exchange-correlation functional depends only on the density at the coordinate where the functional is evaluated, as follows:

$$E_{\text{xc}}^{\text{LDA}}[\rho] = \int \epsilon_{\text{xc}}(\rho(\mathbf{r}))\rho(\mathbf{r}) d\mathbf{r} \tag{2.17}$$

In Equation 2.17, the term $\epsilon_{\text{xc}}(\rho(\mathbf{r}))$ is the exactly known exchange-correlation energy per particle for a homogeneous electron gas of density $\rho(\mathbf{r})$.

If the exchange-correlation functional depends also on the gradient of the density, this leads to the Generalized Gradient Approximation (GGA) functional:

$$E_{\text{xc}}^{\text{GGA}}[\rho] = \int \epsilon_{\text{xc}}(\rho(\mathbf{r}), \boldsymbol{\nabla}\rho(\mathbf{r}))\rho(\mathbf{r}) d\mathbf{r} \tag{2.18}$$

GGA functional gives very good results for molecular geometries and ground-state energies [111].

There are extensions of these approximate exchange-correlation functionals. The Laplacian of the density $\nabla^2\rho(\mathbf{r})$ or the kinetic energy density can be added for the calculation of ϵ_{xc} except for $\rho(\mathbf{r})$ and $\nabla\rho(\mathbf{r})$. This is called meta-GGA functional, but its calculation requires much higher computational cost, and the results are not improved significantly [112]. Functionals can also include a portion of the exact exchange-correlation energy functional from the Hartree-Fock approach and from the approximate exchange-correlation functionals (LDA, GGA etc.) and these are called hybrid [113].

2.2.5 Van der Waals functionals

In DFT calculations the true exchange-correlation functional should include the van der Waals (vdW)/dispersion interactions, which are the interactions between adjacent layers. These are the interactions that exist between atoms that belong to vertically stacked layers. Unfortunately, the well-established approximations (LDA and GGA functionals) do not capture vdW interactions at all. The total energy E_{DFT-D} including vdW corrections is given by:

$$E_{\text{DFT}-\text{D}} = E_{\text{KS}} + E_{\text{disp}} \tag{2.19}$$

where E_{KS} is the total energy obtained from the KS equations and E_{disp} is the extra energy term added to account for the vdW corrections. There are many different ways to calculate the term E_{disp}.

One of them is the D2 method of Grimme [114], in which the correction term takes the form:

$$E_{\text{disp}} = -s_6 \sum_{I=1}^{N_{\text{n}}} \sum_{J=1}^{N_{\text{n}}} \frac{C_6^{IJ}}{R_{IJ,\text{L}}^6} f_{\text{dmp}}(R_{IJ}) \tag{2.20}$$

where the summations are over all nuclei N_{n}, C_6^{IJ} symbolizes the dispersion coefficient for the pair IJ, s_6 is a scaling factor that is dependent on the relevant functional and R_{IJ} is the distance between nuclei. The damping function is given by the formula:

$$f_{\text{dmp}}(R_{IJ}) = \frac{1}{1+e^{-d(R_{IJ}/R_{\text{r}}-1)}} \tag{2.21}$$

where R_{r} is the summation of the atomic vdW radii.

2.2.6 Practical implementation of Density Functional Theory

An actual calculation for DFT uses a numerical procedure that successively updates $V_{\text{eff}}(\mathbf{r})$ and $\rho(\mathbf{r})$, in order to reach a self-consistent solution. First, an electron density $\rho(\mathbf{r})$ is suggested and the effective potential $V_{\text{eff}}(\mathbf{r})$ is calculated. Next by solving the one-electron KS equation $\widehat{H}_{\text{KS}}\psi_i(\mathbf{r}) = \epsilon_i\psi_i(\mathbf{r})$ the orbitals $\psi_i(\mathbf{r})$ are obtained. The new electron density is then implemented by Equation (2.11). If the value of the electron density is the same as the initial guess, within an accuracy ϵ, self-consistency is achieved and the ground-state total energy, forces, stresses, and eigenvalues are calculated. However, if the value of the electron density is not the same as the initial guess, the same procedure is repeated with an updated electron density, until the two values coincide. Figure 2.1 shows the general iterative scheme.

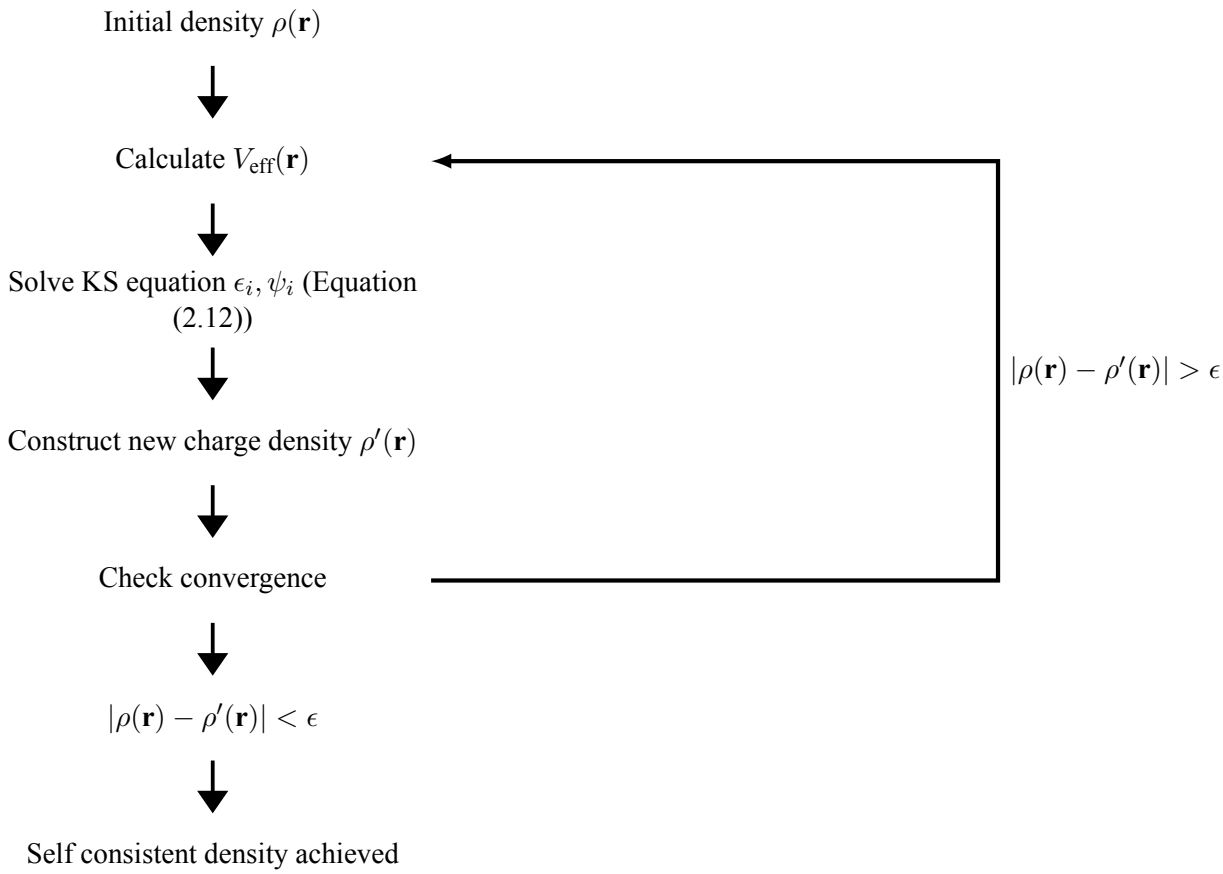

Figure 2.1: *Schematic outline of the iterative solution of the KS equations.*

We performed DFT calculations with VASP program [115–118]. The Projector Augmented-Wave (PAW) method [119, 120] is implemented in VASP, which uses plane waves as a basis set for the expansion of eigenstates for the solution of KS equations. According to Bloch's theorem [121], the electron wavefunctions in a crystalline material can be written as the product of a plane wave and a periodic function. Using the Fourier expansion over a set of plane waves the single-particle wavefunctions $\psi_j(\mathbf{r})$ are:

$$\psi_j(\mathbf{r}) = \sum e^{i\mathbf{k}\cdot\mathbf{r}} c_k^j \tag{2.22}$$

where the summation is all over the plane waves, $\mathbf{k}$ is the Bloch wavevector within the first BZ and c_k^j corresponds to the expansion coefficients. For the k-points mesh within the first BZ Monkhorst-Pack grid was used, which means that the selected $\mathbf{k}$-points consist of a grid of points, which is distributed homogeneously in the BZ [122].

The expansion coefficients are also expanded in plane waves, as follows:

$$c_k^j(\mathbf{r}) = \tfrac{1}{\sqrt{\Omega}} \sum_{\mathbf{G}} e^{i\mathbf{G}\cdot\mathbf{r}} C_G^k \tag{2.23}$$

where Ω is the volume in real space. The basis set includes all plane waves for which:

$$\tfrac{1}{2}|\mathbf{G}+\mathbf{k}|^2 < E_{\text{cutoff}} \tag{2.24}$$

where energy cutoff is: $E_{\text{cutoff}} = \frac{|\mathbf{k}|^2}{2}$ and corresponds to the maximum kinetic energy of any plane wave. The higher the energy cutoff E_{cutoff}, the more accurate the calculation.

VASP simplifies calculations with the use of pseudopotentials. Because of the large number of plane waves to expand the wavefunctions of core electrons, the pseudopotentials replace the potential for the core electrons with a much softer effective potential felt by the valence electrons. This reduces the computational cost, as the number of plane waves needed for the expansion of the wavefunctions is decreased.

2.3 Tight-Binding Approximation

A Tight-Binding (TB) technique was first introduced for 1D linear atomic chains [123] and later was generalised for 2D systems [124]. It is a semi-empirical method that has a

much lower computational cost compared to DFT. The name 'Tight-Binding' means that the electrons considered for this model should be tightly bound to the atom to which they belong and have limited interactions with the surrounding atoms. TB approach was used for the study of the electronic structure and transport properties of graphene.

2.3.1 Energy dispersion for monolayer graphene

In graphene, σ and σ^* orbitals are strongly separated in energy as shown in Figure 1.1 (b). Because of this, their contribution to the electronic and transport properties is often neglected and only the π and π^* orbitals are taken into account. The total wavefunction of MLG can then be expressed as a linear combination of the atomic p_z orbitals for the A and B sublattice. According to Bloch's theorem [121], the total wavefunction of MLG is written as:

$$\Psi(\mathbf{k},\mathbf{r}) = \Psi_A(\mathbf{k},\mathbf{r}) + \Psi_B(\mathbf{k},\mathbf{r}), \tag{2.25}$$

$$\text{with } \Psi_A(\mathbf{k},\mathbf{r}) = \sum_{j=1}^{N_\text{n}} C_{A,j}(\mathbf{k})\Phi_{A,j}(\mathbf{r}-\mathbf{r}_{A,j}) = \tfrac{1}{\sqrt{N_\text{n}}}\sum_{j=1}^{N_\text{n}} e^{i\mathbf{k}\cdot\mathbf{r}_{A,j}}\Phi_{A,j}(\mathbf{r}-\mathbf{r}_{A,j})$$

$$\text{and } \Psi_{B,j}(\mathbf{k},\mathbf{r}) = \sum_{j=1}^{N_\text{n}} C_{B,j}(\mathbf{k})\Phi_{B,j}(\mathbf{r}-\mathbf{r}_{B,j}) = \tfrac{1}{\sqrt{N_\text{n}}}\sum_{j=1}^{N_\text{n}} e^{i\mathbf{k}\cdot\mathbf{r}_{B,j}}\Phi_{B,j}(\mathbf{r}-\mathbf{r}_{B,j})$$

where $\Phi_{A,j}(\mathbf{r})$ and $\Phi_{B,j}(\mathbf{r})$ are the TB Bloch orthogonal wavefunctions for the p_z orbitals with positions $\mathbf{r}_{A,j}$ and $\mathbf{r}_{B,j}$ for the A and B sublattices respectively and $C_{A,j}(\mathbf{k})$ and $C_{B,j}(\mathbf{k})$ are the plane-wave contributions for the j-th orbital for the A and B sublattices respectively [125]. Here, $\mathbf{k} = (k_x, k_y)$ is the crystal momentum, which is chosen to be in the first BZ in our calculations, and N_n refers to the number of atoms (p_z orbitals for graphene). The Schrödinger equation for MLG is:

$$\widehat{H}(\mathbf{k})\Psi(\mathbf{k},\mathbf{r}) = E(\mathbf{k})\Psi(\mathbf{k},\mathbf{r}) \tag{2.26}$$

where $\widehat{H}(\mathbf{k})$ is the Hamiltonian of MLG and $E(\mathbf{k})$ its eigenvalues. Equation (2.26) can be rewritten by inserting Equation (2.25), as follows:

$$\begin{pmatrix} H_{\text{AA}}(\mathbf{k}) & H_{\text{AB}}(\mathbf{k}) \\ H_{\text{BA}}(\mathbf{k}) & H_{\text{BB}}(\mathbf{k}) \end{pmatrix} \cdot \begin{pmatrix} C_A(\mathbf{k}) \\ C_B(\mathbf{k}) \end{pmatrix} = E(\mathbf{k}) \begin{pmatrix} C_A(\mathbf{k}) \\ C_B(\mathbf{k}) \end{pmatrix} \tag{2.27}$$

The elements $H_{\mathrm{AA}}(\mathbf{k})$ are equal $H_{\mathrm{BB}}(\mathbf{k})$, because the atoms in the A and B sublattices are identical. The matrix element $H_{\mathrm{AA}}(\mathbf{k})$ is written as follows:

$$H_{\mathrm{AA}}(\mathbf{k}) = \langle \Psi_A | \widehat{H} | \Psi_A \rangle \rightarrow$$

$$H_{\mathrm{AA}}(\mathbf{k}) = \frac{1}{N_{\mathrm{n}}} \sum_{i,j}^{N_{\mathrm{n}}} e^{i\mathbf{k}(\mathbf{r}_i - \mathbf{r}_j)} \langle \Phi_A(\mathbf{r}_i) | \widehat{H} | \Phi_A(\mathbf{r}_j) \rangle = 0 \tag{2.28}$$

Same for $H_{\mathrm{BB}}(\mathbf{k})$ it is:

$$H_{\mathrm{BB}}(\mathbf{k}) = \langle \Psi_B | \widehat{H} | \Psi_B \rangle \rightarrow$$

$$H_{\mathrm{BB}}(\mathbf{k}) = \frac{1}{N_{\mathrm{n}}} \sum_{i,j}^{N_{\mathrm{n}}} e^{i\mathbf{k}(\mathbf{r}_i - \mathbf{r}_j)} \langle \Phi_B(\mathbf{r}_i) | \widehat{H} | \Phi_{B(\mathbf{r}_j)} \rangle = 0 \tag{2.29}$$

The matrix elements H_{AA} and H_{BB} are set to zero because the onsite energies are set to zero for simplicity and only first nearest-neighbor interactions are taken into account. This can be done, because in graphene there is only one type of atom (carbon), so all of the atoms have the same onsite energies, for no interlayer bias.

For the matrix element $H_{\mathrm{AB}}(\mathbf{k})$ it is:

$$H_{\mathrm{AB}}(\mathbf{k}) = \langle \Psi_A | \widehat{H} | \Psi_B \rangle \rightarrow$$

$$H_{\mathrm{AB}}(\mathbf{k}) = \frac{1}{N_{\mathrm{n}}} \sum_{i,j}^{N_{\mathrm{n}}} e^{i\mathbf{k}(\mathbf{r}_i - \mathbf{r}_j)} \langle \Phi_A(\mathbf{r}_i) | \widehat{H} | \Phi_B(\mathbf{r}_j) \rangle \tag{2.30}$$

After restricting the electron interactions only to first-nearest neighbors, Equation (2.30) is written as:

$$H_{\mathrm{AB}}(\mathbf{k}) = \langle \Phi_{A,0} | \widehat{H} | \Phi_{B,0} \rangle + e^{-i\mathbf{k}\cdot\mathbf{a}_1} \langle \Phi_{A,0} | \widehat{H} | \Phi_{B,-\mathbf{a}_1} \rangle + e^{-i\mathbf{k}\cdot\mathbf{a}_2} \langle \Phi_{A,0} | \widehat{H} | \Phi_{B,-\mathbf{a}_2} \rangle \rightarrow$$

$$H_{\mathrm{AB}}(\mathbf{k}) = V^0_{\mathrm{pp}\pi} \cdot f(\mathbf{k}) \tag{2.31}$$

where $V^0_{\mathrm{pp}\pi}$=-2.7 eV [126] is the nearest-neighbor in-plane transfer integral for graphene and $f(\mathbf{k}) = 1 + e^{-i\mathbf{k}\cdot\mathbf{a}_1} + e^{-i\mathbf{k}\cdot\mathbf{a}_2}$. For the matrix element $H_{\mathrm{BA}}(\mathbf{k})$ it is:

$$H_{\mathrm{BA}}(\mathbf{k}) = H^*_{\mathrm{AB}}(\mathbf{k}) = V^0_{\mathrm{pp}\pi} \cdot f^*(\mathbf{k}) \tag{2.32}$$

Inserting Equations (2.28), (2.29), (2.31) and (2.32) into Hamiltonian $\widehat{H}(\mathbf{k})$, leads to:

$$\widehat{H}(\mathbf{k}) = \begin{pmatrix} 0 & V^0_{\text{pp}\pi} \cdot f(\mathbf{k}) \\ V^0_{\text{pp}\pi} \cdot f^*(\mathbf{k}) & 0 \end{pmatrix} \tag{2.33}$$

The solution of Schrödinger equation 2.26 for the Hamiltonian in Equation (2.33) leads to the energy dispersion relation for MLG:

$$E_{\pm}(\mathbf{k}) = \pm V^0_{\text{pp}\pi}|f(\mathbf{k})| \rightarrow$$

$$E_{\pm}(\mathbf{k}) = \pm V^0_{\text{pp}\pi}\sqrt{3 + 2cos(\mathbf{k}\cdot\mathbf{a}_1) + 2cos(\mathbf{k}\cdot\mathbf{a}_2) + 2cos(\mathbf{k}(\mathbf{a}_2 - \mathbf{a}_1))} \rightarrow$$

$$E_{\pm}(k_x, k_y) = \pm V^0_{\text{pp}\pi}\sqrt{1 + 4cos\tfrac{k_x a_{\text{const}}\sqrt{3}}{2} cos\tfrac{k_y a_{\text{const}}}{2} + 2(1 + cosk_y a_{\text{const}})} \rightarrow$$

$$E_{\pm}(k_x, k_y) = \pm V^0_{\text{pp}\pi}\sqrt{1 + 4cos\tfrac{\sqrt{3}k_x a_{\text{const}}}{2} cos\tfrac{k_y a_{\text{const}}}{2} + 4cos^2\tfrac{k_y a_{\text{const}}}{2}} \tag{2.34}$$

The electronic band structure for MLG is depicted in Figure 1.4 along the high-symmetry points $\Gamma \rightarrow K \rightarrow M$.

2.3.2 Energy dispersion for bilayer graphene

In BLG the exact form of Hamiltonian $\widehat{H}(\mathbf{k})$ depends on the relevant stacking because the interlayer interactions change with stacking. The intralayer and the interlayer interactions for nearest neighbors interactions for BLG with AA stacking and AB stacking are depicted in Figures 2.2 (a) and (b) respectively.

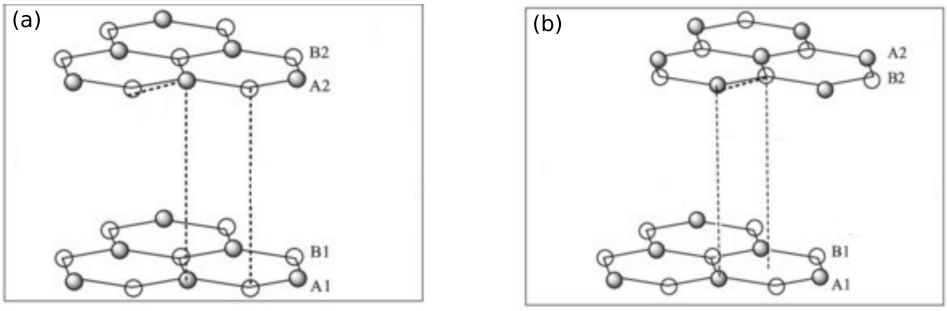

Figure 2.2: *Interlayer interactions for (a) AA-stacked and (b) AB-stacked BLG. Figures (a) and (b) adapted from [127].*

The Hamiltonian $\widehat{H}(\mathbf{k})$ for BLG is constructed by determining the hopping terms. The generalized formula for calculating the hopping terms beyond nearest neighbors in BLG

is given by the Slater-Koster-type formula [128]:

$$t(\mathbf{d}) = V^0_{\mathrm{pp}\pi}\left[1 - \left(\frac{\mathbf{d}\cdot\mathbf{e}_z}{|\mathbf{d}|}\right)^2\right] + V^0_{\mathrm{pp}\sigma}\left(\frac{\mathbf{d}\cdot\mathbf{e}_z}{|\mathbf{d}|}\right)^2 \tag{2.35}$$

where $\mathbf{d} = \mathbf{r}_i - \mathbf{r}_j$ is the distance between atoms i and j at atomic positions $\mathbf{r}_i$ and $\mathbf{r}_j$ respectively, $V^0_{\mathrm{pp}\sigma}$=0.48 eV is the nearest-neighbor out-of-plane, vertically-aligned, transfer integrals for unstrained BLG, d_0=3.35 Å is the unstrained out-of-plane atomic separations and $\mathbf{e}_z$ is the unit vector in the out-of-plane z-direction, perpendicular to graphene xy-plane. Thus, $\mathbf{d}\cdot\mathbf{e}_z$ is the projection along z-direction. The values of the parameters $V_{\mathrm{pp}\sigma}$ and d_0 were chosen according to Reference [92]. The interlayer distance depends on the relevant stacking, but here we assumed that it is the same for every stacking. We took into account interactions beyond nearest neighbors, because of the interlayer interactions for arbitrary stackings. From the DFT calculations that we performed in Chapter 3 we found the two extremes of energy for BLG correspond to AA and AB-stacked BLG (Figure 1.3), to have interlayer distance difference 0.13 Å. In our calculations, we considered electron interactions beyond nearest neighbors for the xy-plane. The Slater-Koster-type TB model is suitable for systems with inhomogeneous strains and stackings, as it can account for differing bond lengths in both the in-plane and out-of-plane directions and has previously been applied in studies of twisted bilayers [92, 129]. The electronic band structures of BLG for AA-, AB/BA-, and SP stacking near K point are depicted in Figures 1.5 (a)–(c) respectively.

The effect of a simple interlayer bias Δ can be included by adding the term $\epsilon_i = \pm\frac{\Delta}{2}$ to the diagonal terms, where there are the onsite energies. Onsite energies in the TB method refer to the energy of an electron at a particular orbital. We have chosen the sign '+' to correspond to the atoms on the top layer and the sign '-' to correspond to the atoms on the bottom layer of BLG. Figures 1.5 (d)–(f) depict the electronic band structures of BLG for AA, AB/BA and SP stacking under the application of Δ=-200 meV interlayer bias.

2.3.3 Energy dispersion for strained monolayer and bilayer graphene

With the inclusion of strain in MLG, the hopping term depends on the distance between the in-plane carbon atoms: $V_{\mathrm{pp}\pi}(|\mathbf{r}|) = V^0_{\mathrm{pp}\pi}e^{-\frac{|\mathbf{r}|-a_0}{r_0}}$, where a_0=1.42 Å is the nearest-neighbor

in-plane distance between carbon atoms and r_0=2.453 Å is the decay length of graphene, i.e. the distance over which the bond strength or the probability of finding an electron between two atoms decreases significantly [130]. Thus, the energy dispersion relation for MLG (Equation (2.34)) with the inclusion of strain is modified as follows:

$$E_{\pm}(k_x, k_y) = \pm V_{\text{pp}\pi}(|\mathbf{r}|)\sqrt{1 + 4cos\frac{\sqrt{3}k_x a_{\text{const}}}{2}cos\frac{k_y a_{\text{const}}}{2} + 4cos^2\frac{k_y a_{\text{const}}}{2}} \tag{2.36}$$

Concerning BLG, strain is included through the hopping terms as follows:

$$t(\mathbf{d}) = V_{\text{pp}\pi}(|\mathbf{d}|)\left[1 - \left(\frac{\mathbf{d}\cdot\mathbf{e}_z}{|\mathbf{d}|}\right)^2\right] + V_{\text{pp}\sigma}(|\mathbf{d}|)\left(\frac{\mathbf{d}\cdot\mathbf{e}_z}{|\mathbf{d}|}\right)^2, \tag{2.37}$$

$$\text{with } V_{\text{pp}\pi}(|\mathbf{d}|) = V^0_{\text{pp}\pi}e^{-\frac{|\mathbf{d}|-a_0}{r_0}} \text{ and } V_{\text{pp}\sigma}(|\mathbf{d}|) = V^0_{\text{pp}\sigma}e^{-\frac{|\mathbf{d}|-d_0}{r_0}}. \tag{2.38}$$

where $|\mathbf{d}|$ is the magnitude of the vector $\mathbf{d}$.

2.4 Green Functions

The Green function (GF) [131] that corresponds to the Schrödinger equation (2.26) is defined as:

$$\widehat{g} = \lim_{\eta\to 0^+}[(E \pm i\eta)\widehat{I} - \widehat{H}]^{-1} \tag{2.39}$$

where $\widehat{H}$ is the relevant Hamiltonian for the investigated system, $\widehat{I}$ is the identity operator and E is the energy. Here, η is a small and positive number added to the energy to secure that the GF $\widehat{g}$ is well-defined around the eigenvalues of the Hamiltonian $\widehat{H}$. In Equation (2.39) the '+' sign corresponds to the retarded GF $\widehat{g}^+$ and the '-' sign corresponds to the advanced GFs $\widehat{g}^-$. For simplicity, when there is no sign '+' or '-' in the GFs $\widehat{g}$, we meant the retarded GFs. GFs can be used to calculate the Density of States (DOS), as well as the transmission, T, of a given system. The Total DOS (TDOS) refers to the number of energy states per energy interval that are available to be occupied by electrons for each energy for all the lattice points of the system and the Local DOS (LDOS) is the DOS at a particular site or orbital in the material.

Here, we show the steps to calculate LDOS and TDOS knowing the GFs of the sys-

tem. The Hamiltonian $\widehat{H}$ of a system with eigenvalues ϵ_m and eigenstates $|\Psi_m\rangle$ for each particular orbital m is written as:

$$\widehat{H} = \sum_m |\Psi_m\rangle \epsilon_m \langle\Psi_m| \tag{2.40}$$

Inserting Equation (2.40) into Equation (2.39) gives:

$$\widehat{g} = \lim_{\eta\to 0^+} \sum_m |\Psi_m\rangle \tfrac{1}{E+i\eta-\epsilon_m} \langle\Psi_m| \tag{2.41}$$

Projecting into orbitals $|j\rangle$ and $|l\rangle$ gives for the GF $\widehat{g}$:

$$g_{j,l} = \langle j|\widehat{g}|l\rangle = \lim_{\eta\to 0^+} \sum_m \langle j|\Psi_m\rangle \tfrac{1}{E+i\eta-\epsilon_m} \langle\Psi_m|l\rangle \tag{2.42}$$

Multiplying the numerator and the denominator by $(E - i\eta - \epsilon_m)$ gives:

$$g_{j,l} = \lim_{\eta\to 0^+} \sum_m \langle j|\Psi_m\rangle \tfrac{E-i\eta-\epsilon_m}{E-\epsilon_m^2+\eta^2} \langle\Psi_m|l\rangle \tag{2.43}$$

The imaginary part of $g_{i,j}$ is:

$$Im\ (g_{j,l}) = \lim_{\eta\to 0^+} \sum_m \langle j|\Psi_m\rangle \tfrac{-\eta}{E-\epsilon_m^2+\eta^2} \langle\Psi_m|l\rangle \tag{2.44}$$

Using the Dirac Delta function:

$$\delta(x) = \tfrac{1}{\pi} \lim_{\eta\to 0^+} \tfrac{\eta}{x^2+\eta^2} \tag{2.45}$$

and setting l=j gives:

$$-\tfrac{1}{\pi} Im\ (g_{j,j}) = \sum_m |\langle j|\Psi_m\rangle|^2 \delta(E-\epsilon_m) \tag{2.46}$$

Equation (2.46) provides the LDOS for a particular atom j. Summing over all sites in the system results in the TDOS. Alternatively, TDOS can be written as a trace over the GF $\widehat{g}$:

$$TDOS = -\tfrac{1}{\pi} Im\ Tr\ (\widehat{g}) \tag{2.47}$$

2.4.1 The Dyson Equation

When a system has translational invariance, the eigenvectors can be calculated using Bloch's theorem. However, when translational invariance is broken, such as with the application of heterostrain, the Bloch wavevectors are no longer eigenvectors of the system. The Dyson equation lets us write the GF $\widehat{G}$ of the perturbed system using the GF $\widehat{g}$ of the unperturbed system and the term form the applied perturbation, without the need to calculate the eigenvectors of the perturbed system. This process has an easy calculation of physical properties, including the DOS, when there is a perturbation.

The Dyson equation can be calculated, by using the definition of the GF $\widehat{g}$ (Equation (2.39)). The Hamiltonian of the perturbed system can be expressed as $\widehat{H} = \widehat{H}_{\text{unperturbed}} + \widehat{V}$, where $\widehat{V}$ determines the interactions between adjacent cells in our calculations, as explained in Subsection 2.4.2. Here, $\widehat{V}$ refers to the hopping terms of electrons, as they move from one location to the other. The GF of the full system $\widehat{G}$ can be written in terms of the GF of the unperturbed system $\widehat{g}$, which is associated with the Hamiltonian $\widehat{H}_{unperturbed}$, as follows:

$$\widehat{G} = [(E + i\eta)\widehat{I} - (\widehat{H}_{\text{unperturbed}} + \widehat{V})]^{-1} \rightarrow$$

$$\widehat{G} = [\widehat{g}^{-1} - \widehat{V}]^{-1} \rightarrow$$

$$\widehat{G} = [\widehat{I} - \widehat{g}\widehat{V}]^{-1}\widehat{g} \tag{2.48}$$

Multiplying Equation (2.48) by $[\widehat{I} - \widehat{g}\widehat{V}]^{-1}$, results in the Dyson equation:

$$\widehat{G} = \widehat{g} + \widehat{g}\widehat{V}\widehat{G} \tag{2.49}$$

The Dyson equation can be used specifically for connecting two large systems. In order to be applied efficiently (with minimum computational cost), it can be used recursively. For our study, the Dyson equation is used for the calculation of surface GFs, as explained in Subsection 2.4.2. Surface GFs are the GFs that account for the effects of the boundaries or interfaces, and in our study include the effect of the left and right lead, because of the inclusion of periodicity along x-direction. The surface GFs are necessary to determine the electronic and transport properties of hBLG, as explained in Subsections 2.4.3 and 2.4.4.

2.4.2 Recursive Green Functions Method with application in Rubio-Sancho method

In large systems, such as hBLG with small strain, the DOS and the transmission, T, can be calculated more efficiently by splitting the unit cell of the investigated system (hBLG) into smaller cells, as is implemented in the Recursive Green Functions (RGF) method [123]. The unit cells of our calculations were divided into cells, by selecting specific atoms as the first cell and then we specified the other cells, by setting a cutoff distance **d**=1.82 Å for the interactions in the xy-plane. Because of the application of heterostrain and the inclusion of Poisson contraction ν, each cell has a different number of atoms, so different sizes. The unit cell of the central device of hBLG that we investigated and the unit cells of the left and right leads, were divided in the same way into 1, 2, ..., N_c cells, are depicted in Figure 2.3. The RGF method is very reliable, and computationally efficient and allows for parallel implementation. For the calculation of GFs and subsequently the DOS and the transmission, T, we first split the unit cell of hBLG (called 'Central Device') into cells. The central device is the supercell used in the leads, which is useful for very large but periodic systems. In order to determine the transmission, T, we add 'leads' on the left and on the right of the central device which have the same size and the same arrangement of carbon atoms as the unit cell of the central device, and we used the Rubio-Sancho method to calculate the surface GFs, $\widehat{G}_{\mathrm{SL}}$ and $\widehat{G}_{\mathrm{SR}}$, for the left and right lead respectively, and consequently the self-energies from the left and right leads [132]. Self-energy arises due to the interactions between the system (Central Device) and the surrounding environment consisting of the left and right lead modifies the energy of the electrons.

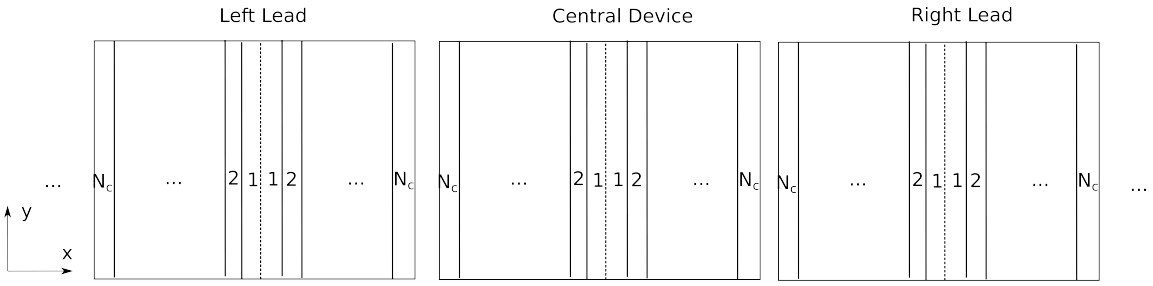

Figure 2.3: *Unit cells of the central device and the left and right leads, divided into 1, 2,.., N_c cells. Here, x and y-directions are also shown.*

The Hamiltonian of the central device and the leads is a block matrix:

$$\widehat{H} = \begin{bmatrix} \widehat{H}_{1,1} & \widehat{H}_{1,2} & & \dots \\ \widehat{H}_{2,1} & \widehat{H}_{2,2} & & \dots \\ \vdots & & \ddots & \\ \widehat{H}_{N_c,1} & \widehat{H}_{N_c,2} & & \widehat{H}_{N_c,N_c} \end{bmatrix}$$

where $\widehat{H}_{1,1}$ corresponds to the Hamiltonian of the first cell, $\widehat{H}_{2,2}$ corresponds to the Hamiltonian of the second cell etc. The submatrices $\widehat{H}_{i,i+1}$ and $\widehat{H}_{i+1,i}$ correspond to the electron interactions between the i-th and the (i+1)-th cell.

Bloch phases can be used to account for periodicity in the other direction (e.g. the y-direction in this example). For the inclusion of periodicity along y-direction, we used as Hamiltonian of the system, the following:

$$\widehat{H}_{\text{total}} = \widehat{H} + \widehat{H}_{\text{bt}} e^{i \cdot k_y \cdot y_{\text{cell}}} + \widehat{H}_{\text{tb}} e^{-i \cdot k_y \cdot y_{\text{cell}}} \tag{2.50}$$

where $\widehat{H}_{\text{bt}}$ is the Hamiltonian that includes the elements of the unit cell which is on top of the unit cell of the central device and $\widehat{H}_{\text{tb}}$ is the unit cell which is below the unit cell of the central device, as depicted in Figure 2.4. These unit cells have the same size and the same arrangement of carbon atoms. Here, y_{cell} is the length of the unit cell along y-direction and k_y includes points in k-space which belong in the First BZ along the y-direction. Last, we normalized the results for the k-space for the calculation of TDOS, LDOS, and transmission, T.

For the calculation of TDOS with the RGF method, we first calculated the GF $\widehat{g}_{i,i}$ for each individual i-th cell (Equation (2.39)), as follows:

$$\widehat{g}_{i,i} = \lim_{\eta \to 0^+} [(E + i\eta)\widehat{I}_{i,i} - \widehat{H}_{i,i}]^{-1} \tag{2.51}$$

and the TDOS (Equation (2.47)), including only the contribution from the first cell, as follows:

$$TDOS = -\tfrac{1}{\pi} Im\, Tr\, (\widehat{g}^1_{1,1}) \tag{2.52}$$

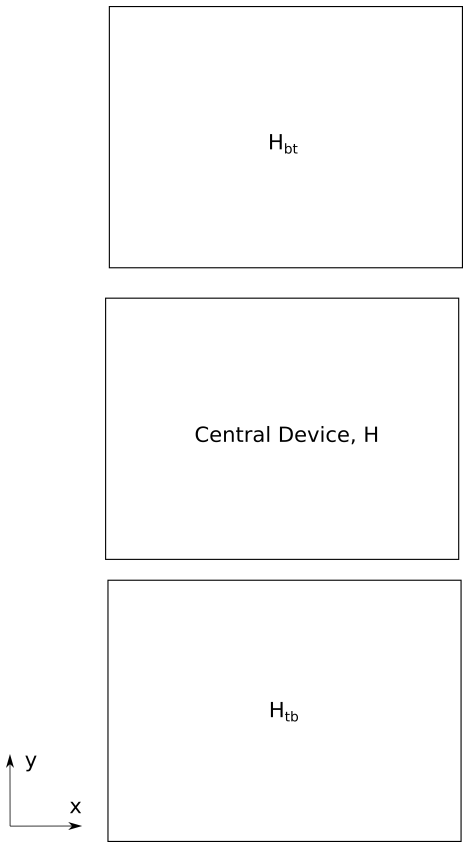

Figure 2.4: *Central device and the adjacent unit cells on top and on the bottom respectively for the inclusion of periodicity along y-direction.*

For the second cell we computed the quantity $\widehat{A}_2$:

$$\widehat{A}_2 = \widehat{V}_{2,1}\widehat{g}^{[1]}_{1,1}\widehat{g}^{[1]}_{1,1}\widehat{V}_{1,2} \tag{2.53}$$

while for the other i-th cells we had:

$$\widehat{A}_i = \widehat{V}_{i,i-1}\widehat{g}^{[i-1]}_{i-1,i-1}(\widehat{A}_{i-1} + \widehat{I}_{i-1,i-1})\widehat{g}^{[i-1]}_{i-1,i-1}\widehat{V}_{i-1,i} \tag{2.54}$$

where the matrix elements $\widehat{V}_{i,i-1}$ and $\widehat{V}_{i-1,i}$ correspond to the electron interactions between the i-th and the (i-1)-th cells for cutoff distance **d**=1.82 Å for the xy-plane and $\widehat{g}^{[i-1]}_{i-1,i-1}$ is the GF of the (i-1)-th cell after all (i-1) has been added. The GF $\widehat{g}^{[i]}_{i,i}$ and TDOS are calculated recursively for each step as follows:

$$\widehat{g}^{[i]}_{i,i} = (\widehat{I}_{i,i} - \widehat{g}_{i,i}\widehat{V}_{i,i-1}\widehat{g}^{[i-1]}_{i-1,i-1}\widehat{V}_{i-1,i})^{-1}\widehat{g}^{[i-1]}_{i,i} \tag{2.55}$$

$$TDOS_{\text{new}} = TDOS_{\text{old}} - \tfrac{1}{\pi} Im\, Tr\, \left(\widehat{g}^{[i]}_{i,i}(\widehat{A}_i + \widehat{I}_{i,i})\right) \tag{2.56}$$

We used the GF in Equation (2.55) for the calculation of the surface GFs that stem from the left and right lead. For each step, going from the i-th cell to (i+1)-th cell, we calculated the surface GFs that correspond to the left and right edges and the GFs that connect them, until the surface GFs are within an accuracy ϵ_{GF}. This means that the surface GFs obtained from the n-th step obey this inequality: $|\widehat{G}^{[n]} - \widehat{G}^{[n-1]}| \leq \epsilon_{\text{GF}}$, and once it is satisfied the recursive calculations stop. For each step, the Rubio-Sancho method efficiently doubles the length of the unit cells along x-direction for our study. This means that for a unit cell with N_{c} connected cells with relevant GFs $\widehat{g}_{1,1}$, $\widehat{g}_{N_{\text{c}},N_{\text{c}}}$, $\widehat{g}_{1,N_{\text{c}}}$ and $\widehat{g}_{N_{\text{c}},1}$ which are known, the corresponding GF for a system twice this size can be calculated by joining the right edge of this system to the left edge of an identical system, whose cells are now denoted N_{c}+1, ..., $2N_{\text{c}}$, instead of 1, ..., N_{c}. The doubling of the unit cell is depicted in Figure 2.5.

For each step we set: $\widehat{g}^{\text{old}}_{1,1} = \widehat{g}_{1,1} = \widehat{g}_{N_{\text{c}}+1,N_{\text{c}}+1}$, $\widehat{g}^{\text{old}}_{1,E} = \widehat{g}_{1,N_{\text{c}}} = \widehat{g}_{N_{\text{c}}+1,2N_{\text{c}}}$, $\widehat{g}^{\text{old}}_{E,1} = \widehat{g}_{N_{\text{c}},1} = \widehat{g}_{2N_{\text{c}},N_{\text{c}}+1}$ and $\widehat{g}^{\text{old}}_{E,E} = \widehat{g}_{N_{\text{c}},N_{\text{c}}} = \widehat{g}_{2N_{\text{c}},2N_{\text{c}}}$, where the index 'E' corresponds to the relevant edge for each step and the superscript 'old' refers to the GFs obtained from the previous step. We can define $\widehat{V}_{N_{\text{c}},N_{\text{c}}+1} = \widehat{V}_{\text{LR}}$ (electron interactions from the previous to the next cell) and $\widehat{V}_{N_{\text{c}}+1,N_{\text{c}}} = \widehat{V}_{\text{RL}}$ (electron interactions from the next to the previous cell). The

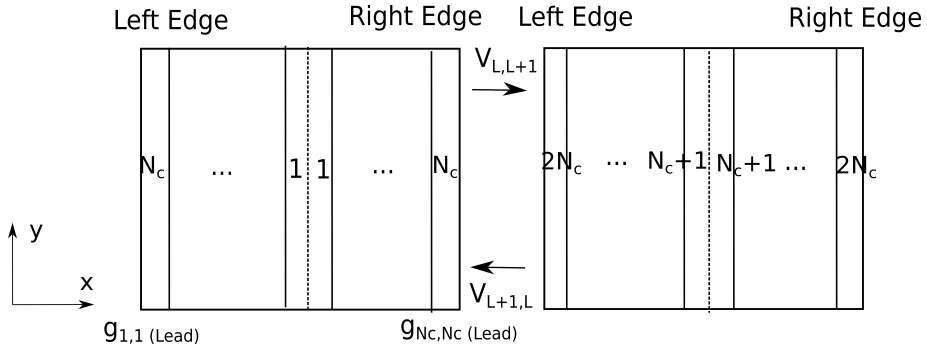

Figure 2.5: *Rubio-Sancho method for doubling the relevant system (left and right lead) for the calculation of surface GFs.*

relevant system is shown in Figure 2.5. We want to find the GFs that correspond to the new connected system $\widehat{G}^{\text{new}}_{1,1} = \widehat{G}_{1,1}$, $\widehat{G}^{\text{new}}_{1,E} = \widehat{G}_{1,2N_c}$, $\widehat{G}^{\text{new}}_{E,1} = \widehat{G}_{2N_c,1}$ and $\widehat{G}^{\text{new}}_{E,E} = \widehat{G}_{2N_c,2N_c}$. For this reason, we made a new derivation for these quantities. Here, $\widehat{G}^{\text{new}}_{E,E}$ can be determined with the use of the Dyson equation (Equation 2.49), as follows:

$$\widehat{G}_{2N_c,2N_c} = \widehat{g}_{2N_c,2N_c} + \widehat{g}_{2N_c,N_c+1}\widehat{V}_{N_c+1,N_c}\widehat{G}_{N_c,2N_c} \tag{2.57}$$

$$\widehat{G}_{N_c,2N_c} = \widehat{g}_{N_c,N_c}\widehat{V}_{N_c,N_c+1}\widehat{G}_{N_c+1,2N_c} \tag{2.58}$$

$$\widehat{G}_{N_c+1,2N_c} = \widehat{g}_{N_c+1,2N_c} + \widehat{g}_{N_c+1,N_c+1}\widehat{V}_{N_c+1,N_c}\widehat{G}_{N_c,2N_c} \tag{2.59}$$

Inserting Equation (2.59) into Equation (2.58), leads to:

$$\begin{aligned}\widehat{G}_{N_c,2N_c} = \widehat{g}_{N_c,N_c}\widehat{V}_{N_c,N_c+1}(\widehat{g}_{N_c+1,2N_c} + \widehat{g}_{N_c+1,N_c+1}\widehat{V}_{N_c+1,N_c}\widehat{G}_{N_c,2N_c}) \rightarrow \\ \widehat{G}_{N_c,2N_c} = (\widehat{I} - \widehat{g}_{N_c,N_c}\widehat{V}_{N_c,N_c+1}\widehat{g}_{N_{]c}+1,N_c+1}\widehat{V}_{N_c+1,N_c})^{-1}\cdot \\ \widehat{g}_{N_c,N_c}\widehat{V}_{N_c,N_c+1}\widehat{g}_{N_c+1,2N_c}\end{aligned} \tag{2.60}$$

Last, inserting Equation (2.60) into Equation (2.57) gives:

$$\begin{aligned}\widehat{G}_{2N_c,2N_c} = \widehat{g}_{2N_c,2N_c} + \widehat{g}_{2N_c,N_c+1}\widehat{V}_{N_c+1,N_c}\cdot \\ (\widehat{I} - \widehat{g}_{N_c,N_c}\widehat{V}_{N_c,N_c+1}\widehat{g}_{N_c+1,N_c+1}\widehat{V}_{N_c+1,N_c})^{-1}\widehat{g}_{N_c,N_c}\widehat{V}_{N_c,N_c+1}\widehat{g}_{N_c+1,2N_c}\end{aligned} \tag{2.61}$$

or else:

$$\widehat{G}^{\text{new}}_{E,E} = \widehat{g}^{\text{old}}_{E,E} + \widehat{g}^{\text{old}}_{E,1}\widehat{V}_{\text{RL}}(\widehat{I} - \widehat{g}^{\text{old}}_{E,E}\widehat{V}_{\text{LR}}\widehat{g}^{\text{old}}_{1,1}\widehat{V}_{\text{RL}})^{-1}\widehat{g}^{\text{old}}_{E,E}\widehat{V}_{\text{LR}}\widehat{g}^{\text{old}}_{1,E} \tag{2.62}$$

For convenience, we defined: $\widehat{t}_1 = \widehat{g}^{\text{old}}_{1,1}\widehat{V}_{\text{RL}}$, $\widehat{t}_2 = \widehat{g}^{\text{old}}_{E,E}\widehat{V}_{\text{LR}}$, $\widehat{A} = (\widehat{I} - \widehat{t}_2\widehat{t}_1)^{-1}\widehat{t}_2\widehat{g}^{\text{old}}_{1,E}$ and

$\widehat{B} = (\widehat{I} - \widehat{t}_1\widehat{t}_2)^{-1}\widehat{t}_1\widehat{g}^{\text{old}}_{E,1}$. With these definitions Equation (2.62) can be written as:

$$\widehat{G}^{\text{new}}_{E,E} = \widehat{g}^{\text{old}}_{E,E} + \widehat{g}^{\text{old}}_{E,1}\widehat{V}_{\text{RL}}\widehat{A} \tag{2.63}$$

Similarly, we determine the GF $\widehat{G}^{\text{new}}_{1,1}$ using Dyson equation (Equation 2.49), as follows:

$$\widehat{G}_{1,1} = \widehat{g}_{1,1} + \widehat{g}_{1,N_\text{c}}\widehat{V}_{N_\text{c},N_\text{c}+1}\widehat{G}_{N_\text{c}+1,1} \tag{2.64}$$

$$\widehat{G}_{N_\text{c}+1,1} = \widehat{g}_{N_\text{c}+1,N_\text{c}+1}\widehat{V}_{N_\text{c}+1,N_\text{c}}\widehat{G}_{N_\text{c},1} \tag{2.65}$$

$$\widehat{G}_{N_\text{c},1} = \widehat{g}_{N_\text{c},1} + \widehat{g}_{N_\text{c},N_\text{c}}\widehat{V}_{N_\text{c},N_\text{c}+1}\widehat{G}_{N_\text{c}+1,1} \tag{2.66}$$

Inserting Equation (2.66) into Equation (2.65) leads to:

$$\widehat{G}_{N_\text{c}+1,1} = \widehat{g}_{N_\text{c}+1,N_\text{c}+1}\widehat{V}_{N_\text{c}+1,N_\text{c}}(\widehat{g}_{N_\text{c},1} + \widehat{g}_{N_\text{c},N_\text{c}}\widehat{V}_{N_\text{c},N_\text{c}+1}\widehat{G}_{N_\text{c}+1,1}) \rightarrow$$

$$\widehat{G}_{N_\text{c}+1,1} = (\widehat{I} - \widehat{g}_{N_\text{c}+1,N_\text{c}+1}\widehat{V}_{N_\text{c}+1,N_\text{c}}\widehat{g}_{N_\text{c},N_\text{c}}\widehat{V}_{N_\text{c},N_\text{c}+1})^{-1}\widehat{g}_{N_\text{c}+1,N_\text{c}+1}\widehat{V}_{N_\text{c}+1,N_\text{c}}\widehat{g}_{N_\text{c},1} \tag{2.67}$$

Last, inserting Equation (2.67) into Equation (2.64) gives:

$$\begin{aligned}\widehat{G}_{1,1} = \widehat{g}_{1,1} + \widehat{g}_{1,N_\text{c}}\widehat{V}_{N_\text{c},N_\text{c}+1}\cdot \\ (\widehat{I} - \widehat{g}_{N_\text{c}+1,N_\text{c}+1}\widehat{V}_{N_\text{c}+1,N_\text{c}}\widehat{g}_{N_\text{c},N_\text{c}}\widehat{V}_{N_\text{c},N_\text{c}+1})^{-1}\widehat{g}_{N_\text{c}+1,N_\text{c}+1}\widehat{V}_{N_\text{c}+1,N_\text{c}}\widehat{g}_{N_\text{c},1}\end{aligned} \tag{2.68}$$

or else:

$$\widehat{G}^{\text{new}}_{1,1} = \widehat{g}^{\text{old}}_{1,1} + \widehat{g}^{\text{old}}_{1,E}\widehat{V}_{\text{LR}}(\widehat{I} - \widehat{g}^{\text{old}}_{1,1}\widehat{V}_{\text{RL}}\widehat{g}^{\text{old}}_{E,E}\widehat{V}_{\text{LR}})^{-1}\widehat{g}^{\text{old}}_{1,1}\widehat{V}_{\text{RL}}\widehat{g}^{\text{old}}_{E,1} \tag{2.69}$$

and using the definitions for $\widehat{t}_1$, $\widehat{t}_2$, $\widehat{A}$ and $\widehat{B}$, we have that:

$$\widehat{G}^{\text{new}}_{1,1} = \widehat{g}^{\text{old}}_{1,1} + \widehat{g}^{\text{old}}_{1,E}\widehat{V}_{\text{LR}}\widehat{B} \tag{2.70}$$

For the term $\widehat{G}^{\text{new}}_{1,E}$ it is:

$$\widehat{G}_{1,2N_\text{c}} = \widehat{g}_{1,N_\text{c}}\widehat{V}_{N_\text{c},N_\text{c}+1}\widehat{G}_{N_\text{c}+1,2N_\text{c}} \tag{2.71}$$

$$\widehat{G}_{N_\text{c}+1,2N_\text{c}} = \widehat{g}_{N_\text{c}+1,2N_\text{c}} + \widehat{g}_{N_\text{c}+1,N_\text{c}+1}\widehat{V}_{N_\text{c}+1,N_\text{c}}\widehat{G}_{N_\text{c},2N_\text{c}} \tag{2.72}$$

We replaced $\widehat{G}_{N_\text{c},2N_\text{c}}$ from Equation (2.60) into Equation 2.72, as follows:

$$\begin{aligned}\widehat{G}_{N_\text{c}+1,2N_\text{c}} = \widehat{g}_{N_\text{c}+1,2N_\text{c}} + \widehat{g}_{N_\text{c}+1,N_\text{c}+1}\widehat{V}_{N_\text{c}+1,N_\text{c}}\widehat{G}_{N_\text{c}+1,1}\cdot \\ (\widehat{I} - \widehat{g}_{N_\text{c},N_\text{c}}\widehat{V}_{N_\text{c},N_\text{c}+1}\widehat{g}_{N_\text{c}+1,N_\text{c}+1}\widehat{V}_{N_\text{c}+1,N_\text{c}})^{-1}\widehat{g}_{N_\text{c},N_\text{c}}\widehat{V}_{N_\text{c},N_\text{c}+1}\widehat{g}_{N_\text{c}+1,2N_\text{c}}\end{aligned} \tag{2.73}$$

Inserting Equation (2.73) into Equation (2.71) leads to:

$$\begin{aligned}\widehat{G}_{1,2N_c} = \widehat{g}_{1,N_c}\widehat{V}_{N_c,N_c+1}[\widehat{g}_{N_c+1,2N_c} + \widehat{g}_{N_c+1,N_c+1}\widehat{V}_{N_c+1,N_c}\cdot \\ (\widehat{I} - \widehat{g}_{N_c,N_c}\widehat{V}_{N_c,N_c+1}\widehat{g}_{N_c+1,N_c+1}\widehat{V}_{N_c+1,N_c})^{-1}\widehat{g}_{N_c,N_c}\widehat{V}_{N_c,N_c+1}\widehat{g}_{N_c+1,2N_c}]\end{aligned} \tag{2.74}$$

or else:

$$\widehat{G}^{\text{new}}_{1,E} = \widehat{g}^{\text{old}}_{1,E}\widehat{V}_{\text{LR}}[\widehat{g}^{\text{old}}_{1,E} + \widehat{g}^{\text{old}}_{1,1}\widehat{V}_{\text{RL}}(\widehat{I} - \widehat{g}^{\text{old}}_{E,E}\widehat{V}_{\text{LR}}\widehat{g}^{\text{old}}_{1,1}\widehat{V}_{\text{RL}})^{-1}\widehat{g}^{\text{old}}_{E,E}\widehat{V}_{\text{LR}}\widehat{g}^{\text{old}}_{1E}] \tag{2.75}$$

and the use of definitions $\widehat{t_1}$, $\widehat{t_2}$ and $\widehat{A}$ leads to:

$$\widehat{G}^{\text{new}}_{1,E} = \widehat{g}^{\text{old}}_{1,E}\widehat{V}_{\text{LR}}[\widehat{g}^{\text{old}}_{1,E} + \widehat{t}_1\widehat{A}] \tag{2.76}$$

For the term $\widehat{G}^{\text{new}}_{E,1}$ it is:

$$\widehat{G}_{2N_c,1} = \widehat{g}_{2N_c,N_c+1}\widehat{V}_{N_c+1,N_c}\widehat{G}_{N_c,1} \tag{2.77}$$

$$\widehat{G}_{N_c,1} = \widehat{g}_{N_c,1} + \widehat{g}_{N_c,N_c}\widehat{V}_{N_c,N_c+1}\widehat{G}_{N_c+1,1} \tag{2.78}$$

Inserting $\widehat{G}_{N_c+1,1}$ from Equation (2.67) into Equation 2.78 leads to:

$$\begin{aligned}\widehat{G}_{N_c,1} = \widehat{g}_{N_c,1} + \widehat{g}_{N_c,N_c}\widehat{V}_{N_c,N_c+1}\cdot \\ (\widehat{I} - \widehat{g}_{N_c+1,N_c+1}\widehat{V}_{N_c+1,N_c}\widehat{g}_{N_c,N_c}\widehat{V}_{N_c,N_c+1})^{-1}\widehat{g}_{N_c+1,N_c+1}\widehat{V}_{N_c+1,N_c}\widehat{g}_{N_c,1}\end{aligned} \tag{2.79}$$

Inserting Equation 2.79 into Equation (2.77), as follows:

$$\begin{aligned}\widehat{G}_{2N_c,1} = \widehat{g}_{2N_c,N_c+1}\widehat{V}_{N_c+1,N_c}[\widehat{g}_{N_c,1} + \widehat{g}_{N_c,N_c}\widehat{V}_{N_c,N_c+1}\cdot \\ (\widehat{I} - \widehat{g}_{N_c+1,N_c+1}\widehat{V}_{N_c+1,N_c}\widehat{g}_{N_c,N_c}\widehat{V}_{N_c,N_c+1})^{-1}\widehat{g}_{N_c+1,N_c+1}\widehat{V}_{N_c+1,N_c}\widehat{g}_{N_c,1}]\end{aligned} \tag{2.80}$$

or else:

$$\widehat{G}^{\text{new}}_{E,1} = \widehat{g}^{\text{old}}_{E,1}\widehat{V}_{\text{RL}}[\widehat{g}^{\text{old}}_{E,1} + \widehat{g}^{\text{old}}_{E,E}\widehat{V}_{\text{LR}}(\widehat{I} - \widehat{g}^{\text{old}}_{1,1}\widehat{V}_{\text{RL}}\widehat{g}^{\text{old}}_{E,E}\widehat{V}_{\text{LR}})^{-1}\widehat{g}^{\text{old}}_{1,1}\widehat{V}_{\text{RL}}\widehat{g}^{\text{old}}_{E,1}] \tag{2.81}$$

and with the definitions $\widehat{t_1}$, $\widehat{t_2}$ and $\widehat{B}$ it is:

$$\widehat{G}^{\text{new}}_{E,1} = \widehat{g}^{\text{old}}_{E,1}\widehat{V}_{\text{RL}}[\widehat{g}^{\text{old}}_{E,1} + \widehat{t}_2\widehat{B}] \tag{2.82}$$

Equations (2.63), (2.70), (2.76) and (2.82) calculate the surface GFs $\widehat{G}_{\text{SL}}$ and $\widehat{G}_{\text{SR}}$ for each iteration. If for each element of the GFs (2.63), (2.70), (2.76) and (2.82) it is $|\widehat{G}^{[n]} -$

$\widehat{G}^{[n-1]}| \leq \epsilon_{\text{GF}}$ for the n-th step, the recursive calculations stop. Here, ϵ_{GF} is chosen here to be 10^{-8}. After convergence is achieved, $\widehat{G}_{E,E} = \widehat{G}_{\text{SL}}$ is the surface GF for the left lead and $\widehat{G}_{1,1} = \widehat{G}_{\text{SR}}$ is the surface GF for the right lead respectively.

In order to include the contributions from the leads, we calculated the GF of the last cell ((N_{c}-th cell) as follows:

$$\widehat{G}_{N_{\text{c}},N_{\text{c}}} = [(E + i\eta)\widehat{I}_{N_{\text{c}},N_{\text{c}}} - \widehat{H}_{N_{\text{c}},N_{\text{c}}} - \widehat{\Sigma}_{L}^{+} - \widehat{\Sigma}_{R}^{+}]^{-1} \tag{2.83}$$

where the retarded and advanced self-energy functions from the left $\Sigma_{\text{L}}^{+}, \Sigma_{\text{L}}^{-}$ and right lead $\Sigma_{R}^{+}, \Sigma_{R}^{-}$ are:

$$\widehat{\Sigma}_{\text{L}}^{+} = \widehat{V}_{\text{L}}^{\dagger}\widehat{G}_{\text{SL}}^{+}\widehat{V}_{\text{L}}, \quad \widehat{\Sigma}_{\text{L}}^{-} = \widehat{V}_{\text{L}}^{\dagger}\widehat{G}_{\text{SL}}^{-}\widehat{V}_{\text{L}} \tag{2.84}$$

$$\widehat{\Sigma}_{\text{R}}^{+} = \widehat{V}_{\text{R}}\widehat{G}_{\text{SR}}^{+}\widehat{V}_{\text{R}}^{\dagger}, \quad \widehat{\Sigma}_{\text{R}}^{-} = \widehat{V}_{\text{R}}\widehat{G}_{\text{SR}}^{-}\widehat{V}_{\text{R}}^{\dagger} \tag{2.85}$$

$\widehat{G}_{\text{SL}}^{+}$ and $\widehat{G}_{\text{SR}}^{+}$ are the retarded surface GFs for the left and right lead and $\widehat{G}_{\text{SL}}^{-}$ and $\widehat{G}_{\text{SR}}^{-}$ are the advanced surface GFs for the left and right lead respectively. The matrices $\widehat{V}_{\text{L}}$ and $\widehat{V}_{\text{R}}$ correspond to the electron interactions between the central device and the left and right lead respectively.

2.4.3 Total DOS and Local DOS

In order to find TDOS, we added the contributions from each cell according to Equation (2.56). For N_{c}-th cell we included the contribution from the leads by obtaining the surface greens functions $\widehat{G}_{\text{SL}}$ and $\widehat{G}_{\text{SR}}$ and including them in the GF $\widehat{G}_{N_{\text{c}},N_{\text{c}}}$, as follows:

$$TDOS_{\text{new}} = TDOS_{\text{old}} - \tfrac{1}{\pi} Im\, Tr\left(\widehat{G}_{N_{\text{c}},N_{\text{c}}} \cdot (\widehat{A}_{N_{\text{c}}} + \widehat{I}_{N_{\text{c}},N_{\text{c}}})\right) \tag{2.86}$$

where $A_{N_{\text{c}}}$ was obtained from Equation (2.54), where the matrix elements $\widehat{V}_{i,i-1}$ and $\widehat{V}_{i-1,i}$ correspond to the electron interactions between the N_{c}-th cell and the leads for cutoff distance **d**=1.82 Å for the xy-plane. Last, TDOS was normalized by the number of atoms in the system.

Similar to the calculation of TDOS, for the calculation of LDOS we also used the GF $\widehat{g}_{i,i}^{[i]}$ in Equation (2.55) and we included the contribution from the leads for the GF of the N_{c}. By using the GFs $\widehat{g}_{i,i}^{[i]}$, we determined the GFs $\widehat{G}_{i,i}$ for each cell i, in order to take into

account the contributions from all the atoms, as follows:

$$\widehat{G}_{i,i} = \widehat{g}^{[i]}_{i,i} + \widehat{g}^{[i]}_{i,i}\widehat{V}_{i,i+1}\widehat{g}^{[i+1]}_{i+1,i+1}\widehat{V}_{i+1,i}\widehat{g}^{[i]}_{i,i} \tag{2.87}$$

We obtained LDOS by replacing the GFs from Equation (2.87) for each atom j into the following equation:

$$LDOS_j = -\tfrac{1}{\pi} Im\,(\widehat{G}_{j,j}) \tag{2.88}$$

where $\widehat{G}_{j,j}$ refers to the GF of the individual atom j.

2.4.4 Transmission

Transmission, $\widehat{T}$, shows the probability that a particle (electron) passes through a barrier (in our study from the Left to the Right Lead, Subsection 2.4.2). For the single channel case, the value of transmission is between zero and one, where zero indicates no transmission and one complete transmission. Transmission can be greater than one if more than one channel is available. In practice, we are looking at transmissions for periodic systems and we divide by the cell width. The transmission, $\widehat{T}$, across hBLG (Central Device) is calculated using the Caroli formula [133]:

$$\widehat{T} = \mathrm{Tr}(\widehat{\Gamma}_{\mathrm{L}}\widehat{G}_{+}\widehat{\Gamma}_{\mathrm{R}}\widehat{G}_{-}) \tag{2.89}$$

where the retarded GF $\widehat{G}_{+}$ and the advanced GF $\widehat{G}_{-}$ correspond to atoms of the N_{c}-th cell in the central device (Equation (2.83) gives the expression for the retarded GF of the N_{c}-th cell). Here, $\widehat{\Gamma}_{\mathrm{L}}$ and $\widehat{\Gamma}_{\mathrm{R}}$ are the broadening matrices for the left and right lead respectively, which account for the broadening effect. The broadening effect arises from the uncertainty principle in quantum systems. The energy levels have a finite uncertainty in energy due to the limited lifetime of the excited states. The broadening matrices $\widehat{\Gamma}_{\mathrm{L}}$ and $\widehat{\Gamma}_{\mathrm{R}}$ are related to the self-energies $\widehat{\Sigma}^{+}_{\mathrm{L}}$, $\widehat{\Sigma}^{-}_{\mathrm{L}}$, $\widehat{\Sigma}^{+}_{\mathrm{R}}$ and $\widehat{\Sigma}^{-}_{\mathrm{R}}$ (self-energies are explained in Subsection 2.4.2), as follows:

$$\widehat{\Gamma}_{\mathrm{L}} = i[\widehat{\Sigma}^{+}_{\mathrm{L}} - \widehat{\Sigma}^{-}_{\mathrm{L}}], \quad \widehat{\Gamma}_{\mathrm{R}} = i[\widehat{\Sigma}^{+}_{\mathrm{R}} - \widehat{\Sigma}^{-}_{\mathrm{R}}] \tag{2.90}$$

Thus, transmission, $\widehat{T}$, can be written as:

$$\widehat{T} = \mathrm{Tr}(i[\widehat{\Sigma}_{\mathrm{L}}^{+} - \widehat{\Sigma}_{\mathrm{L}}^{-}]\widehat{G}_{+} i[\widehat{\Sigma}_{\mathrm{R}}^{+} - \widehat{\Sigma}_{\mathrm{R}}^{-}]\widehat{G}_{-}) \tag{2.91}$$

2.5 Summary of Chapter

In this Chapter we presented the mathematical and computational tools that were used for the implementation of our calculations throughout this thesis. We explained the theoretical formalism of DFT calculations. We also included the TB formalism, which is a semi-empirical method. Next, we introduced the concept of the RGF method which is computationally very efficient. We also showed the usefulness of the RGF method for the calculation of TDOS, LDOS, and transmission, T.

Chapter 3 Strain-induced stacking transition in graphene

3.1 Introduction

Strain can have a considerable effect on the structural, electronic, and transport properties of 2D materials and heterostructures. Here, we focused on the effect of heterostrain on the structural properties of BLG. Uniaxial and biaxial heterostrain can modify its stacking arrangement of BLG, as already mentioned in Subsection 1.2.4. We investigated the strain-induced stacking transition in hBLG, by performing DFT calculations and investigated the interplay between an externally applied heterostrain and the resulting stacking. This way, we determined how a strain applied to one layer (bottom layer or L1) is transferred to a 'free' layer (top layer or L2) and at what critical strain the ground-state AB stacking is disrupted (Figure 3.1). This is an alternative way to twistronics for engineering stacking order, which affects the electronic, transport, and optical properties of BLG near this critical point, due to the change in stacking order.

Uniaxial strain can be applied on the L1 layer of BLG experimentally with its deposition on a flexible substrate (Subsection 1.2.4). Raman spectroscopic studies showed that the maximum strain that can be transferred to MLG through a flexible polymer substrate is 1.3%-1.8% [59, 64–67]. However, there are some ways to increase the strain applied to MLG through the straining of the substrate, by adding formvar resins as a buffer layer to this system [68]. With this method, the maximum strain that can be transferred to MLG is 3.3%, which is quite large.

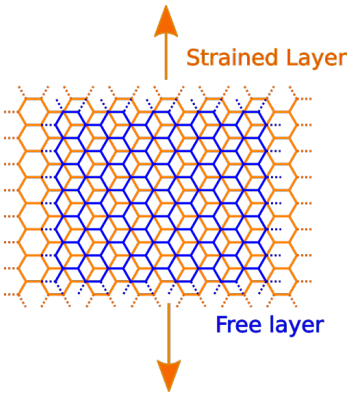

Figure 3.1: *Structure of the BLG system considered in this work, where uniaxial strain is applied only to the L1 layer and we consider strained and unstrained configurations of the L2.*

Androulidakis et al. used a flexible substrate to apply heterostrain on BLG [61]. They showed that for uniaxial tensile strain up to 1% on the flexible substrate, the strain transfer between the substrate and the L1 layer of BLG is always larger than the strain transfer between the two graphene layers by three to four times. Also, they showed that the strain transfer depends on the amount of the applied strain on the substrate.

There are two energetic costs that determine the final stacking of BLG concerning the applied heterostrain, the cost of straining the 'free' layer and the cost of changing the initial ground state AB stacking. For small amounts of strain applied to the L1, the 'free' layer is expected to strain by the same amount, as the energetic cost of straining is small compared to that of breaking uniform AB stacking. However, at a certain critical value of applied strain, which is not known yet, the energetic cost of maintaining strain in the 'free' layer exceeds the cost of breaking AB stacking. At this point, strain is released in the free layer as the energy benefit in doing so is greater than the energy penalty to be paid for a less-than-ideal stacking configuration. At this critical strain, a transition between a uniform AB stacking order and a non-uniform stacking will occur, together with the formation of Moiré superlattices.

Theoretical studies showed the possibility of commensurate-incommensurate transition in BLG with the one layer being stretched or compressed along the AC direction, using the Frenkel-Kontorova model and DFT calculations [71]. For -0.39% compressive heterostrain, there is a need for reducing the elastic energy of the system, which leads

to the first incommensurability defect. Figure 3.2 depicts the energy difference of total energies of BLG for the incommensurate state with a single incommensurate defect and without per unit width of the layers perpendicular to the elongation as a function of the relevant elongation. This indicates that as the elongation increases, the energy difference is decreased.

Experimentally, Frank et al. performed Raman spectroscopic measurements for BLG which was deposited on a polymer substrate and they found an uneven stress transfer between the two graphene layers for large strain [66]. This was also verified theoretically by Wang et al., who also performed Molecular Dynamics simulations for a graphene flexible substrate and a graphene flake connected to it. They found that for a large value of applied uniaxial heterostrain on the graphene flexible substrate, the relevant stacking was non-uniform due to the lattice mismatch [134]. However, the critical strain threshold that this happens is not known yet, and we performed DFT calculations to find it.

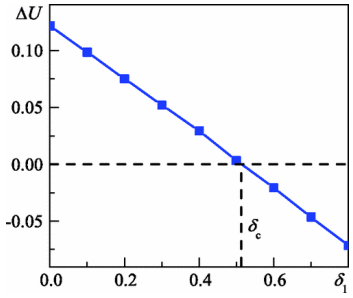

Figure 3.2: *Difference in the total energies of BLG for the incommensurate state with a single incommensurate defect and without per unit width of the layers perpendicular to the elongation as a function of the relevant elongation. Figure adapted from [71].*

Section 3.2 has the computational details of the DFT calculations performed to find the critical strain of the transition and the relevant results are included in Section 3.3. We have used a simple model to determine approximately the critical strain for the transition. Taking into account this approximate value of critical strain, we did the actual DFT calculations for values of strain close to this value. To overcome restrictions caused by the use of periodic boundary conditions in the graphene plane, the hBLG system was approximated using a hydrogen-terminated armchair graphene nanoribbon (AGNR) adsorbed on top of an MLG. The dangling carbon bonds at the AGNR edges were passivated with hydrogen atoms. Section 3.4 has a discussion of these results, concerning the feasibility of this study

to experimental methods as well as its potential applications.

3.2 Computational details

DFT calculations were performed using VASP-5.4.1. The Perdew-Burke-Ernzerhof (PBE) [135] parameterization of the GGA functional was employed and the vdW interactions were included using the D2 semi-empirical method of Grimme. The plane wave basis set was converged using a 950 eV energy cutoff. A $13 \times 21 \times 1$ k-point mesh was used to determine the total energies of both perfect unstrained MLG and BLG for the DFT calculations. All structures were optimized until the residual forces were less than 0.01 eV/Å and a vacuum layer of at least 11.5 Å was included in the direction normal to MLG or BLG to ensure no spurious interactions between repeating slabs. The GGA-calculated lattice constants of MLG and BLG were both found to be 2.47 Å, in good agreement with the experimental value of 2.46 Å. The interlayer distances in AB- and AA-stacked BLGs were found to be 3.37 Å and 3.5 Å, respectively, in good agreement with previous theoretical [136] and experimental studies [137, 138].

Heterostrain was then introduced by straining the MLG along the ZZ direction. A $21 \times 5 \times 1$ k-point mesh was sufficient to converge the total energy of all the composite structures (AGNR/MLG) considered. A distance of at least 12.5 Å was maintained between periodic replicas of adsorbed AGNRs to ensure that they do not interact. To achieve this, the size of the L1 layer is increased for wider ribbons. The optimal AGNR width was determined by comparing the stacking-dependent AGNR binding energy (E_B) to the stacking-dependent binding energy of BLG. These quantities are normalized by the overlap between the two layers (Equation (3.1)), in order to allow a meaningful comparison between ribbons of different widths. In this case, the in-plane positions of the two central atoms of the AGNR were held fixed at the chosen stacking and all other AGNR atoms were allowed to relax both in-plane and out-of-plane. To determine the lowest energy stacking configuration for different heterostrains, the carbon-hydrogen bonds and the interlayer distance between the MLG and the AGNR were relaxed while the in-plane positions of all other atoms were held fixed.

The interlayer distance is found to largely follow the stacking order, as expected. Beyond its role in determining the stacking order, a strain of order 1% has a negligible additional effect (<0.01 Å) on the interlayer distance. This is at least an order of magnitude smaller than the variation due to stacking or due to the finite width of the ribbon in composite systems. A reduced interlayer distance is found in our composite systems compared to infinite bilayers (3.25 Å versus 3.37 Å for AB-stacked regions), similar to the trend noted previously in bilayer GNRs.

3.3 Results

To determine the critical strain for which a transition occurs from a uniformly strained BLG with AB stacking to a heterostrained system with disrupted stacking, we compared the energetics of two limiting cases: when L2 layer either adopts the same strain as that applied to L1 or it remains completely unstrained. Possible intermediate scenarios, where the layer L2 adopts a non-zero strain different from that in the L1 layer or displays a non-uniform strain distribution, are not considered in this work due to their high computational cost. Similarly, in order to maintain periodicity for the DFT calculations, we neglect the role of contraction in the direction perpendicular to the applied strain. This is equivalent to setting Poisson ratio ν=0.

3.3.1 Simple Model

We used a simple model to determine approximately the amount of critical strain required for the transition and then we performed DFT calculations for a strain range close to this approximate critical value. There are two principal energy costs, due to strain (ΔE_{strain}) and stacking (ΔE_{stack}), which determine the behavior of the L2 layer when uniaxial strain is applied to the L1. To get a rough estimate of where the transition between a strained and unstrained L2 layer occurs, we can compare the expected energy costs of straining the L2 layer in isolation, and of breaking AB stacking in an unstrained BLG system.

We first consider $\Delta E_{\text{strain}} = E - E_{\text{unstrained}}$, the energy cost associated with straining the L2 layer away from its relaxed structure to match the strain applied to L1. The energy cost

of straining a graphene layer increases with the amount of strain considered, as shown in Figure 3.3 (a) for MLG with strain applied along the ZZ direction. Here, ΔE_{strain} displays almost identical behavior in AA- and AB-stacked BLG, once normalized by the number of atoms in the system, and for strains along the AC direction in all three systems, with a maximum variation of only 2.8 meV per atom. Since ΔE_{strain} is not significantly affected by the strain direction, or the nature of the stacking in BLG systems, the curve in Figure 3.3 (a) should also be an excellent approximation to the energetic cost of straining a single layer in BLG in the absence of stacking effects.

If the amount of strain is different in the two layers, the system is no longer able to maintain energetically favorable AB stacking and instead must display a modulation of the stacking order with an associated energy cost $\Delta E_{\text{stack}} = E - E_{\text{AB}}$. Although the modulation wavelength depends on the strain mismatch, the energy cost per atom is roughly constant, as a similar range of stackings will occur for any mismatch. Therefore, ΔE_{stack} should not depend sensitively on the strain applied to the L1, and we approximate it by considering different stacking configurations in unstrained BLG. Figure 3.3 (b) shows the energetic cost of rigidly shifting one graphene layer over the other along ZZ or AC directions, starting from either an initial AB or AA stacking. As the layers are shifted, the in-plane positions of atoms are held fixed to maintain the desired stacking configuration, but the interlayer distance is allowed to relax. Any shift away from AB stacking results in a positive ΔE_{stack}, confirming that this is the preferred configuration. Here, ΔE_{stack} is the maximum for AA stacking with a value of 5.84 meV/atom, in excellent agreement with the results of DFT calculations in Reference [48]. The stacking modulation arising from heterostrain contains a combination of various stackings, and the corresponding ΔE_{stack} can be approximated as an appropriately weighted average of the values appearing in Figure 3.3 (b).

Comparing Figures 3.3 (a) and (b) allows us to understand the interplay between strain and stacking in hBLG. For small strains applied to the L1, $\Delta E_{\text{strain}} \ll \Delta E_{\text{stack}}$, and it is energetically favorable for the L2 layer to adopt the same strain. However, as the strain applied to the L1 layer is increased, the cost of uniformly straining the L2 layer eventually balances the cost of breaking AB stacking. A transition occurs above this critical strain, releasing the strain in the L2 layer and introducing a modulation of the stacking order.

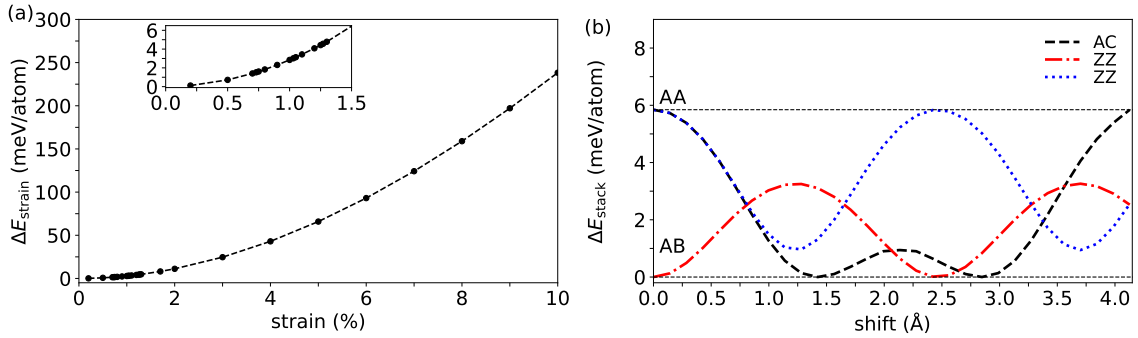

Figure 3.3: *(a) ΔE_{strain} per atom as a function of applied ZZ uniaxial strain in MLG. (b) ΔE_{stack} per atom as a function of the relative shift between layers in BLG for different initial stackings (AA and AB stackings). Shifts along both ZZ and AC directions are shown.*

The maximum possible value of critical strain is restricted by the finite range of ΔE_{stack}: the maximum possible cost of breaking AB stacking (i.e., $\Delta E^{AA}_{\text{stack}} \sim 5.84$ meV/atom), corresponds to a strain of 1.98%. In reality, the mix of different stackings that occur in a hBLG will give $0 < \Delta E_{\text{stack}} < \Delta E^{AA}_{\text{stack}}$. For an even distribution of stackings between AB and AA, we can estimate $\Delta E_{\text{stack}} \sim \frac{1}{2}\Delta E^{AA}_{\text{stack}}$, corresponding to a critical strain of 1.36%. Uneven stacking distributions can occur if the considered strain excludes certain stackings, or if a non-uniform strain distribution is allowed in the L2. However, even accounting for a significant reduction in ΔE_{stack} due to these effects does not dramatically change the expected critical strain. For example, assuming $\Delta E_{\text{stack}} \sim \frac{1}{4}\Delta E^{AA}_{\text{stack}}$ still gives a critical strain of 0.94%. The results of this simple model strongly suggest that the critical strain is near 1%, and that uniform AB stacking will be broken when larger strains are applied to the L1.

3.3.2 AGNR on strained MLG

DFT calculations of hBLGs will now be used to test the prediction of this simple model that the critical strain occurs near 1%. However, periodic boundary conditions enforce a commensurability condition when dealing with two infinite graphene sheets. Although neglecting contraction in the transverse direction (ν=0) simplifies matters considerably, only certain values of strain would be achievable. The unit cells of hBLG are different in size and depend on the value of heterostrain, as atomic structures showed for 11.1% and 20%

uniaxial strain applied along the ZZ direction on L1 layer of BLG [139]. Furthermore, very large supercells would be required to investigate the relevant strain range, because 1% strain requires 101 cells of the L2 layer and 100 cells of the strained layer L1. Getting sufficient resolution to determine the critical strain quickly becomes computationally prohibitive.

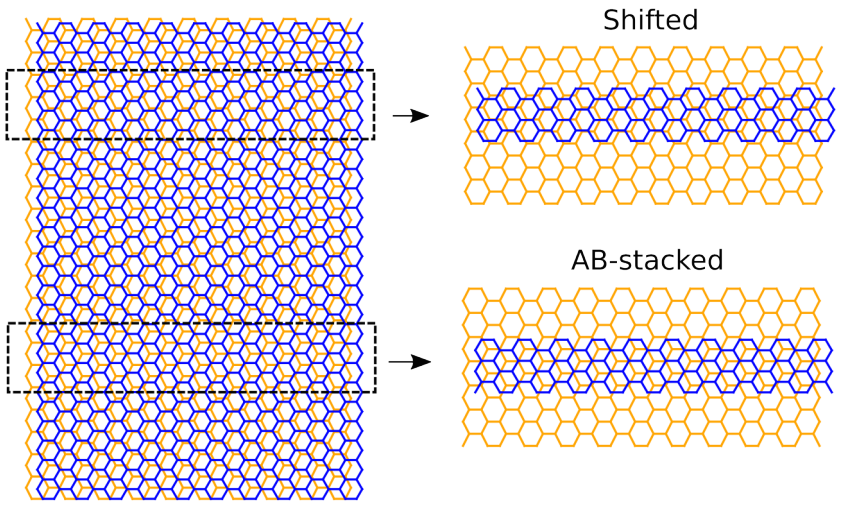

Figure 3.4: (Left:) *Structure of BLG when the bottom (orange) layer is uniaxially strained by 15% along the ZZ (vertical) direction. A modulation of the stacking is clearly visible.* (Right:) *The systems considered in this work, where AB and shifted regions of the BLG system are represented by finite-width AGNRs.*

To overcome this constraint, we instead investigate the interplay of strain and stacking in a system where different regions of the L2 layer are modeled by finite-width AGNRs. This is shown schematically on the left side of Figure 3.4, for an exaggerated strain of 15% along the ZZ (vertical) direction applied to the L1. A 1D Moiré pattern is evident in the full BLG with regions of AB stacking (lower dashed box) separated by other stacking types. Due to the ZZ strain direction and ν=0, no AA stacking occurs and the furthest stacking from AB is that in the upper dashed box, which we denote as 'Shifted' and corresponds to rigidly shifting one layer of unstrained BLG by half a graphene lattice constant in the ZZ direction. We aim to determine the energetics of the complete system (left-hand side) by modeling different portions of it by a finite-width ribbon adsorbed onto an infinite L1 layer (right-hand side). The AGNR can be rigidly shifted over the continuous L1 layer to

approximate the different stackings that occur in a hBLG system. As the L2 layer is no longer continuous, but now consists of a periodic array of AGNRs, we can consider different strains in each layer using a constant-size supercell. We consider hydrogen-passivated AGNRs to circumvent features including unpassivated bonds and localized edge states. These may occur in certain AGNRs but are not expected in extended bilayer systems. It was found that the width dependence does not experience the hyperbolic expected trend in the band gap for AGNRs, using the extended Hückel theory [140]. Also, zigzag GNRs (ZGNRs) have localized edge states, as TB calculations indicated [141, 142]. For our calculations, the relaxed structure of the H-passivated 6-AGNR/MLG system, with the periodic unit cell is shown by the grey box in Figure 3.5.

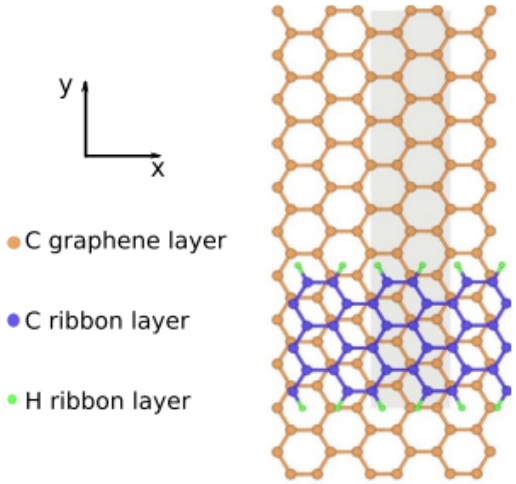

Figure 3.5: *Relaxed structure of the H-passivated 6-AGNR/MLG system, with periodic unit cells shown by the grey box.*

We approximated the two graphene layers with one infinite graphene sheet and one graphene nanoribbon adsorbed on top of it, to study the effects of stacking on the energetics, but we considered multiple stacking configurations for the AGNR to represent different sections of the BLG setup. To assess the reliability of this model, we reproduced the binding energy E_{B} between two graphene layers of the approximate MLG/AGNR system and the perfect BLG for various stackings. We used this approximate system because in this study we are only interested in the energetic aspects and this approximate system would not give good results, necessarily, for the study of electronic properties. Other DFT studies concerning the electronic properties of hBLG have considered the full unit cells, which

restricted them to certain strain values [96, 139]. We finally found that the approximate system indeed captures the important energetic aspects that arise due to different stackings. The choice of AGNR width is determined by that which best approximates the stacking-dependent E_{B} of BLG at a reasonable computational cost. To meaningfully compare E_{B} in BLG and the n-AGNR/MLG systems we normalise E_{B} by the number of carbon atoms in the top-layer, N_{c}, as follows:

$$\beta = \frac{E_{\mathrm{B}}}{N_{\mathrm{c}}} \tag{3.1}$$

Figure 3.6 (a) shows how β varies as the L2 layer is rigidly shifted along the AC direction from AA to AB alignment with the L1. The dashed black curve shows β for BLG while the other curves show β for the approximate n-AGNR/MLG systems with n=5,. . . , 10. While there is an offset between the BLG E_{B} and the AGNR/MLG E_{B}, this offset is approximately constant across all stackings between AA and AB. For widths in excess of n=6, the error is less than 10%. Figures 3.6 (b) shows the E_{B} difference between AA and AB stackings, $\beta_{\mathrm{AA}} - \beta_{\mathrm{AB}}$, as a function of width n, compared to the corresponding quantity for BLG (dashed line). Thus, the finite size of the ribbon model is suitable for studying the effects of stacking on the energetics, but for the study of electronic, transport or optical properties it is required to use the full unit cells of the hBLG system. Agreement between the BLG and AGNR/MLG systems improves in general with the increase of n, but non-uniformly due to different behavior of ribbons with widths n=3q, 3q+1 and 3q+2, where q=1, 2, 3, ... Similar trends have been noted, for example, for the band gap of AGNRs [143]. The odd-even effect states that certain properties alternate between odd and even values. Therefore, there is not a strict ‘odd-even’ effect, but there is a period 3 oscillation. The TB calculations showed the lowest band gap (almost zero) for n=3q+2, a bigger band gap for n=3q, and an even higher one for n=3q+1 [143]. As we are interested in how stacking changes the energetics, and not the absolute magnitude of the E_{B}, the 6-AGNR is deemed sufficiently wide for our purposes.

To estimate the critical strain in hBLG using the 6-AGNR/MLG system, we consider the energy difference, ΔE_X, between strained and unstrained AGNR layers, for different stackings (X=AB, shifted). We emphasize that it is the *unstrained* case that gives rise to broken stacking, due to the strain applied to the L1, whereas the *strained* case restores AB

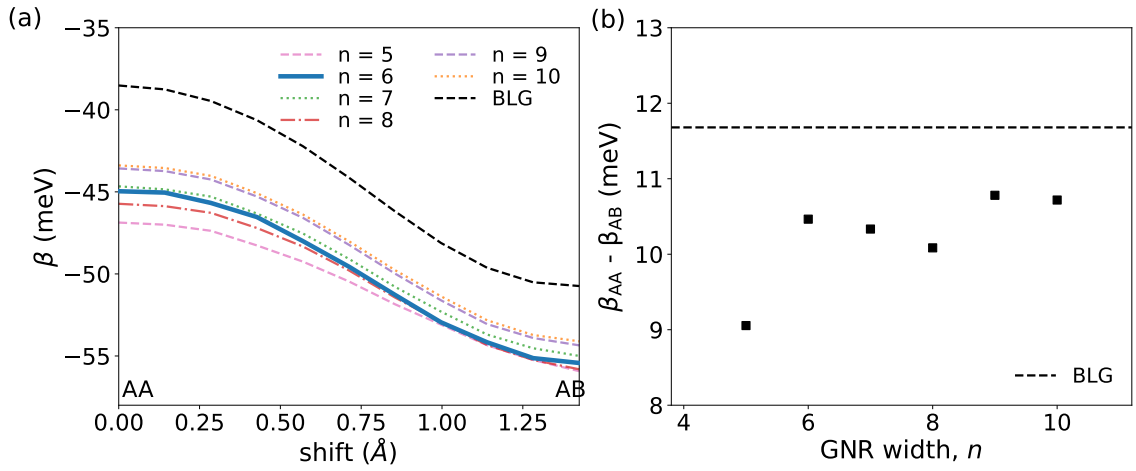

Figure 3.6: *(a) Plot of E_B (per overlap atom) β as a function of stacking for different width n-AGNR/MLG systems, compared to that for infinite BLG. (b) Energy difference $\beta_{AA} - \beta_{AB}$ as a function of width n for the approximate system n-AGNR/MLG, with the black dashed line showing the corresponding BLG result.*

stacking by matching the strain in both layers. The energy difference between strained and unstrained AGNR layers is then given by:

$$\Delta E = E_{\text{AB, strain}} - E_{X,\text{unstrain}} \,, \tag{3.2}$$

where we note that the energy of the final state $E_{\text{AB, strain}}$ is the same in each case, as AB stacking has been restored. Here, $E_{X,\text{unstrain}}$ corresponds to the case that MLG is strained and AGNR is unstrained, with the stacking, X, set by fixing the positions of the central carbon atoms of the AGNR. The in-plane positions of the AGNR carbon atoms are held fixed as determined by the strain and stacking, while the hydrogen-carbon bonds and the interlayer distance are allowed to relax.

The full heterostrained system is considered as an average of the two stacking extremes, AB and Shifted (more general cases will be discussed later), as follows:

$$\Delta E_{\text{av}} = E_{\text{AB, strain}} - \tfrac{1}{2}(E_{\text{AB, unstrain}} + E_{\text{shifted, unstrain}}). \tag{3.3}$$

Negative values of ΔE_{av} imply that the L2 layer prefers to be strained so that the bilayer system remains AB-stacked. Positive values indicate that the L2 layer prefers to be unstrained, and the system adopts a non-uniform stacking profile. Figure 3.7 shows ΔE and

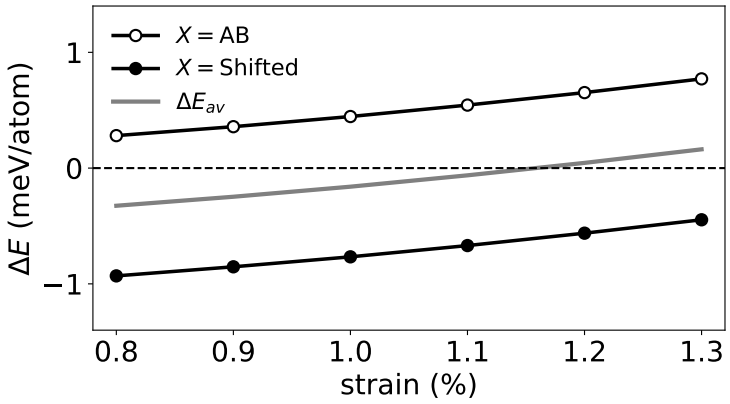

Figure 3.7: *Energy difference ΔE between the strained and unstrained L2 geometries as a function of ZZ uniaxial strain applied to the L1. In the strained case, the layers are AB-stacked, whereas in the unstrained case, different stackings are possible, with different contributions to the ΔE. These calculations were performed using the 6-AGNR/MLG system, and the averaged curve indices a critical strain of $\varepsilon \sim$1.2%.*

ΔE_{av}, as a function of the applied strain along ZZ direction. The curve for the AB-stacked AGNR/MLG system shows that it prefers to be unstrained, i.e., that it is energetically favorable for the AGNR to break perfect AB stacking, instead of maintaining a strain of between 0.8%-1.3%. This is not surprising, as the stacking mismatch is not too significant in this part of the modulated structure (Figure 3.4). However, in the Shifted region, the stacking deviates furthest from AB when the L2 layer is unstrained, and the associated ΔE curve shows that a strained, uniform AB stacking is preferred. The overall preference of the system is a competition between these different regions. For a uniform distribution of stackings in the modulated structure, the averaged case shown by the grey curve in Figure 3.7 indicates that a transition occurs at a critical strain of $\varepsilon \sim$1.2%. This is in very good agreement with the estimate given by the simple model.

3.4 Discussion

For a heterostrain to occur a greater transfer of strain is required between the polymer substrate and the bottom graphene layer than between the two graphene layers (Section 3.1). This is the case observed experimentally by Raman spectroscopic measurements for AB-stacked BLG, compared to MLG [144], with the strain transfer between the substrate

and the L1 layer to be larger than the strain transfer between the two layers [61]. Modulated stacking profiles in BLG systems lead to a wide range of new properties, particularly when combined with an interlayer bias, as already mentioned in Subsection 1.2.3. Such an interlayer bias will open a band gap in regions with particular stackings, leading to a complex distribution of gapped and conducting regions that follow the underlying stacking pattern. This has been widely investigated in twisted bilayers where, for example, networks of 1D topological channels have been found between gapped AB- and BA- stacked regions of the Moiré pattern, which have been investigated both with the continuum theory calculations [54, 145] and STS measurements [102].

Heterostrained, untwisted BLG, as considered here, could potentially host a similar range of phenomena. The schematic structure in Figure 3.4 shows the formation of a 1D Moiré pattern with different stacking profiles, which would also create a spatially varying band gap landscape in the presence of an interlayer bias, as we discuss in the Chapter 4. To maintain periodicity for our calculations, we neglected the Poisson contraction ν perpendicular to the direction of the applied strain. Including such a contraction would lead to a 2D modulation of the stacking pattern and a more complete analogy with twisted systems. We note that setting $\nu \neq 0$ (Chapter 5) allows a wider range of stackings when the free layer is unstrained than for the simple 1D modulation considered in Figures 3.4 and 3.7. In particular, more energetically unfavorable stackings, such as AA, are now possible, which may slightly increase the critical strain due to the increased energetic cost of breaking uniform stacking.

Last, the estimate of the critical strain in this work is based on the L2 layer being either unstrained or uniformly adopting the same strain as the L1. We have not considered, for example, an intermediate value of strain in the free layer. We expect such cases to be less energetically favorable than the unstrained free layer. This is because such cases will have to pay both strain and stacking-related energy costs, and the latter is expected to be largely strain-independent, as discussed in Section 3.3.1. Therefore the minimum energy heterostrained system should be that which minimizes ΔE_{strain}, namely that with an unstrained free layer. Due to the periodicity constraints of our calculations, we also have not been able to explicitly consider the role of non-uniform strain in the free layer, as

discussed in Section 3.1.

3.5 Summary of Chapter

In this Chapter we showed the existence of a critical strain $\varepsilon \sim 1\%$ applied to one layer of BLG, which was supported by DFT calculations. First, we considered the energetic costs of strain and stacking independently in infinite, periodic systems, by doing two simple approximations to determine the range of critical strain that exists. Next, we performed further DFT calculations which consider both contributions of these energy costs simultaneously, and one layer is represented by finite AGNRs, in order to reduce computational cost.

The application of critical strain to one of the two layers of BLG could be used to tune the stacking profile of the system. In particular, below the critical strain, it is energetically favorable to transfer the strain to the second layer in order to maintain a uniform AB stacking configuration. On the other hand, above the critical value, the cost of maintaining the strain in the second layer is too high and the system prefers to release it and adopts a non-uniform stacking profile. Thus, for values of strain bigger than $\sim 1\%$ strain the stacking of BLG changes, and this consequently affects different properties, like electronic structure and transmission, that are directly related to the relative stacking. In the next Chapters 4 and 5, we explain the effect of heterostrain on the electronic and transport properties.

Chapter 4 1D topological channels in graphene

4.1 Introduction

The application of heterostrain on BLG leads to the creation of Moiré superlattices (Figures 1.11 (a)–(c)). In some cases, interface channels are created (AA- and SP-stacked domains), which exist between the AB/BA-stacked domains. These interface channels may have similar properties compared to the ones that tBLG has. Concerning the electronic properties of interface channels in tBLG, with the application of large enough interlayer bias (Δ>200 meV) there is a localization of electronic states in AA- and SP-stacked domains (topological channels). Theoretical studies have shown that electrons propagate without dissipation along these interface channels (AA- and SP-stacked interfaces) in minimally-twisted tBLG, using continuum model calculations [53, 54, 89, 92, 99, 100], verified by STM measurements [101]. For twist angle $\theta \sim 1.1^\circ$ interesting phenomena arise, like correlated insulating states and unconventional superconductivity, as experimental studies showed [94]. Due to the similar Moiré domains created in hBLG (Figures 1.11 (a)–(c)), we expect relative phenomena.

DFT calculations have predicted that heterostrain can be used to open and tune an electronic energy gap in BLG [139]. For these DFT studies the LDA functional was used, while for our calculations for the study of the effects of stacking on the energetics of BLG (Chapter 3) we used the GGA functional. Choi et al. showed how the direct band gap (red color) and the indirect band gap (blue color) change with the application of uniaxial

strain along the ZZ direction for BLG (Figure 4.1). For small strains (ε<2%) and for larger strains (ε>10%) the band gap is direct, while for the intermediate strains between AA and AB stackings, the band gap is indirect. A direct band gap means that the minimum energy of the conduction band and maximum energy of the valence band of the electrons occur at the same wavevector in the BZ, while for the indirect band gap, they occur for different wavevectors in reciprocal space. In the case of the direct band gap, the electrons can directly transition from the valence band to the conduction band with minimal change in momentum. A direct band gap is more desirable in electronic applications, as electrons can be emitted and absorbed more easily.

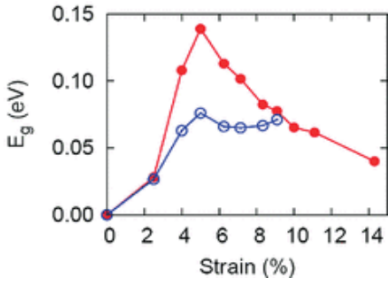

Figure 4.1: *Band gap of hBLG as a function of the uniaxial strain applied on the L1. The blue curve corresponds to the indirect band gap and the red curve corresponds to the direct band gap. Figure adapted from [139].*

Also, Crosse et al. performed theoretical calculations (nearest-neighbor TB method) and showed how the energy band gap depends on both the application of interlayer bias and uniaxial heterostrain for an initially AB-stacked BLG ribbon [146]. This system is 1D, so it is periodic only along one of the two perpendicular in-plane directions. The BLG ribbon is wide enough, which means that its size is sufficient so that the confinement effects are negligible, which means that the band structure of the graphene ribbon resembles this of bulk graphene. Its upper layer is subjected to uniaxial compressive strain along the AC direction and its lower layer is subjected to a uniaxial tensile strain along the same direction. In the absence of interlayer bias and the application of low strain (ε=2%), the BLG ribbon still is band gap semimetal (region (A) in Figure 4.2). Thus, only with the application of layer-asymmetric strain, there is no band gap opening for the BLG ribbon. However, with the application of a large enough interlayer bias (Δ ~300 meV), there is the formation of a band gap of size of 400 meV (region (B) in Figure 4.2). Also, for the application of

both uniaxial strain (ε ∼6%) and interlayer bias (Δ ∼300 meV), Crosse et al. found the creation of a negative band gap, which means that the bands cross the Fermi Level and the material is a metal, as shown in Figure 4.3 (region (C) in Figure 4.2). Therefore, the application of only interlayer bias or both layer-asymmetric strain and interlayer bias is an alternative way to tune the electronic properties of BLG systems and only the application of heterostrain without interlayer bias is not sufficient to tune the electronic properties of BLG ribbon.

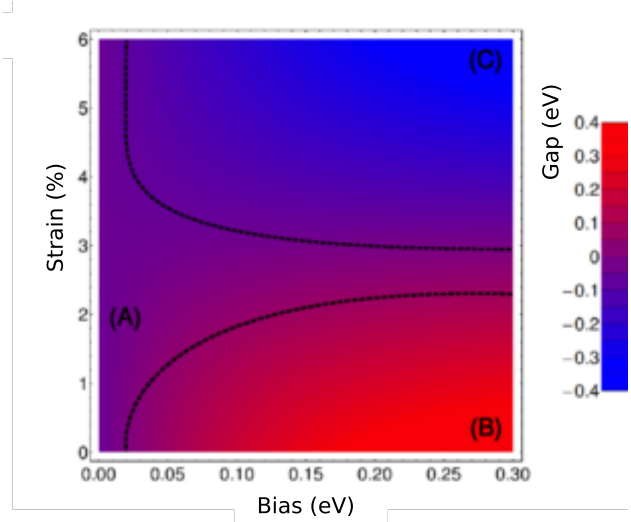

Figure 4.2: *Dependence of energy gap on both the interlayer bias and the uniaxial heterostrain for BLG ribbon, which is initially AB-stacked. Region (A) corresponds to the case that only layer-asymmetric strain is applied to the ribbon without bias, region (B) to the case that only interlayer bias is applied and region (C) to the case that both large layer-asymmetric strain ε ∼6% and large interlayer bias (Δ ∼300 meV) are applied to the BLG ribbon. Figure adapted from [146].*

There is no study so far that explains the local electronic properties of the interface channels in this heterostrained system. Continuum model calculations showed the formation of valley-protected topological channels in a similar system: BLG which has a domain wall-grain boundary between AB and BA stackings (Figure 4.4) [53]. Figure 4.5 shows the band structure around the Fermi level E_{F} near the K-point (top panel) and K'-point (bottom panel) with the application of uniform interlayer bias (Δ=50 meV) in the system with a grain boundary. The bands for both panels are linear near Fermi level E_{F}. This pair of bands for the application of uniform interlayer bias has states that belong to the domain wall, as the AB- and BA-stacked domains are gapped. We expect to have the formation of

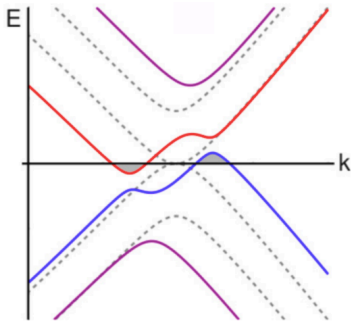

Figure 4.3: *Band structure of BLG without bias (dashed lines) and with bias (solid lined) in the presence of a layer-asymmetric strain. In the case of applied bias there is a 'negative' band gap. Figure adapted from [146].*

similar topological channels in 1%-AC-strained hBLG under the application of interlayer bias.

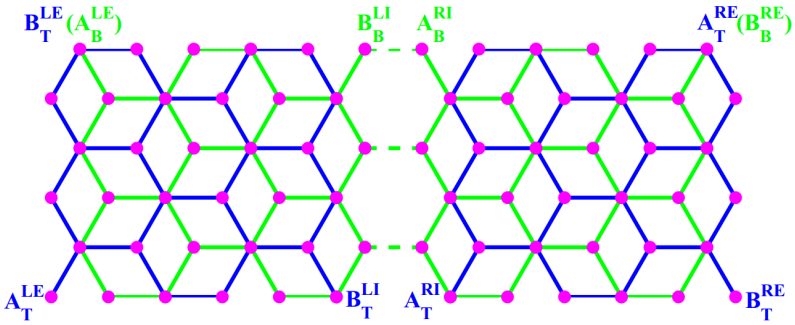

Figure 4.4: *Interface channel induced by a grain boundary in AB-stacked BLG. Figure adapted from [53].*

Moiré systems have been found experimentally to exhibit relaxation due to the many different stacking arrangements that they have, such as tBLG systems [81]. This relaxation, which leads to local strain and deformations has been found to affect the properties of these systems. For example, in Magic-Angle tBLG experimental studies showed the formation of flat bands close to Fermi level E_F [94, 95]. The flat bands lead to enhanced DOS and correlated insulating states at half-filling. These flat bands also can lead to superconductivity, like in this case, which means that below a certain temperature, the material conducts electricity without resistance. Zero-resistance states were observed for Magic-Angle tBLG with critical temperature T_c=1.7 K.

Relaxation could also affect the electronic properties of hBLG, as it is a Moiré system.

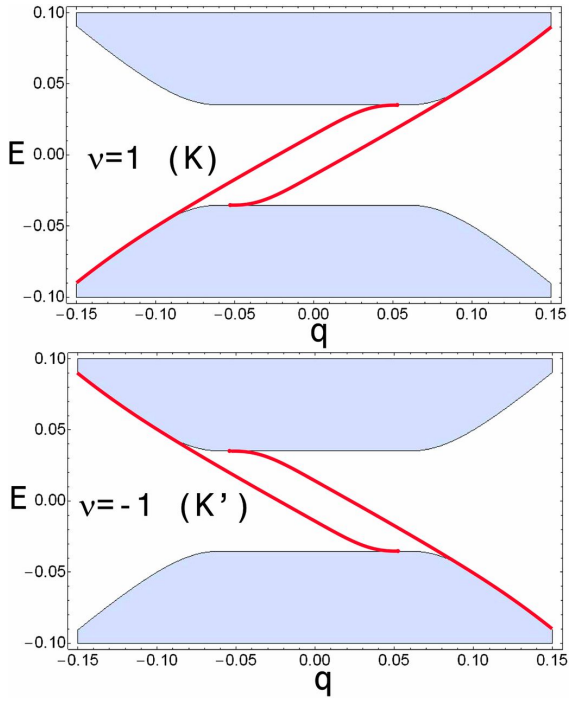

Figure 4.5: *Band structure near Fermi level E_F of BLG with a grain boundary along K valley (top panel) and K' valley (bottom panel) with the application of Δ=50 meV uniform interlayer bias. The BLG is initially AB-stacked and results in the BA stacking with a grain boundary between the two stackings. With the application of uniform interlayer bias the AB- and BA-stacked domains are gapped, while the domain boundary has localized states, resulting in a robust topological channel. Figure adapted from [53].*

Molecular Dynamics and DFT calculations showed the creation of flat bands for hBLG near Fermi level E_{F}, with the use of out-of-plane relaxation, for $\varepsilon\pm1\%$ strain [96]. In this study, they used a combination of Molecular Dynamics (to get the structure) and DFT (to get the electronic structure). Because of the use of DFT with periodic boundary conditions, they were restricted to certain cell sizes and certain strains. These calculations included both compressive and tensile strain from -5% to +5%, allowing out-of-plane relaxation. They showed the formation of flat bands near Fermi level E_{F} only for $\varepsilon\pm1\%$ heterostrain. They were primarily interested in the effect of the Moiré pattern on chemical functionalization. They found flat bands but did not investigate thoroughly and did not consider the effect of a gate voltage. To do that on an experimentally relevant system size, you have to use TB, which we do. Thus, it is important to include the effect of in-plane and out-of-plane relaxation for the study of electronic properties of hBLG. For our calculations, out-of-plane relaxation has been ignored for simplicity.

This Chapter includes the study of local electronic properties of hBLG for 1% applied uniaxial heterostrain on the L1. In the absence of a Poisson contraction ν perpendicular to the applied strain, this creates a regular 1D Moiré pattern. An example of the system that we investigated is shown in the main panel of Figure 4.6. An exaggerated 4% uniaxial strain is applied on the L1 along the AC direction (orange-bottom) and the L2 layer (blue-top) remains unstrained. The resulting lattice mismatch along the y-direction gives rise to an alternating sequence of (from bottom to top on Figure 4.6) AA (Figures 4.6 (c) & (e)), AB (Figure 4.6 (a)), SP (Figure 4.6 (d)) and BA (Figure 4.6 (b)) stackings. This situation can arise, for example, if the strain applied to a bilayer system using a flexible substrate does not transfer between the layer directly in contact with the substrate to the L2 layer. In Chapter 3, we proved that this can happen if the energetic penalty caused by the broken AB stacking is less than the energy cost required to strain the L2 layer by the same amount. For applied heterostrain of approximately 1% or greater, we found that the modulated stacking is energetically favorable, which indicates that such strains can be used as a tool to tune the stacking of a BLG system.

Here, we focus on the formation and evolution of interface states in hBLG under the application of interlayer bias using the TB method. We want to find out if the application

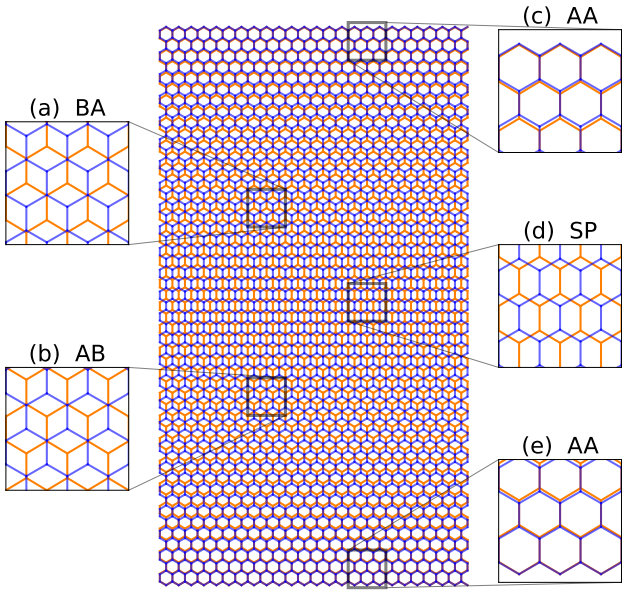

Figure 4.6: *hBLG with 4% uniform heterostrain, applied along the AC direction to L1 layer (orange). A 1D Moiré pattern is formed, which consists of (c) & (e) AA stacking, (a) BA stacking, (d) SP stacking, and (b) AB stacking.*

of a uniform heterostrain and interlayer bias are sufficient for the creation of topological channels in BLG. Section 4.2 contains the computational details of our TB calculations, to determine the electronic properties of hBLG and a simple model to account for these in-plane relaxations. In Section 4.3 we examine the band structure and the distributions of states in hBLG, and compare the results to what is found for uniformly-stacked AA, AB/BA, and SP systems. The application of realistic values of interlayer bias and heterostrain do not give clear signatures of the expected topological channels, as the relevant band structures and the distribution of states demonstrated. In Section 4.4 we used a simple model to mimic the effect of in-plane relaxation, which is motivated by previous studies in twisted systems. In tBLG relaxation tends to minimize AA-stacked domains, maximize AB/BA-stacked domains, and sharpen SP-stacked interfaces, as already mentioned in Section 1.2.5. These structural deformations affect the electronic band structure and, in particular, the formation of flat bands at specific twist angles in tBLG.

In this heterostrained system, one layer is assumed to remain uniform due to its interaction with a substrate. If strain is applied using a flexible substrate, the in-plane relaxation should occur in the unstrained layer, as shown by Raman spectroscopic measurements for

MLG [56, 58, 60] and for BLG [61] respectively. However, if the strain is applied to the L2 layer using, for example, the tip of an atomic force microscope [105], then we expect in-plane relaxation within this layer. Therefore, we consider in-plane relaxations of both the strained and unstrained layers independently in order to capture the geometries that emerge from both processes. We find that in-plane relaxation, of either the strained or unstrained layer, allows for more robust topological interfaces to emerge due to larger, gapped AB/BA-stacked domains and sharper AA- and SP-stacked interfaces. After the discussion of structural, energetic, and band structure considerations, we examine the resulting topological interfaces in more detail in Section 4.5. The layer and sublattice distribution of states at the AA- and SP-stacked domains are investigated, and it was found that it depends on the type of interface. Last, we discuss our findings and the potential role of heterostrain as a mechanism to tune the presence and distribution of topological channels in BLG systems.

4.2 Computational details

The electronic structure of hBLG which has a range of different stackings and interlayer biases is investigated using a TB model (Equation (2.37)). The nearest-neighbor in-plane transfer integral for graphene which is used for these TB calculations is $V^0_{\mathrm{pp}\pi}$=-2.7 eV according to Reference [126], and the nearest-neighbor out-of-plane transfer integral $V^0_{\mathrm{pp}\sigma}$=0.48 eV and the unstrained interlayer distance d = 3.35Åfor BLG according to Reference [92], which have been mentioned in Section 2.3. We considered interactions beyond nearest neighbors with a cutoff distance for the xy-plane of **d**=1.82 Å, to account for the nearest-neighbor hopping terms with the application of heterostrain, as well as for the interlayer interactions. The main geometry considered in this work is a BLG sheet with 1% applied uniaxial heterostrain along the AC direction in L1, with the other layer L2, being unstrained. As the stacking modulation does not affect periodicity along the ZZ direction (Figure 4.6), the periodic unit cell required for calculations of this system consists of a single chain of atoms from each layer. We assume an initial AA stacking at y=0 and the stacking returns to AA at the top of the unit cell in order to maintain periodicity. This

requires a total extension which is a multiple of y_u=$3a_0$, the width of a four-atom graphene unit cell. We assume that the L1 layer contains N strained cells and ε is the relevant uniaxial applied strain. The unit cell for the 1% applied heterostrain case corresponds to N=100 strained cells in L1 and N=101 cells in L2 and contains in total 804 carbon atoms. The band structures presented in the following sections are calculated using exact diagonalization of the corresponding Hamiltonian matrices with the appropriate Bloch phases. We are interested in the emergence of states confined to x-direction interfaces, so we only show bands as a function of k_x, with k_y=0.

In-plane relaxation has been shown to play a vital role in determining the electronic properties of twisted Moiré systems [84, 86, 87, 89, 92, 93]. The main effect of such relaxation is an increase of the AB- and BA-stacked domains at the expense of AA- and SP-stacked regions. In the presence of an interlayer bias, this affects the localization of states along the sharper AA- and SP-stacked interfaces between the gapped AB- and BA-stacked regions. To consider how in-plane relaxations affect the geometry of hBLG, we employ a simple model that allows the relevant stackings of hBLG to be continuously tuned. In our model, we assume that only one layer of the system is allowed to relax. As mentioned in Section 4.1, the layer that is actually strained in the experiment will depend on the method used to apply the strain. In experimental conditions, this corresponds to the layer which is not in contact with the substrate, but only with the other graphene layer. We first consider the case where relaxation occurs within the strained layer (L1). A uniform strain $\varepsilon = \frac{1}{N}$ applied to the L1 layer along the AC direction introduces an extension that is linearly dependent on the unstrained y-coordinate $y_{0,L1}$ and is given by:

$$\Delta y_{L1}\left(y_{0,L1}\right) = \varepsilon\, y_{0,L1}\,. \tag{4.1}$$

The linear extension and uniform strain as a function of position, are shown by the grey curves in Figures 4.7 (a) and (b) respectively. The lattice mismatch with L2 layer conserves the high symmetry AA, AB, SP, and BA stackings when Δy_{L1}=0, a_0, $\frac{3}{2}a_0$ and $2a_0$ respectively, which correspond to $y_{0,L1}^{AA_1}$=0, $y_{0,L1}^{AB} = \frac{Ny_u}{3}$, $y_{0,L1}^{SP} = \frac{Ny_u}{2}$ and $y_{0,L1}^{BA} = \frac{2Ny_u}{3}$. The stacking returns to AA again at Δy_{L1}=y_u=$3a_0$ and $y_{0,L1}^{AA_2}$=Ny_u. Due to periodicity, AA_1 and AA_2 correspond to the same point, but it is useful to consider them separately in

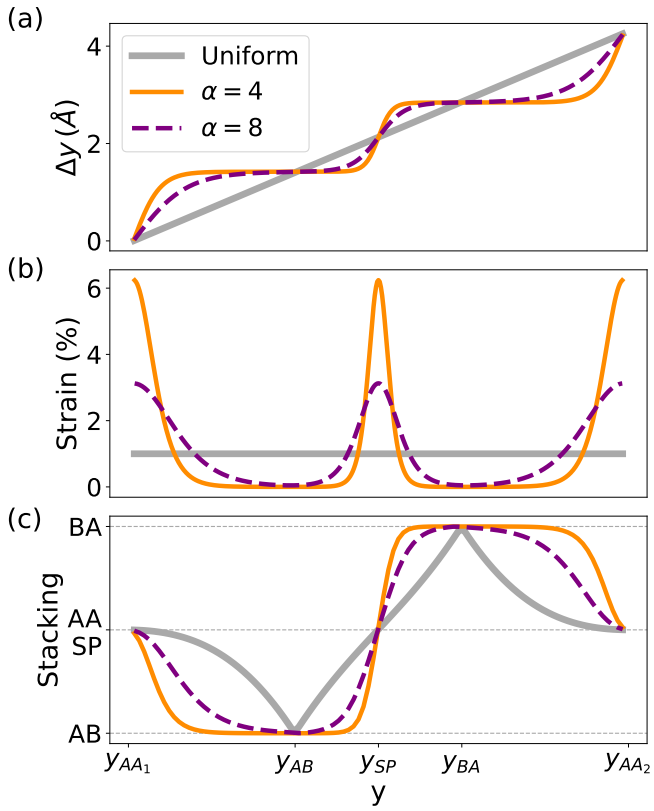

Figure 4.7: *(a) Local displacement, (b) strain, and (c) stacking order for 1% uniaxially strained hBLG as a function of position along the AC strained direction (y). The grey curve shows the case of a uniform uniaxial strain in layer L1, while the purple and orange curves correspond to 'relaxed' structures for interface smoothness parameter* $\alpha = 8$ *and* α*=4.*

the context of a finite unit cell. The positions of these high symmetry stacking locations are shown along the x-axis in Figure 4.7 (c) and the local stacking near them by the Figures 4.6 (a)–(e).

To include the effect of relaxation and have sharper interfaces and wider gapped domains, we replace the linear extension from Equation (4.1) with a summation of sigmoid functions, $\Delta y_{L1}^{\text{rel.}}(y_{0,L1}) = \sum_i S_i - \frac{S_{AA_1}}{2}$, which have the following form:

$$S_i(y_{0,L1}) = \frac{\Delta Y_i}{1 + e^{-(y_{0,L1} - y^i_{0,L1})/(\alpha \Delta Y_i)}}\,, \tag{4.2}$$

with $i \in \{AA_1, SP, AA_2\}$. These sigmoid functions are centered at the AA- and SP-stacked interfaces (orange and purple curves in Figure 4.7 (a)), where they locally increase the strain (Figure 4.7 (b)) and sharpen the interfaces (Figure 4.7 (c)). The inclusion of the

effect of relaxation leads to much lower strains and more uniform stackings in the AB- and BA-stacked regions. The 'sharpness' of an interface is determined by the parameter α, which adjusts the local maximum value of strain at the interface and relates the characteristic width of an interface to the total stacking shift (ΔY_i) that occurs across it. Low values of α correspond to sharp interfaces and bigger values of α to wider interfaces. However, the model assumes that the effects of each interface are independent and break down if α is increased to values where the interface regions begin to merge.

This approach can also be used to consider relaxation which occurs instead in the initially unstrained L2 layer, as is expected to occur if heterostrain is applied to the other layer via a flexible substrate. In this case, a uniform tensile strain is first applied to L2 to match that in the strained layer, before a non-uniform compressive strain is applied using the 'sum-of-sigmoids' approximation above to return the average strain in the unstrained layer to zero. The structural and electronic effects of both types of relaxation are discussed in detail in Section 4.4.

4.3 Electronic properties of heterostrained systems

We consider the electronic structure of BLG with a 1% strain applied to one of the layers, in the absence of interlayer bias and relaxation effects. The 804-atom unit cell of this system is four times wider than the structure depicted in Figure 4.6. The electronic structure of this system along the k_x direction is shown in Figure 4.8 (a). It has a complex series of subbands due to the large real-space unit cell with 804 atoms. The parabolic bands that are expected for AB/BA-stacked BLG cannot be clearly distinguished here (Figure 1.5 (b)). There is a large number of bands that cross the Fermi energy E_{F} near E=0 and give the system a metallic character. This suggests that the band structure from our heterostrained system has features from the band structures of uniformly AA- (Figure 1.5 (a)) and SP-stacked (Figure 1.5 (c)) BLGs. Unlike AB stacking, these cases resemble the conical band structure of MLG, but with two copies of the linear MLG cone separated in either energy (AA), or energy and momentum (SP).

We now explore the relationship between the band structure of hBLG and those of

regularly-stacked systems in more detail. Figures 4.8 (b)–(d) show the bands from Figure 4.8 (a) projected onto narrow 20 Å strips centered around y^{AB}, y^{AA}, and y^{SP} respectively, where the color of each point corresponds to the weight of the associated states of hBLG in these regions. Figures 4.8 (b)–(d) show the effective band structures in the AB-, AA-, and SP-stacked regions of hBLG. Bands that are only strongly colored in one region indicate states that are largely localized in that region. Similarly, a strong correspondence between the bands in each region and their bulk counterparts in Figures 1.5 (a)–(c) would indicate that bands in a region with a particular stacking resemble those in a uniform bilayer with the same stacking. However, the majority of these states, are not localized in this manner. Instead, they have weight in multiple regions, indicating states that are distributed across large parts of the system and not confined to regions with a particular stacking. These states reside in regions of k_x–E space common to all three stackings, and can be viewed as hybridizations between states with similar momentum and energy that occur in regions with different stackings. Although they have a similar spatial distribution to that expected for topological interface states, we note that there is no band gap in this system.

Interlayer bias opens a band gap only in BLG systems with certain stackings, with the largest gap occurring for AB stacking and no gap opens for AA- and SP-stacked systems (Figures 1.5 (d)–(f)). The application of interlayer bias can lead to a complex distribution of gapped and conducting domains, and the formation of topological interface states, in systems with modulated stacking, such as tBLG [54]. We anticipate that similar behaviour could emerge in the heterostrained system considered here, and in particular that the AA- and SP-stacked domains that separate the AB/BA-stacked regions should host 1D topologically protected channels. Figure 4.9 (a) shows the band structure of the heterostrained system when Δ=-200 meV interlayer bias is applied and Figures 4.9 (b)–(d) show the band structure and projections of the corresponding states onto each atom in a 20 Å strip around AB-, AA- and SP-stacked domains respectively. We note that here the negative potential is applied to the unstrained layer L2. For an opposite sign of interlayer bias, a slightly different result is obtained, due to the inequivalence of the layers and the broken electron-hole symmetry. We note that, unlike other 1D interface cases such as grain boundaries or sharp bias flips [97, 98, 147–150], the application of an interlayer bias does not seem to give rise

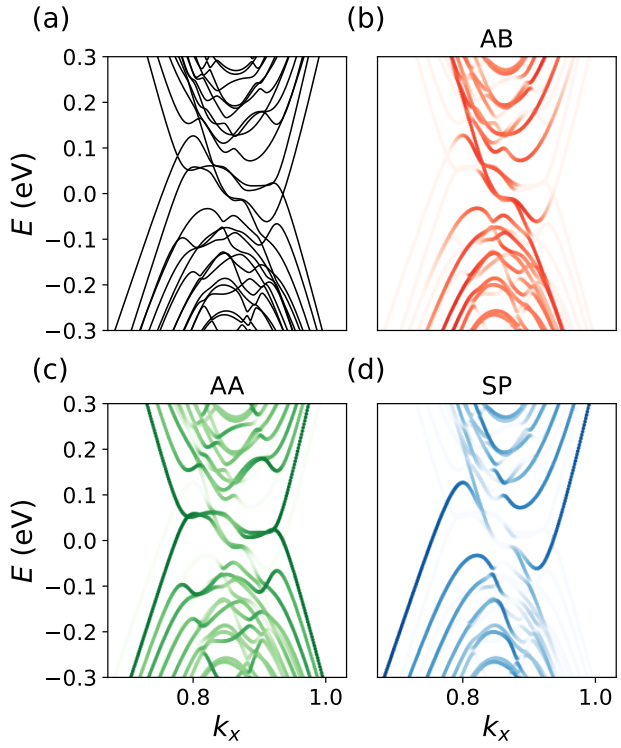

Figure 4.8: *(a) K-valley band structure of a BLG system with 1% uniform heterostrain. Figures (b), (c), and (d) show the band structure projected onto 20 Å wide strips around the perfect AB-, AA-, and SP-stacked regions respectively. Most of the states are distributed across multiple stacked domains, with exceptions for low energies which show confinement to regions with particular stackings.*

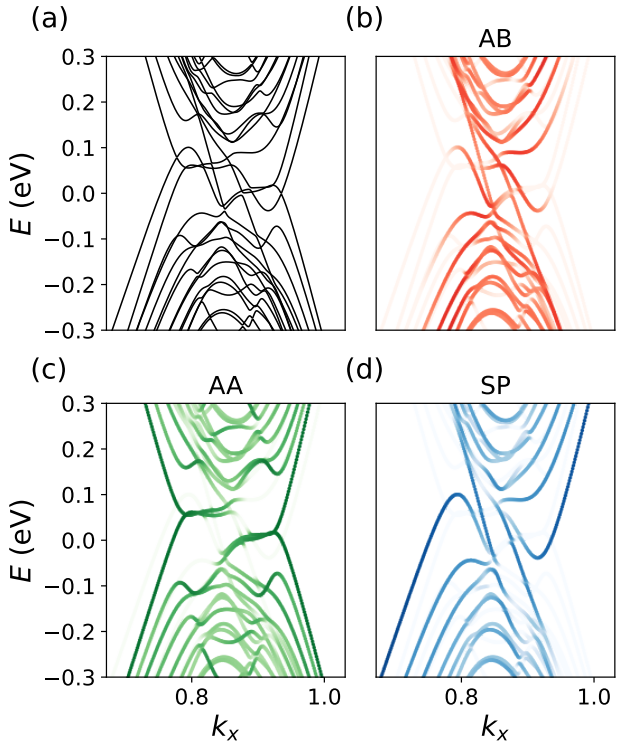

Figure 4.9: *(a) Band structure of a hBLG with 1% uniform heterostrain and an additional interlayer bias Δ=-200 meV along k_x direction. Figures (b), (c), and (d) show the band structure projected onto 20 Å wide strips around the perfect AB, AA, and SP stacking points, respectively, where the color of each point corresponds to the weight of the associated state of hBLG in these regions. No clear band gap opens, even for states in the AB-stacked region, despite a sizeable band gap opening for the corresponding uniformly AB-stacked system in Figure 1.5 (e) for the same bias.*

to clearly defined topological channels (Figure 4.9 (a)). In these other systems, an interlayer potential opens a bulk band gap which is bridged only by pairs of chiral boundary modes with opposite propagation directions in the K and K' valleys (Figure 4.5) [53]. For our system, this would correspond to a total of four valley-protected topological modes in each valley, two each for the interfaces along the AA- and SP-stacked domains. Instead of the clear emergence of a bulk gap and topological modes, we see only minor changes compared to the unbiased system discussed in Figures 4.8 (a)–(d). Consequently, uniform heterostrain and interlayer bias alone are not sufficient to create 1D topological channels. An accompanying relaxation that sharpens the interfaces and expands the Bernal-stacked regions may be required.

4.4 Role of interface smoothness

The absence of a band gap formation in Section 4.3 can be explained by the stacking of the heterostrained system. It has only very small regions with perfect AB or BA stackings, which suppresses the formation of a band gap. However, including the effect of relaxation might lead to the creation of topological channels. We consider the simple relaxation model, explained in Section 4.2, in order to determine how in-plane relaxation affects the electronic properties of a biased hBLG system. It allows us to continuously adjust the interface smoothness and redistribute the local strain (Figure 4.7 (b)). The panels in Figure 4.10 (a) show the evolution of the band structure of the biased hBLG system, as the interface smoothness α is decreased. They include the band structure for the application of a uniform heterostrain and for interface smoothness parameters α=15, α=11, α=7, and α=3. As the interfaces become sharper (smaller interface smoothness parameter α), the number of bands crossing the Fermi energy E_{F} decreases until only two pairs of crossings remain. We note that this is the expected number of band crossings for a BLG system with two topological interfaces between AB and BA-type regions, i.e. with the formation of valley-polarised interface states along both the AA- and SP-stacked domains in our system. The energy window in which only these four bands are present (the so-called 'pseudogap'), is shown by the red shaded areas in the panels of Figure 4.10 (a), and increases as the interfaces become sharper. The pseudogap opens at the critical value of α=11 and is not present for unrelaxed or smoother interfaces. The evolution of the pseudogap for Δ=-200 meV is shown by the orange curve in Figure 4.10 (b), together with the pseudogap for smaller bias (Δ=-100 meV) and bigger bias (Δ=-400 meV).

The critical smoothness α required to open a pseudogap and observe interface states varies with the magnitude of the bias (Figure 4.10 (b)). Lower biases require a sharper interface to open a pseudogap. This is consistent with the different stacking profiles in these systems, as sharper interfaces give rise to larger regions with nearly perfect AB- and BA-stacked domains. In order to observe a pseudogap and consequently have topological channels, relaxation has to be sharp enough. For example, for low bias, such as Δ=-100 meV, the interface smoothness parameter α has to be at least below 9 to induce a pseudo-

gap. If it is smoother, it does not lead to topological channels for this value of interlayer bias. From Figure 4.10 (b) it is shown that pseudogap depends on both the applied bias and the interface smoothness parameter α. Thus, pseudogap can be presented as the bias needed for different types of interfaces. Consequently, even if the AB/BA-stacked domains become gapped with the application of large interlayer bias, this is not enough to observe the pseudogap. With the inclusion of the effect of relaxation these gapped domains become bigger which leads to sharper interfaces and then pseudogap is evident.

In the experiment, strain solitons with widths of 6 to 11 nm were reported on samples grown by CVD method [104], whereas a recent work on a biaxially strained bilayer system reports domain wall solitons with widths of between 15 and 35 nm depending on energy [151]. In our model, we can approximate the structural width of a soliton by $\sim 8\alpha\Delta Y$, which corresponds to the width over which 96% of the stacking shift between perfect AB and BA registries occurs. The interface regions in our work have a width of $\sim$4.5 nm for SP-stacking and $\sim$9.1 nm for AA-stacking for α = 4, with these values doubling for the α = 8 cases. These are similar to widths of 5.2 nm and 12 nm reported by continuum model simulations of similar interfaces [71, 152]. The electronic width of the soliton, determined from the localization of interface states may vary from the structural width, as shown later in Figure 4.12.

The degree to which intralayer relaxation will occur can be simulated in a number of ways, including molecular dynamics [89, 129, 153, 154] or *ab initio* simulations [91], and the Frenkel Kontorova model and related continuum approaches [71, 84, 85, 92]. The specifics of the relaxation are also likely to be affected by experimental conditions, such as the effects due to substrate interactions. However, relaxation occurs principally to minimize the energy costs which are introduced by straining the graphene lattice and breaking the uniform AB stacking registry. Both energy cost contributions can be calculated by *ab initio* simulations of uniform systems [155], allowing the energetics of larger, non-uniform systems to be estimated by summing over local stacking and strain costs throughout the system. We consider two possible relaxation scenarios, which either the strained layer relaxes using the simple model in Section 4.2 (Figure 4.11 (a)) or the unstrained layer (Figure 4.11 (b)). The energy costs associated with the stacking [48] and strain were cal-

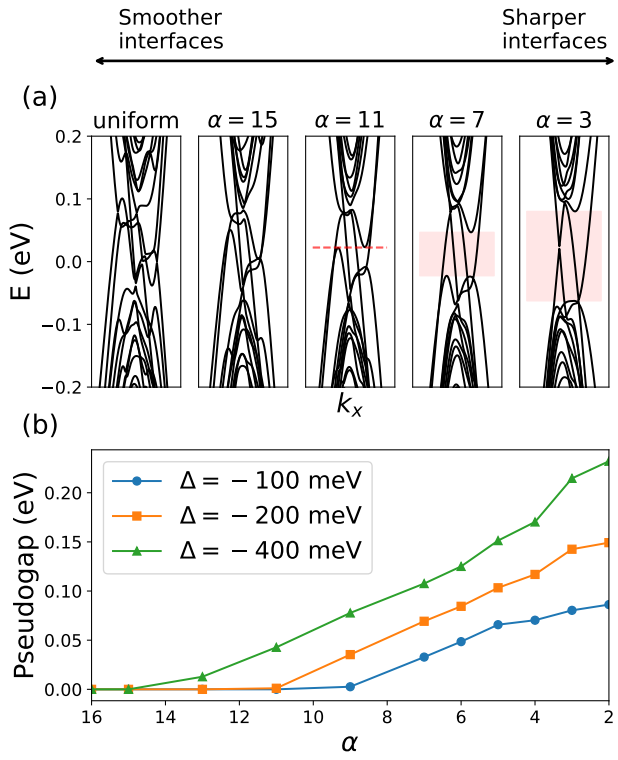

Figure 4.10: *(a) Evolution of the band structure for hBLG for Δ=-200 meV applied interlayer bias on the hBLG system for uniform heterostrain, α = 15, α=11, α=7 and α=3. The AA- and SP-stacked interfaces are sharpened by relaxing the strained layer (L1). The 'pseudogap' window, where only four band crossings are present near Fermi level E_F is shown in red. (b) Pseudogap for different values of interlayer bias (Δ=-100 meV, Δ=-200 meV, and Δ=-400 meV) and interface smoothness parameter (α varies from 16 to 2).*

culated with DFT method for perfect BLG systems and are quite accurate. Experimental studies showed similar energy cost for the stacking (∼2 eV/supercell) [104]. The strain energy depends on the width of the relevant interface channels. In each case, the atomic positions in the other layer remain the same after the application of heterostrain.

Figures 4.11 (a) and (b) show the total energy costs per supercell of breaking uniform AB stacking (red curves) and local strains (blue curves) for the relaxed hBLG and the unrelaxed. The total energy cost is shown by the black curve, with the corresponding energy values for a uniformly heterostrained system shown by the square symbols. The energy costs due to the change of stacking are identical for the two scenarios, with the energy costs decreasing linearly for sharper interfaces (lower interface smoothness parameter α). In contrast, the energy cost due to strain is higher for the case of relaxing the initially un-

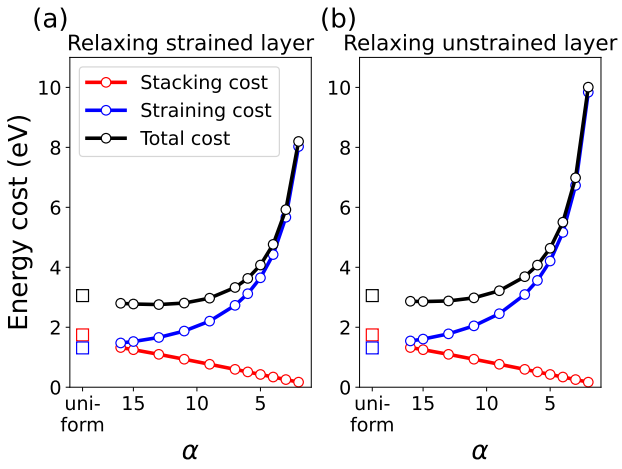

Figure 4.11: *Energy costs per supercell associated with breaking AB stacking registry (red curves) and strain (blue curves) in hBLG. The effect of the simple relaxation model applied to either the (a) strained or (b) unstrained layer is shown to give sharper interfaces. The black curves show the total energy from both terms, and the square symbols show the corresponding values for uniformly strained unrelaxed systems.*

strained layer L2. In this case, large portions of both layers have strain values near 1% as the AB/BA-stacked regions grow for smaller values of α. For both relaxation scenarios, and for all values of α, the strain energy cost is greater than that of the uniformly-strained system (blue squares). This is trivial for relaxing the unstrained layer, as the cost of the additional strain introduced by the relaxation of this layer must be added to the cost of the uniformly strained layer. When the strained layer is relaxed, the strain is redistributed throughout the layer such that the average strain in the layer is conserved. As the energy cost of strain increases superlinearly, the additional energy cost of higher strain near the interfaces is not compensated by the reduced strain in the AB- and BA-stacked domains. Also, there is a slight reduction in the total energy, compared to the uniformly strained case (black square symbol), if the interface smoothness parameter is $\alpha \gtrsim 8$ when L1 is allowed to relax and $\alpha \gtrsim 10$ when L2 is allowed to relax. Consequently, whether the L1 layer or the L2 layer is allowed the relax, this does not affect significantly the total energy cost. For this reason, we decided to include the effect of relaxation for the L1 heterostrained layer. For applied interlayer bias Δ=-400 meV and for interface smoothness parameter α=9, we have $\sim$100 meV pseudogaps (Figure 4.10 (b)), which is reasonable. Also, for this value of interface smoothness parameter α=9, which has been introduced for the inclusion of relaxation,

the total energy cost is not high ($\sim$3 eV per supercell). A similar pseudogap (100 meV) could be achieved for a lower value of bias, such as for Δ=-200 meV (Figure 4.10 (b)), but with a much higher energetic cost due to the larger local strain at the interfaces (Figure 4.11 (a)). Conversely, a similar pseudogap with a smoother interface (larger values for α), would require a larger bias to be applied between the layers. Consequently, for applied interlayer bias Δ=-400 meV and interface smoothness parameter α=9 we investigated the local electronic properties of hBLG in the next Section.

4.5 Interface states

Figure 4.12 (a) depicts the band structure of hBLG near K point along k_x for Δ=-400 meV and α=9. It has a pseudogap of $\sim$100 meV, spanned by two pairs of dispersive bands. To verify that these correspond to the interface-localized channels we plotted the band structure and the distribution of states projected onto each atom in a 20 Å strip around AB-, AA- and SP-stacked regions (Figures 4.12 (b), (c) and (d) respectively). Figure 4.12 (b) proves the AB-stacked regions are indeed gapped, whereas the AA- and SP-stacked interfaces host a pair of boundary modes each in the K-valley. From the slope of the bands near Fermi level E_{F}, we observe that the modes at a particular interface (AA or SP) propagate in the same direction. Also, the K-valley modes from the two different interfaces propagate in opposite directions. This is due to the opposite displacements of the AB- and BA-stacked domains relative to the two interfaces. All these features are consistent with the formation of valley-protected topological modes at the interfaces due to a change in the valley Chern number between AB and BA regions in biased BLG, as continuum model calculations showed for simple domain wall for BLG [53].

There are subtle differences between modes at AA- or SP-stacked interfaces. The AA-stacked interface in our system is broader than the SP-stacked interface because the AA-stacked interface has twice the interlayer shift of the SP-stacked interface ($\Delta Y_{\mathrm{AA}} = 2a_0, \Delta Y_{\mathrm{SP}} = a_0$. This does not seem to correspond to a wider interface state, however. Figures 4.12 (e)–(h) show the projections of the corresponding states in Figures 4.12 (c) and (d) respectively onto each atom in a 20 Å strip around the relevant interface. A slightly

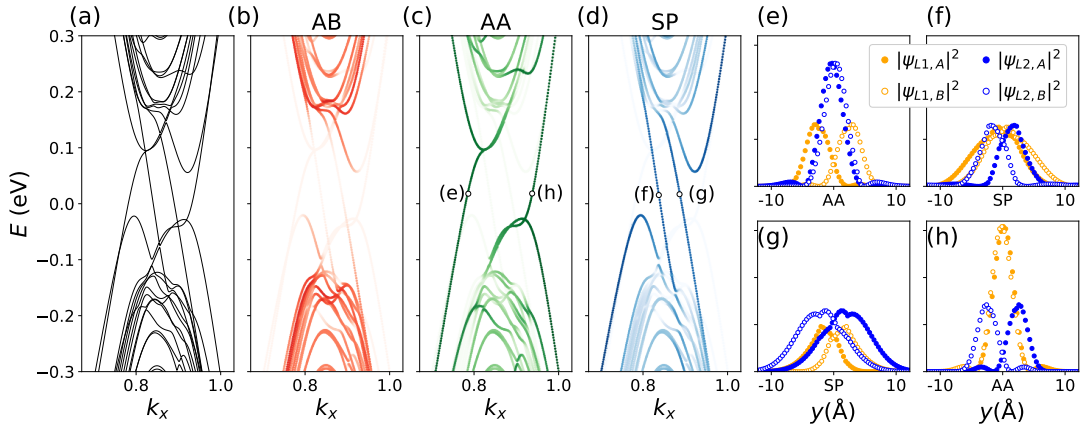

Figure 4.12: *(a) Band structure of hBLG under the application of Δ=-400 meV interlayer bias, where the interfaces are sharpened by a relaxation with α=9 in the strained layer. Figures (b), (c), and (d) show the band structure projected onto 25 Å wide strips around the perfect AB, AA, and SP stacking points, respectively. Clear topological channels are formed at the AA- and SP-stacked interfaces in Figures (c) and (d) respectively. The distributions of these states around these interfaces (AA- and SP-stacked domains) on each layer (L1 and L2) and each sublattice (A and B) are shown in Figures (e)–(h).*

broader spread is noted for the SP-stacked interface modes in Figures 4.12 (f) and (g) compared to the AA-stacked interface modes in Figures 4.12 (e) and (h). There is a more significant difference however in the layer distribution of these AA-stacked modes. Each of the two AA modes in Figures 4.12 (e) and (h) has the largest weight exactly at the interface on one of the two layers, with both sublattices having very similar distributions in the dominant layer. The other layer has a smaller, sublattice-split distribution with peaks on either side of the interface. In contrast, the SP modes in Figures 4.12 (f) and (g) appear to have a more symmetric distribution between both layers and sublattices. However, this distribution of states might be sensitive to the strain levels at the interfaces, and may not be present if, for example, relaxation results in different local strains at each interface.

4.6 Summary of Chapter

In this Chapter we showed that the application of interlayer bias and local deformations which arise due to the application of heterostrain on BLG give rise to robust 1D topologically protected interface channels between the AB- and BA-stacked domains. The application of interlayer bias leads to gapped (AB/BA-stacked regions) and localized states

(AA- and SP-stacked regions). The latter states are evident in the pseudogap which opens in the AB/BA-stacked regions with the application of interlayer bias. The size of the pseudogap and the emergence of interface states depend on how sharp the interface is modified by relaxation, as well as the magnitude of applied bias. When the AB-stacked regions are gapped, the AA- and SP-stacked interfaces each host a pair of boundary modes in the K valley propagating unidirectionally. The corresponding modes in the K′ valley propagate in the opposite direction, which is consistent with the formation of valley-protected topological modes at the interfaces due to a change in the valley Chern number between AB- and BA-stacked regions in biased BLG. Last, unlike tBLG where only the SP-stacked interfaces contribute to the network, the Moiré system generated by the application of a uniaxial strain has two distinct interface states, namely those at the AA- and SP-stacked interfaces. These interface states at the AA- and SP-stacked interfaces are not identical, with differences in the layer and sublattice distribution of these modes. We expect the exact nature of the distribution of these modes to depend sensitively on the strain levels at these interfaces.

The relaxation model employed here is a simplification that allowed us to examine, in a general manner, the role of interface sharpness in such systems. So far we have considered a pure uniaxial strain which creates a strictly 1D modulation of the stacking order. Allowing for a biaxial strain, or a Poisson compression of the strained layer, produces a 2D Moiré pattern [156]. We will explain in Chapter 5 how this will modify the emergent network of interface states. We expect that the channels associated with the AA-stacked interface will no longer contribute to the network, as in tBLG, while those associated with the SP-stacked regions will remain. However, their configuration is likely to be different from those in tBLG. Therefore, hBLG is a very promising platform from which to tune the presence and distribution of topological channels. This system could potentially exhibit phenomena akin to those in tBLG while circumventing some of the limitations associated with achieving precise twist angles.

Chapter 5 2D Moiré physics in heterostrained bilayer graphene

5.1 Introduction

In Chapter 4 we investigated the formation and evolution of interface-localized topological channels in 1D Moiré patterns, which emerge due to the different stacking registries between the two layers of a hBLG. The necessary condition for the formation of topological channels was to include large interlayer bias, as well as larger AB/BA-stacked regions and sharper interfaces. For simplification, we neglected the Poisson contraction, which results in a compression perpendicular to the applied uniaxial strain [157].

Here, we investigated the formation of interface channels for the same system (hBLG), including Poisson contraction ν. Poisson contraction is the deformation in the direction which is perpendicular to the applied strain. This deformation depends on the value of the applied strain (but it is much smaller in any case) and on the relevant material that is applied. For some materials, it is positive, which means that for uniaxial tensile applied strain we have contraction along the perpendicular in-plane direction (like graphene), while for some other materials, Poisson contraction is negative, which means that for uniaxial tensile applied strain, there is tension along the perpendicular in-plane direction. Poisson contraction, for MLG and BLG, is in the range from 0.16 to 0.46 [158–160]. The exact value of Poisson contraction depends on the amount of strain applied to graphene and the direction in which it is applied. With the inclusion of Poisson contraction in hBLG the layers are now mismatched in both directions and to different extents, which gives the

creation of networks of interface channels, as opposed to the 1D channels created for no Poisson contraction. However, we can eliminate to some degree Poisson contraction, by selecting substrates or encapsulating materials which have a Poisson ratio close to zero.

Poisson contraction has a broad spread, because its value depends on the material and the direction of the applied strain. For 1% applied heterostrain and Poisson ratio ν=0.4 the unit cell of hBLG has $\sim$200,000 carbon atoms, while for ν=0.2, which is a more realistic value of Poisson ratio for 1% heterostrain, the unit cell of hBLG has $\sim$400,000 carbon atoms. The aspect ratio of the unit cell changes, due to the different Poisson ratio, which will affect the overall shape, but we expect the qualitative features (networks of channels) to persist. Poisson contraction will also likely depend on substrate effects and may be different for heterostrain than uniform strain applied to both layers. For small values of strain (ε<2%), the Poisson ratio was found to be isotropic and not to be affected by the direction of the applied strain. For graphene and for low values of strain the Poisson contraction was found to have value ν $\sim$0.17-0.18. Here, we applied a low value of uniaxial heterostrain (ε=1%), we chose Poisson contraction ν=0.4. Changing the value of Poisson contraction affects the aspect ratio of the Moiré pattern. We magnified the effect to see how it affects the electronic properties and to reduce the system size, but lower values of Poisson contraction have to be checked in the future. In tBLG this is fixed and does not depend on the angle.

The unit cell of hBLG for these parameters consists of 201,400 carbon atoms and is depicted in Figure 5.1 (a) in the dashed box. The white color corresponds to the SP-stacked regions, which are connected through the AA-stacked regions. The blue and the red colors correspond to the energetically favorable AB- and BA-stacked domains respectively. The Moiré domains of this system consist of a triangular network of 1D interface channels (SP-stacked domains) connected with each other through the junctions (AA-stacked regions), as opposed to the 1D interface channels observed in hBLG where the Poisson contraction was neglected (Figure 4.6). A similar triangular network of interface channels is formed in tBLG and is depicted in Figure 5.1 (b), where the gray regions show the SP-stacked interface channels, the yellow color is associated with the AA-stacked domains, the pink color with the AB-stacked regions and the blue color with the BA-stacked domains.

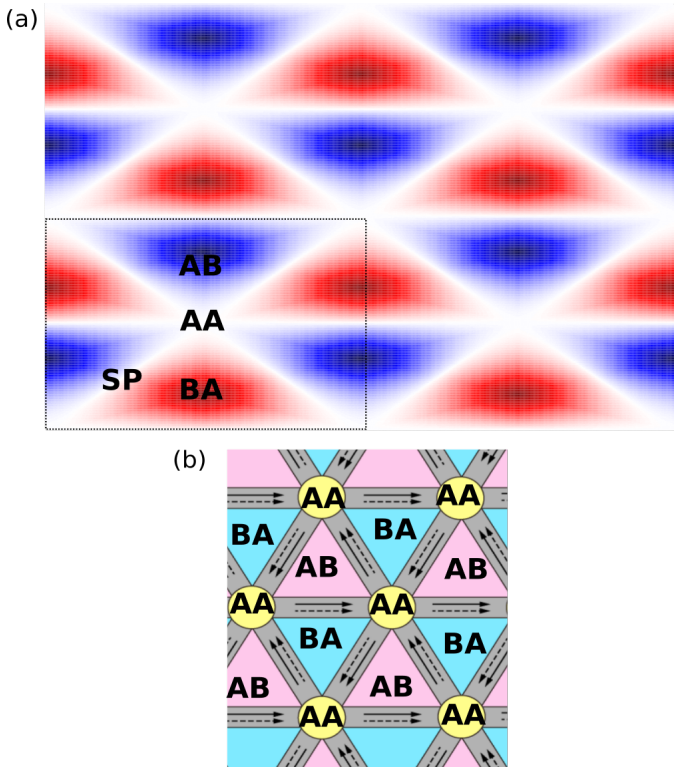

Figure 5.1: *(a) hBLG with 1% uniaxial tensile heterostrain applied along the AC direction (y) and Poisson contraction ν=0.4 applied along the perpendicular ZZ direction (x). The AA- and SP-stacked domains are depicted with white color and the energetically favorable AB- and BA-stacked domains with blue and red color respectively. The unit cell of hBLG is shown in the dashed box. (b) Networks of interface channels for tBLG (similar to the networks of interface channels for hBLG), where the grey domains correspond to SP-stacked regions, the pink domains to AB-stacked regions, the blue color to BA-stacked regions, and the yellow color to AA-stacked domains. Figure (b) adapted from [92].*

Before considering the heterostrained case, it is worth revisiting the twisted system, where similar interface channels are created. The formation of interface states in tBLG, which are localized under the application of large enough interlayer bias, was investigated with continuum model and TB calculations [54, 89, 99, 100] for small twist angles (θ<1.5°). Furthermore, the interface states in tBLG were investigated with experimental tools, in which STM measurements and fast Fourier transform were used to the extracted topography [101] and with spectroscopic measurements [102]. Depleted electronic states were found in the AB/BA-stacked domains and conducting states in the AA- and SP-stacked domains. By taking into account the local strains due to the twist angles, which maximize AB/BA-stacked domains, sharpen SP-stacked regions, and minimize AA-stacked domains, it was proven that there is strong localization in the AA-stacked domains for small twist angles $\theta \leq 1.1°$. In Magic-Angle tBLG ($\theta \sim 1.1°$), the localization of states is maximised [93]. There is the creation of ultraflat bands for low energies, which are associated with enhanced DOS and correlated insulating states at half-filling [94]. Both tBLG and hBLG systems present similar Moiré domains (Figures 5.1 (a) and (b)) and consequently we expect that similar effects could emerge in hBLG. For instance, *ab initio* calculations, in which out-of-plane relaxation was allowed, showed that for 1% uniaxial heterostrain applied on BLG, there is the formation of flat bands [96], similar to the ones found in tBLG [94].

We determined the total and local electronic properties, as well as the transport properties of the interface channels of hBLG, by calculating the TDOS, LDOS, and transmission, T, across this system. We compared our results with and without the application of interlayer bias because, in the previous Chapter 4, we showed that both the application of interlayer bias and the inclusion of the effect of relaxation are vital for the formation of 1D topological channels in the hBLG system. We ignored the effect of relaxation because the model of the sigmoid function is too simple to work here, and this system is huge. To overcome this, we applied larger interlayer bias on hBLG (Δ=-800 meV instead of Δ=-400 meV that we used in the previous study in Chapter 4), because the smoother the effect of relaxation the larger bias is required as shown in Figure 4.10 (b). We speculate that relaxation will enhance the 1D channels for lower applied bias. We leave confirmation of

this for future work. Section 5.2 has the details of TB calculations for determining TDOS and transmission, T, for low energies. Also, the computational details for the calculation of LDOS for specific energies are contained. Section 5.3 includes preliminary results of our study, where possible extensions are discussed in Section 5.4.

5.2 Computational details

We performed TB calculations, using the RGF method with the Rubio-Sancho approach (Section 2.4.2) to determine the electronic and transport properties of hBLG. The supercell was split into subcells and we used sparse matrices to store Hamiltonians of the very large system ($\sim$ 200,000 carbon atoms) due to memory. The size of each subcell varies due to the application of heterostrain. This is because the distribution of carbon atoms is different on the bottom L1 layer and the top L2 layer. For example, most of the subcells contain 804 carbon atoms, but some others have 811, 823 or 837 carbon atoms.

We included periodicity along x-direction by taking into account the self-energies of the two leads (left and right) and periodicity along y-direction by including the Bloch phases. We applied 1% uniaxial strain on the L1 layer along the AC direction and Poisson contraction ν=0.4 along the ZZ direction. We used 251 four-atom-cells for the L1 layer along the ZZ direction and 100 four-atom-cells along the AC direction and 250 and 101 four-atom-cells for L2 respectively. The unit cell of hBLG has in total of 201,400 carbon atoms. Concerning the k-space along y-direction we used 7 k_y points for hBLG. We used 100 energy points for the energy range from -0.5 eV to +0.5 eV and from -0.1 eV to +0.1 eV, to determine the TDOS and the transmission, T.

5.3 Electronic and transport properties of heterostrained graphene

The key features in tBLG systems are the formation of networks of topological channels under the application of interlayer bias and the inclusion of the effect of relaxation. Also, strong localization of electronic states for very low energies in the AA-stacked domains

was found with TB calculations [93]. We expect to find similar states in the corresponding domains in hBLG.

For the study of the electronic properties of hBLG, we begin by considering the TDOS in a wide energy range of -0.5 eV to +0.5 eV without an interlayer bias (Figure 5.2 (a)). We compared these results for the same system for TDOS in the same energy range but with Δ=-800 meV bias applied on both layers. Because we did not take into account the effect of relaxation we applied larger interlayer bias to the system, compared to the previous study in Chapter 4 (Δ=-400 meV). Without the inclusion of relaxation, the AB- and BA-stacked regions are smaller and we expect to have a pseudogap for the AB/BA-stacked regions for larger bias, as shown in Figure 4.10 (b). From Figures 5.2 (a) and (b), we can possibly observe a small bump for the TDOS for low energies near half-filling, only when interlayer bias is applied.

However, there are many peaks for both without and with the inclusion of interlayer bias, and is difficult to clearly resolve features with any certainty. We need to mention that these results are preliminary. These 'noise-like' features do not seem the result of numerical methods, as they appear in the same places as the number of k points and convergence parameters, η and ϵ_{GF}, are varied. Further work is required to verify exactly this, because these 'noise-like' features may indicate errors in the Hamiltonian or GFs, rather than real features.

We are interested in the electronic properties of the system near half-filling and we want to determine whether this is an actual bump in the TDOS. For this reason, we plotted the TDOS for lower energies (from -0.1 eV to +0.1 eV for 100 energy points), as shown in Figures 5.3 (a) and (b) without and with the application of Δ=-800 meV interlayer bias respectively. When the interlayer bias is applied, for energies close to Fermi level E_{F} (from $\sim$30 meV to $\sim$50 meV) the TDOS of hBLG has indeed a prominent bump, while for no bias this is not observed. In tBLG a similar feature is associated with the strong localization of states in the AA-stacked regions for low energies [93]. We also expect the formation of clear SP-stacked topological channels with the application of interlayer bias in hBLG.

To investigate the distribution of states and determine if these properties are indeed present in our system, we calculated and mapped the distribution of states (LDOS) for

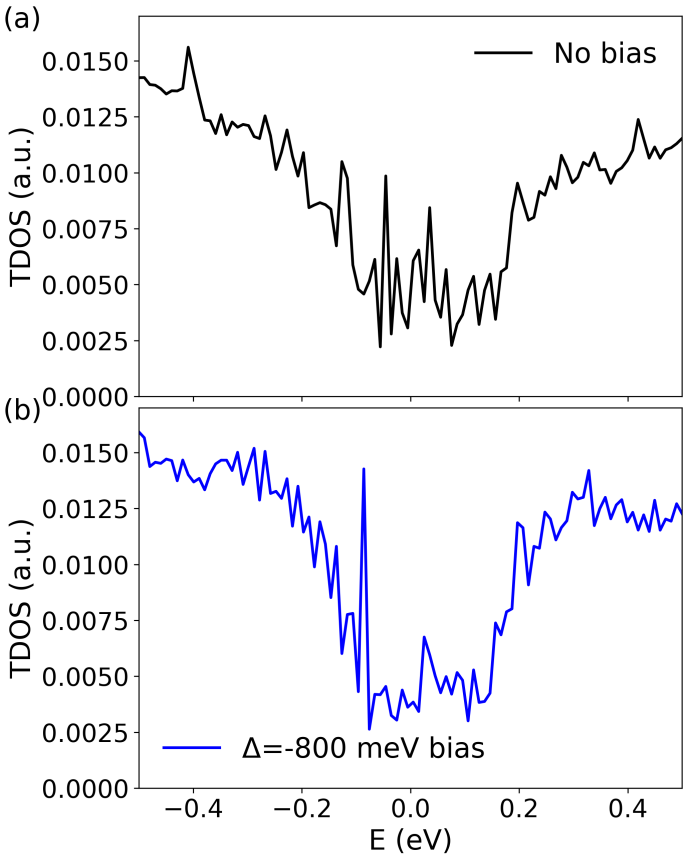

Figure 5.2: *TDOS for the energy range from -0.5 eV to +0.5 eV (a) without and (b) with the application of Δ=-800 meV interlayer bias.*

energies close to Fermi level E_F. For no bias, we chose three energies, E=-45 meV, E=-35 meV, and E=35 meV, which correspond to a small peak, a small dip, and a small peak respectively in the relative TDOS graph (shown by the red dots in Figure 5.3 (a)). The LDOS for these three energies is depicted in Figures 5.4 (a)–(c) and are in the logarithmic scale. We can observe subtle differences between these three plots and for some energies there seems to be more localization of the electronic states on the AA-stacked domains (the energy which corresponds to the dip E=35 meV). However, there is no strong spatial dependence on the electronic properties of the LDOS. This means that electronic states in this system, in general, are delocalized across the entire system.

For comparison, the LDOS when interlayer bias Δ=-800 meV is applied is shown for three energies, E=11 meV (Figure 5.5 (a)), E=17 meV (Figure 5.5 (b)) and E=39 meV (Figure 5.5 (c)), which correspond to a small peak and a small dip outside the prominent

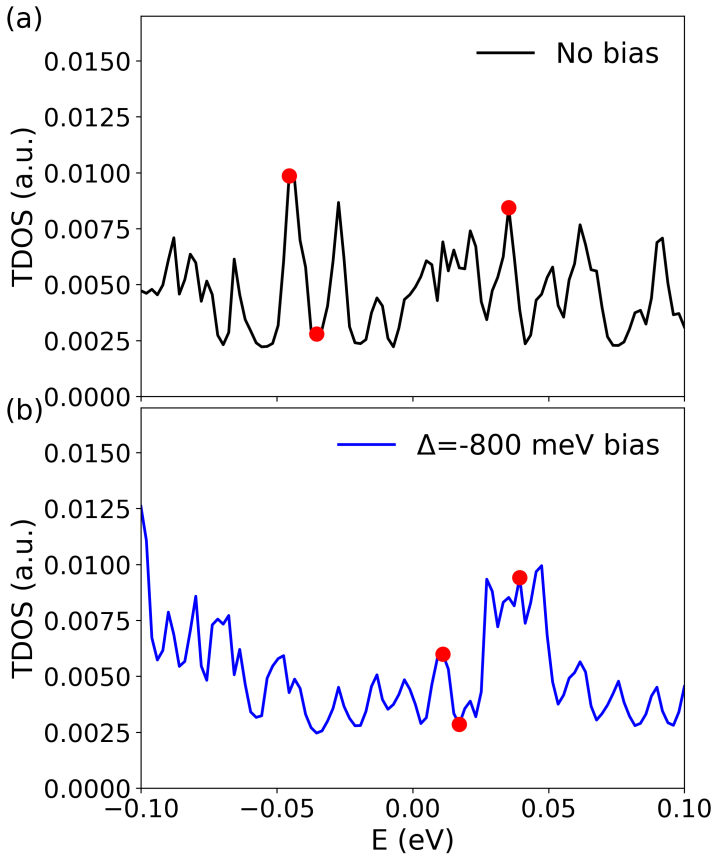

Figure 5.3: *TDOS for the energy range from -0.1 eV to +0.1 eV (a) without and (b) with the application of interlayer bias Δ=-800 meV. The selected energies for no bias (E=-45 meV, E=-35 meV, and E=35 meV in this order) and for applied interlayer bias (E=11 meV, E=17 meV and E=39 meV in this order) for the LDOS are shown in red dots respectively.*

bump, and a small peak inside the prominent bump respectively (Figure 5.3 (b)). The LDOS is on a logarithmic scale and for all these cases it has a distinctive pattern. For all these energies the AB- and BA-stacked domains appear to be depleted electronically. However, for the energy that corresponds to the prominent bump, E=39 meV, there is an enhancement of the electronic states which are localized in the AA-stacked domains at the corners and center of the mapped region, as happens in tBLG.

Moreover, from the comparison of the Figures 5.5 (a)–(c) we can deduce that the SP-stacked channels are dispersive, because they occur over a range of energies (same pattern for LDOS), while the very bright AA spots (associated with high LDOS) occur in the relevant 'bump'. The same qualitative physics occurs in tBLG (localized AA-stacked domains, dispersive SP-stacked channels). The difference between tBLG and hBLG is that

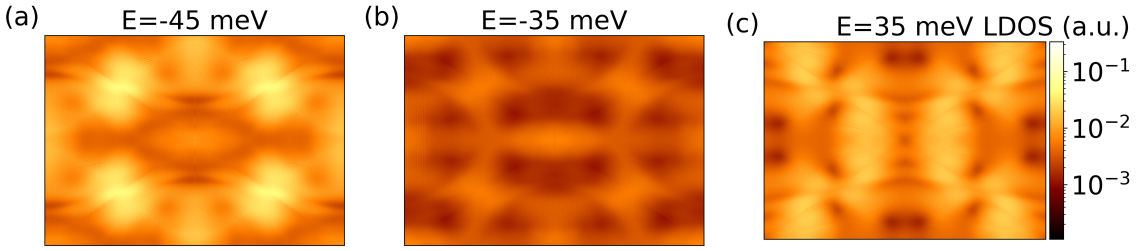

Figure 5.4: *LDOS for (a) E=-45 meV, (b) E=-35 meV and (c) E=35 meV for the unit cell of 1% hBLG without interlayer bias. The LDOS is on a logarithmic scale.*

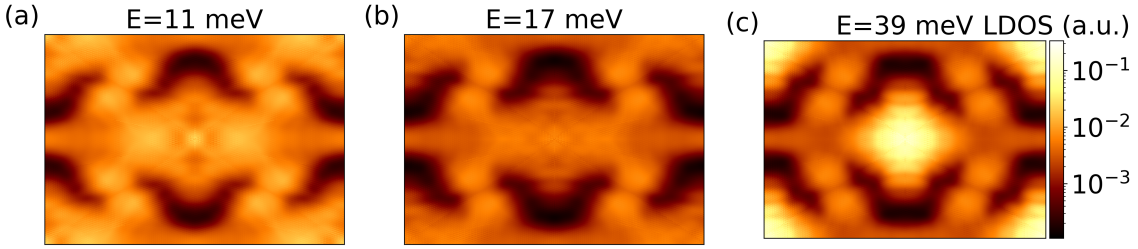

Figure 5.5: *LDOS for (a) E=11 meV, (b) E=17 meV and (c) E=39 meV for the unit cell of 1% hBLG under the application of Δ=-800 meV interlayer bias. The LDOS is on a logarithmic scale.*

in tBLG the SP-stacked channels are straight lines (gray areas in Figure 5.1 (b)), while for hBLG there is a distinctive new pattern if the SP-direction has a y-component, as opposed to the x-component. In Figure 5.6 (b) the white SP lines along the x-direction, do not appear to be as strongly affected by the larger y-direction strain (green lines). For comparison, the stacking of hBLG is depicted in Figure 5.6 (a). We explain this by the fact that the strain applied along the AC direction is larger than the strain applied along the ZZ direction, which means that not all the SP directions are the same anymore. Also, STM measurements have very recently shown that biaxial strain lower than 1.5% applied only to one of the two layers, due to the contact with the SiC substrate, leads to the formation of swirl topological channels (SP-stacked domains), under atomic reconstruction [151]. In both cases, the shape of the topological channels is affected by strain, unlike the regular triangular networks in tBLG.

Next, we consider the transport properties of this system, which are related to its electronic properties. Generally, we expect the transmission, T, to have similar features to the TDOS. We showed how transmission, T, changes with respect to energy for the energy

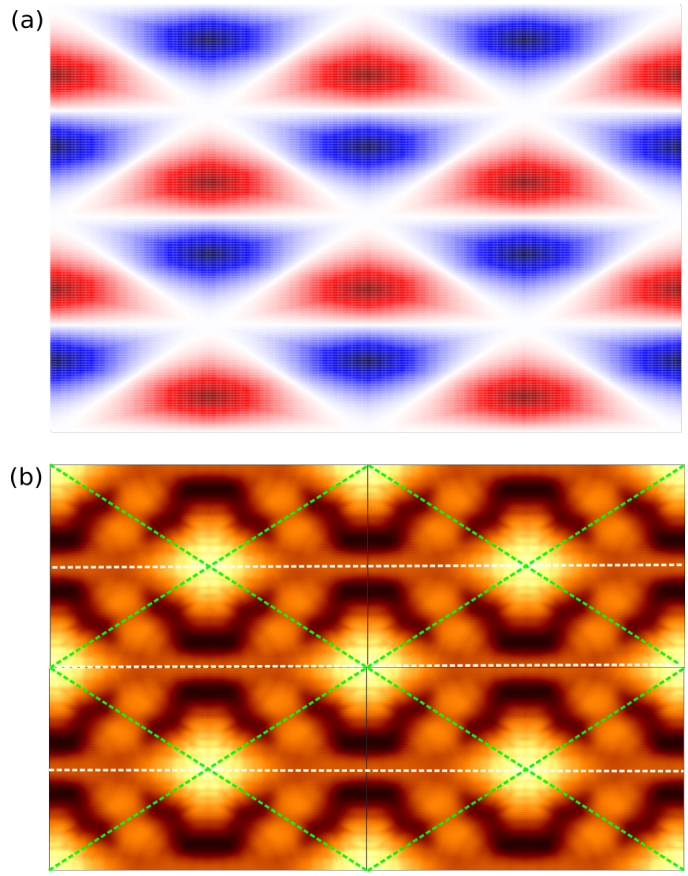

Figure 5.6: *(a) hBLG with 1% uniaxial tensile heterostrain applied along the AC direction (y) and ν=0.4 Poisson contraction applied along the ZZ direction (x). The AA- and SP-stacked domains are depicted with white color and the energetically favorable AB- and BA-stacked domains with blue and red color respectively. (b) LDOS for the same structure in Figure (a), for E=39 meV for hBLG under the application of Δ=-800 meV interlayer bias. We have included four unit cells, to show the topological channels which are created. The LDOS is on a logarithmic scale.*

range from -0.5 eV to +0.5 eV with and without the application of interlayer bias (Figure 5.7). For low energies close to Fermi level E_F there is a prominent dip with the application of interlayer bias in a narrow energy range near half-filling (from ∼-5 meV to ∼65 meV). This corresponds to the opening of a pseudogap in AB- and BA-stacked regions which reduces the number of transport channels through the system.

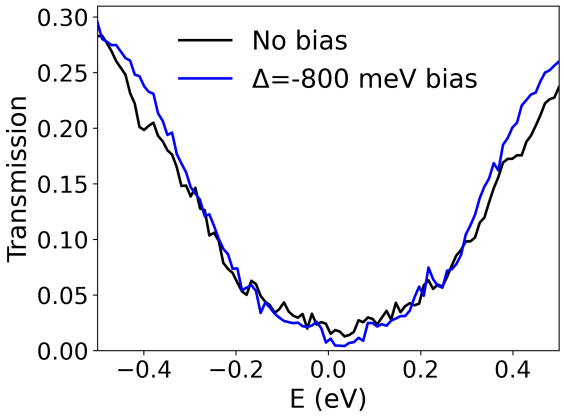

Figure 5.7: *Transmission, T, for the energy range from -0.5 eV to +0.5 eV without and with the application of Δ=-800 meV interlayer bias.*

We are interested in the transport properties of hBLG for low energies, so we plotted the transmission for energy range from -0.1 eV to +0.1 eV near the dip without (Figure 5.8 (a)) and with the application of Δ=-800 meV interlayer bias (Figure 5.8 (b)). For the same energy range as we have already computed the TDOS (Figures 5.3 (a) and (b) respectively) we may expect correspondence between these plots, as the 'bump' in the TDOS should correspond to a dip in the transmission graph for the same energy. However, the results do not coincide completely with the case of interlayer bias. The bump of TDOS is observed for the energy range from ∼30 meV to ∼50 meV and the dip of transmission for the energy range from -5 meV to +65 meV. This is because the system is complicated and the relevant states are not evenly distributed throughout the system and not all of them contribute to transport. Localized states in AA-stacked domains, for instance, do not contribute to the overall transmission, as they are not strongly connected to each other, even if they are strongly localized. The SP-stacked channel states are spread throughout the system in certain stacking regions, but they can carry current. The transmission, when interlayer bias Δ=-800 meV is applied, is close to zero, but still nonzero. This is because even

if some domains become electronically depleted due to the application of interlayer bias (AB/BA-stacked domains) and correspond to zero transmission, there are still domains that contribute to nonzero transmission (SP-stacked domains). This is why the value of transmission for low energies is still nonzero. On the other hand, the new localized AA states, which give a prominent TDOS bump, do not contribute to transport and have no signature in Figure 5.8 (b). For no bias, the transmission is slightly bigger.

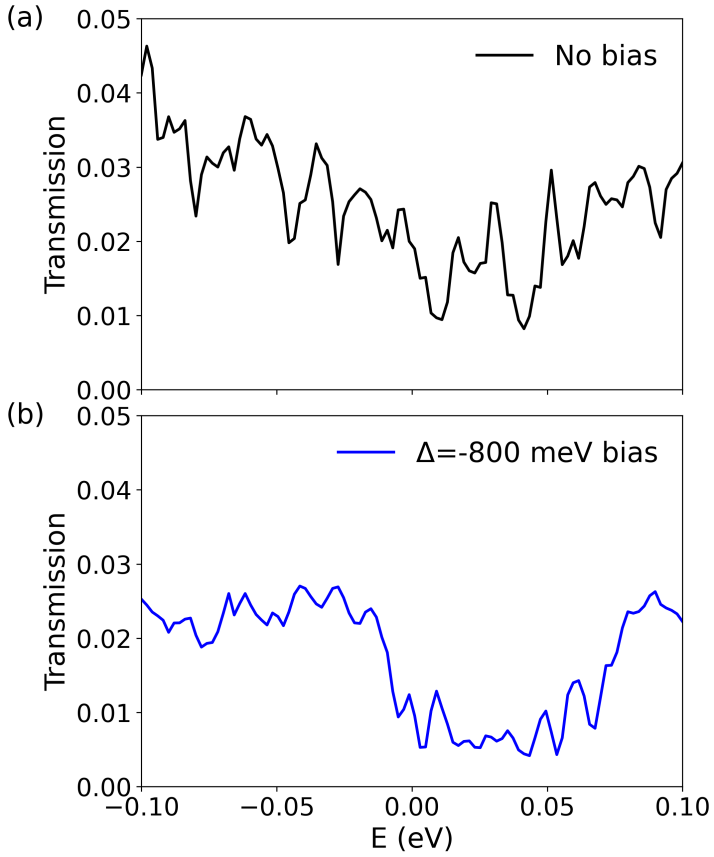

Figure 5.8: *Transmission, T, for the energy range from -0.1 eV to +0.1 eV (a) without and (b) with the application of Δ=-800 meV interlayer bias.*

5.4 Summary of Chapter

Overall, we found that there is a strong spatial variation of the states in hBLG under the application of large interlayer bias along the interface topological channels. For very low energies, we find the signature of strong localization in the AA-stacked domains, which is

associated with the formation of flat bands, as in tBLG. Also, SP-stacked interface channels were formed, which occur over a range of energies (dispersive channels), as happens for tBLG. However, these topological channels do not have the expected straight channels, but a distinctive zigzag pattern. We explained this, due to the fact the strain applied to the AC and the ZZ direction is not the same, affecting the shape of interface channels. Moreover, the transmission has very low values due to the existence of the AB/BA-stacked gapped domains in hBLG with the application of large interlayer bias, compared to no bias.

Also, in Figures 5.2 and 5.3, which show the TDOS as a function for energy for different energy intervals, there is the existence of some local peaks. If these peaks are indeed real features, they may correspond to localized states. Similar dips we found in the graphs of the transmission as a function of energy (Figures 5.7 and 5.8), which can indicate the existence of localized states. Further study is required to verify these. Consequently, heterostrained untwisted BLG is an alternative way to tune the electronic and transport properties of BLG, compared to tBLG, overcoming limitations relevant to achieving precise twist angle [105].

As future work, we could extend this analysis for smaller and bigger values of heterostrain to find how the distribution of states is affected by the amount of uniaxial heterostrain and for which value of strain the localization in the energetically unfavorable AA-stacked domains was maximum. TB calculations for tBLG, performed by Nguyen et al, showed that for twist angle $\theta \sim 1.1^\circ$ is a critical value where the localization of states in the AA-stacked domains is maximised [93]. For twist angles $\theta > 1.1^\circ$ the atomic relaxation is negligible and the low Dirac electrons are conserved. On the other hand, for twist angles $\theta < 1.1^\circ$ there is strong spatial variation and localization in the AA stacking regions. However, as the twist angle θ is reduced the relative contribution of the AA-stacked domains is decreased. As a consequence, the isolated flat bands close to Fermi level E_{F} and the strong electron localization do not contribute to the global electronic properties of the system. Also, we could include a more realistic value for the Poisson contraction (as explained in Section 5.1), or directly relax the system.

Concerning the transport properties of this system, we could show how the transmission is modified as a function of energy, as well as by changing the value of the uniaxial applied heterostrain. Relevant TB calculations for tBLG demonstrated that the system's

transmission can be tuned by varying the energy and the twist angle θ [161]. Similar calculations could be performed for hBLG. We could also investigate for which stackings we observe localized current for low energies and for specific values of strain (e.g. ε=1%), as studies showed for tBLG [161].

Chapter 6 Conclusions and future work

6.1 Summary of thesis

In this thesis we used *ab initio* and semi-empirical methods to study the energetic, electronic, and transport properties of hBLG. We considered small values of heterostrain, in line with what is achievable experimentally. This system has similar Moiré domains to the ones found in tBLG and consequently, we wanted to investigate if similar properties would emerge in this system.

In Chapter 2 we described the *ab initio* and analytical methods that we used in this thesis. The DFT method, which is an *ab initio* method, is used to calculate the ground state properties of many-electron systems. The main disadvantage of this method is its relatively high computational cost. We also explained the TB method, which gives more qualitative results compared to DFT, but with a significantly reduced computational cost. TB methods were used to investigate the electronic properties of large systems, such as hBLG with 1% applied uniaxial heterostrain on one of the two layers. Uniaxial strain was included in the model, through a modification of hopping terms. For some other calculations that required the study of even larger systems ($\sim$200,000 carbon atoms for 1% heterostrain and $\nu \neq 0$), we used the TB method within RGF formalism, which reduces further the computational cost.

In Chapter 3 we performed DFT calculations to find the value of critical strain applied only to one of the two layers at which the stacking order in BLG changes. We found that

above a critical strain of $\sim$1%, it is energetically favorable for the free top layer to be unstrained, indicating a transition between uniform AB-stacking and non-uniform mixed stacking. This was in agreement with a simple model estimate based on the individual energy contributions of strain and stacking effects. Our findings suggest that small levels of strain provide a platform to reversibly engineer stacking order and Moiré features in BLG, providing a viable alternative to twistronics to engineer topological and exotic physical phenomena in such systems.

In Chapter 4 we performed TB calculations to study the local electronic properties in hBLG at a 1% strain. We found that the application of both an interlayer bias and the inclusion of relaxation effects is vital for observing the formation of 1D topological channels. A simple model was used to account for the in-plane atomic reconstruction caused by the changing of the stacking registry due to the application of heterostrain. As a result, the AB and BA Bernal stacked domains were larger and the interface channels (AA- and SP-stacked regions) were sharper, leading to robust topological interfaces. These states are highly localized in the interfaces and exhibit differences in their layer and sublattice distribution depending on the interface stacking (AA or SP). Consequently, heterostrain can be used as a mechanism to tune the presence and distribution of topological channels in gapped BLG systems, complementary to the field of twistronics.

In Chapter 5 we investigated how the 2D Moiré patterns that emerge with the inclusion of a Poisson contraction affect the properties of hBLG. We used the RGF method with the Rubio-Sancho approach to determine the TDOS, LDOS, and transmission, T. We did not include local relaxation in this case to simplify the structure. To compensate, we applied a larger interlayer bias. Networks of topological interface channels were formed. For very low energies we showed the strong localization in the AA-stacked domains, which are associated with the flat bands, as in tBLG. SP-stacked dispersive channels were also created, but they did not have the expected pattern. This may be due to the fact that hBLG has different values of strain along the AC and the ZZ direction, which introduces an anisotropy that is present in heterostrained systems.

Overall, we showed that heterostrain is an alternative to twisting BLG. The difference is that hBLG allows different Moiré features, with different wavelengths in the x and y

directions. Also, the level of the applied strain can be changed in-situ in hBLG, whereas the twist angle θ cannot, because of the expeirmental methods.

6.2 Future work

Our work comprises the study of many properties for hBLG, such as the tuning of stacking, the electronic, and the transport properties. These calculations can extended. For example, the study of the electronic properties of hBLG as a function of uniaxial heterostrain would be very interesting. Similar studies in tBLG found that the electron localization is maximized in specific domains for particular twist angles. It is unknown whether the magnitude of strain can be used to tune localization in hBLG.

Moreover, different values of Poisson contraction can be used instead of ν=0.4 for the calculations in Chapter 5. Poisson contraction for graphene has values in the range from 0.16 to 0.46, depending on the magnitude direction of applied strain [158–160]. For small strains (ε<2%), the Poisson ratio was found to be ν ∼0.17-0.18. Thus, the effect of ν on the electronic and transport properties of hBLG could be investigated in more detail.

For simplicity in Chapter 4 we have only considered a single value of α within each structure so that the local strain at the AA- and SP-stacked interfaces is the same. However, these interfaces have different local stacking energetics, relative shifts, and widths, and so may be able to sustain different levels of local strain. We do not expect these considerations to dramatically alter the main trends in our results. The main effect is likely to be that these more complicated relaxed geometries could reduce the energy costs due to strain beyond the values predicted by our simple model, leading to an increased preference for sharper interfaces.

It is worth considering additional factors that may affect strain redistribution in hBLG, with and without the Poisson contraction ν. For both systems, substrate effects were neglected, except in the simplifying assumption that relaxation only occurs in one layer of the system in Chapter 4. The specific nature of the interaction between the substrate, or any tips or contacts used for either the application of strain or other measurements, may also affect the local distribution of strain in the system. It is feasible to study the effects

of a substrate theoretically, as several DFT studies have been done for graphene on top of a substrate, like SiC, Si(100), h-BN, SiO_2 and Al_2O_3 [162]. However, it could be difficult to study on the scale required for this system. We could perhaps include the effects of certain substrates (doping, disorder, charge puddles etc.) by varying the TB model used to describe the graphene layer in contact with it.

Also, we have not considered the role that out-of-plane deformations could play in reducing the total energy of heterostrained systems, as happens for tBLG systems. The local stacking energy is sensitive to modulations of the interlayer separation introduced by such deformations, as DFT calculations showed for tBLG with small twist angle θ [163]. This has an effect on hBLG, as recent work showed that such out-of-plane deformations can affect flat band formation and local chemical reactivity in this type of system [96]. Additionally, the effect of the compressive strain should be further investigated for the local electronic and transport properties of hBLG [96]. In-plane deformations should be considered as well because STM measurements showed that they exist for biaxially strained BLG [151]. However, including the relaxation effects using the simple method mentioned in Chapter 4 for biaxially strained BLG (hBLG with Poisson contraction) is difficult, because this is applicable only to uniaxially strained systems. One method for the inclusion of local in-plane deformations in hBLG is to use configuration space, as has been employed for tBLG and twisted MoS_2 [164]. This method accounts for the local deformations and has minimal computational cost.

Concerning the transport properties of this hBLG, we could investigate how the transmission changes as a function of energy, as well as with the applied uniaxial heterostrain. Relevant TB calculations for tBLG demonstrated that the system's transmission can be tuned by varying the energy and the twist angle θ [161]. We could also find out for which stackings we observe localized current for low energies and for specific values of strain (e.g. ε=1%), as studies showed for tBLG [161].

As already mentioned in Chapter 1, the inclusion of 5/7-membered rings (SW defect) affects the electronic properties of BLG. We also showed that the application of heterostrain affects the electronic properties of BLG (Chapters 4 and 5). Because both the application of heterostrain and the inclusion of a SW defect lead to a gapped system with bias, the

combination of both might require lower bias to tune its electronic properties, but additional studies are required.

Overall, these calculations can be extended for other layered systems. For example, similar DFT calculations that were performed in Chapter 3 could be implemented in other layered materials. Instead of two graphene, we can have two layers of MoS_2 and find the effect of heterostrain for this system. The effect of heterostrain for the tuning of stacking could be investigated for heterostructures as well, such as graphene/MoS_2. Also, the effect of heterostrain could be investigated for the electronic and transport properties of other layered systems, like bilayer MoS_2. TB methods can be extended to systems like MoS_2 [165].

List of Publications

- N Georgoulea, S Power, and N Caffrey. Strain-induced stacking transition in bilayer graphene. Journal of Physics: Condensed Matter, 34(47):475302, 2022, DOI: 10.1088/1361-648X/ac965d.
- N Georgoulea, N Caffrey, and S Power. One-dimensional topological channels in heterostrained bilayer graphene. Physical Review B, 109(3):035403, 2024, DOI: 10.1103/PhysRevB.109.035403.

References

[1] P Wallace. The band theory of graphite. *Physical review*, 71(9):622, 1947.

[2] K Novoselov, D Jiang, F Schedin, T Booth, V Khotkevich, S Morozov, and A Geim. Two-dimensional atomic crystals. *Proceedings of the National Academy of Sciences*, 102(30):10451–10453, 2005.

[3] K F Mak, C Lee, J Hone, J Shan, and T Heinz. Atomically thin MoS_2: A new direct-gap semiconductor. *Physical Review Letters*, 105(13):136805, 2010.

[4] G Cassabois, P Valvin, and B Gil. Hexagonal boron nitride is an indirect bandgap semiconductor. *Nature Photonics*, 10(4):262–266, 2016.

[5] D Akinwande, C Brennan, S Bunch, P Egberts, J Felts, H Gao, R Huang, J-S Kim, T Li, Y Li, K Liechti, N Lu, H Park, E Reed, P Wang, B Yakobson, T Zhang, Y Zhou, and Y Zhu. A review on mechanics and mechanical properties of 2D materials—graphene and beyond. *Extreme Mechanics Letters*, 13:42–77, 2017.

[6] J M Kim, C Cho, E Hsieh, and S Nam. Heterogeneous deformation of two-dimensional materials for emerging functionalities. *Journal of Materials Research*, 35(11):1369–1385, 2020.

[7] M Katsnelson. Graphene: Carbon in two dimensions. *Materials Today*, 10(1-2):20–27, 2007.

[8] C Lee, X Wei, J Kysar, and J Hone. Measurement of the elastic properties and intrinsic strength of monolayer graphene. *Science*, 321(5887):385–388, 2008.

[9] M Zarenia, J Milton Pereira, A Chaves, F M Peeters, and G A Farias. Erratum: Simplified model for the energy levels of quantum rings in single layer and bilayer graphene. *Physical Review B*, 82(11):119906, 2010.

[10] T Ohta, A Bostwick, T Seyller, K Horn, and E Rotenberg. Controlling the electronic structure of bilayer graphene. *Science*, 313(5789):951–954, 2006.

[11] K Zou and J Zhu. Transport in gapped bilayer graphene: The role of potential fluctuations. *Physical Review B*, 82(8):081407, 2010.

[12] K Zou, F Zhang, C Clapp, A MacDonald, and J Zhu. Transport studies of dual-gated ABC and ABA trilayer graphene: Band gap opening and band structure tuning in very large perpendicular electric fields. *Nano Letters*, 13(2):369–373, 2013.

[13] C Androulidakis, K Zhang, M Robertson, and S Tawfick. Tailoring the mechanical properties of 2D materials and heterostructures. *2D Materials*, 5(3):032005, 2018.

[14] H Wang, F Liu, W Fu, Z Fang, W Zhou, and Z Liu. Two-dimensional heterostructures: Fabrication, characterization, and application. *Nanoscale*, 6(21):12250–12272, 2014.

[15] K Liu, Q Yan, M Chen, W Fan, Y Sun, J Suh, D Fu, S Lee, J Zhou, S Tongay, J Ji, J Neaton, and J Wu. Elastic properties of chemical-vapor-deposited monolayer MoS_2, WS_2, and their bilayer heterostructures. *Nano Letters*, 14(9):5097–5103, 2014.

[16] Q Guo, G Wang, R Pandey, and S Karna. Robust band gaps in the graphene/oxide heterostructure: SnO/graphene/SnO. *Physical Chemistry Chemical Physics*, 20(26):17983–17989, 2018.

[17] A Geim and I Grigorieva. Van der Waals heterostructures. *Nature*, 499(7459):419–425, 2013.

[18] L G De Arco, Y Zhang, A Kumar, and C Zhou. Synthesis, transfer, and devices of single-and few-layer graphene by chemical vapor deposition. *IEEE Transactions on Nanotechnology*, 8(2):135–138, 2009.

[19] A Reina, X Jia, J Ho, D Nezich, H Son, V Bulovic, M Dresselhaus, and J Kong. Large area, few-layer graphene films on arbitrary substrates by chemical vapor deposition. *Nano Letters*, 9(1):30–35, 2009.

[20] K S Kim, Y Zhao, H Jang, S Y Lee, J M Kim, K Kim, J-H Ahn, P Kim, J-Y Choi, and B H Hong. Large-scale pattern growth of graphene films for stretchable transparent electrodes. *Nature*, 457(7230):706–710, 2009.

[21] X Li, W Cai, J An, S Kim, J Nah, D Yang, R Piner, A Velamakanni, I Jung, E Tutuc, S Banerjee, L Colombo, and R Ruoff. Large-area synthesis of high-quality and uniform graphene films on copper foils. *Science*, 324(5932):1312–1314, 2009.

[22] Y Hernandez, V Nicolosi, M Lotya, F Blighe, Z Sun, S De, I McGovern, B Holland, M Byrne, Y Gun'Ko, J Boland, P Niraj, G Duesberg, S Krishnamurthy, R Goodhue, J Hutchison, V Scardaci, A Ferrari, and J Coleman. High-yield production of graphene by liquid-phase exfoliation of graphite. *Nature Nanotechnology*, 3(9):563–568, 2008.

[23] U Khan, A O'Neill, M Lotya, S De, and J Coleman. High-concentration solvent exfoliation of graphene. *Small*, 6(7):864–871, 2010.

[24] M Lotya, Y Hernandez, P King, R Smith, V Nicolosi, L Karlsson, F Blighe, S De, Z Wang, I McGovern, G Duesberg, and J Coleman. Liquid phase production of graphene by exfoliation of graphite in surfactant/water solutions. *Journal of the American Chemical Society*, 131(10):3611–3620, 2009.

[25] C Muratore, A Voevodin, and N Glavin. Physical vapor deposition of 2D Van der Waals materials: A review. *Thin Solid Films*, 688:137500, 2019.

[26] E Gao, S-Z Lin, Z Qin, M Buehler, X-Q Feng, and Z Xu. Mechanical exfoliation of two-dimensional materials. *Journal of the Mechanics and Physics of Solids*, 115:248–262, 2018.

[27] S Bhowmik and A G Rajan. Chemical vapor deposition of 2D materials: A review of modeling, simulation, and machine learning studies. *Science*, page 103832, 2022.

[28] J Shen, Y He, J Wu, C Gao, K Keyshar, X Zhang, Y Yang, M Ye, R Vajtai, J Lou, J Lou, and M Ajayan. Liquid phase exfoliation of two-dimensional materials by directly probing and matching surface tension components. *Nano Letters*, 15(8):5449–5454, 2015.

[29] J-U Lee, D Yoon, and H Cheong. Estimation of Young's modulus of graphene by Raman spectroscopy. *Nano Letters*, 12(9):4444–4448, 2012.

[30] K Bolotin, K Sikes, Z Jiang, M Klima, G Fudenberg, J Hone, P Kim, and H Stormer. Ultrahigh electron mobility in suspended graphene. *Solid State Communications*, 146(9-10):351–355, 2008.

[31] G Eda, G Fanchini, and M Chhowalla. Large-area ultrathin films of reduced graphene oxide as a transparent and flexible electronic material. *Nature Nanotechnology*, 3(5):270–274, 2008.

[32] B Feldman, B Krauss, J Smet, and A Yacoby. Unconventional sequence of fractional quantum hall states in suspended graphene. *Science*, 337(6099):1196–1199, 2012.

[33] Y Guo, B Wu, H Liu, Y Ma, Y Yang, J Zheng, G Yu, and Y Liu. Electrical assembly and reduction of graphene oxide in a single solution step for use in flexible sensors. *Advanced Materials*, 23(40):4626–4630, 2011.

[34] Y Wu, Y-M Lin, A Bol, K Jenkins, F Xia, D Farmer, Y Zhu, and P Avouris. High-frequency, scaled graphene transistors on diamond-like carbon. *Nature*, 472(7341):74–78, 2011.

[35] P Wang, W Zhang, O Liang, M Pantoja, J Katzer, T Schroeder, and Y-H Xie. Giant optical response from graphene-plasmonic system. *ACS Nano*, 6(7):6244–6249, 2012.

[36] N Xiao, X Dong, L Song, D Liu, Y Tay, S Wu, L-J Li, Y Zhao, T Yu, H Zhang, W Huang, H H Hng, P Ajayan, and Q Yan. Enhanced thermopower of graphene films with oxygen plasma treatment. *ACS Nano*, 5(4):2749–2755, 2011.

[37] M Allen, V Tung, and R Kaner. Honeycomb carbon: A review of graphene. *Chemical Reviews*, 110(1):132–145, 2010.

[38] M El-Kady, Y Shao, and R Kaner. Graphene for batteries, supercapacitors and beyond. *Nature Reviews Materials*, 1(7):1–14, 2016.

[39] Z Yin, J Zhu, Q He, X Cao, C Tan, H Chen, Q Yan, and H Zhang. Graphene-based materials for solar cell applications. *Advanced Energy Materials*, 4(1):1300574, 2014.

[40] L Foa Torres, S Roche, and J-C Charlier. *Introduction to graphene-based nanomaterials: From electronic structure to quantum transport*. Cambridge University Press, 2020.

[41] E McCann and M Koshino. The electronic properties of bilayer graphene. *Reports on Progress in Physics*, 76(5):056503, 2013.

[42] A V Rozhkov, A O Sboychakov, A L Rakhmanov, and F Nori. Electronic properties of graphene-based bilayer systems. *Physics Reports*, 648:1–104, 2016.

[43] K Novoselov, A Geim, S Morozov, D Jiang, Y Zhang, S Dubonos, I Grigorieva, and A Firsov. Electric field effect in atomically thin carbon films. *Science*, 306(5696):666–669, 2004.

[44] J-H Ho, C Lu, C Hwang, C Chang, and M-F Lin. Coulomb excitations in AA- and AB-stacked bilayer graphites. *Physical Review B*, 74(8):085406, 2006.

[45] C Park, J Ryou, S Hong, B Sumpter, G Kim, and M Yoon. Electronic properties of bilayer graphene strongly coupled to interlayer stacking and an external electric field. *Physical Review Letters*, 115(1):015502, 2015.

[46] I Razado-Colambo, J Avila, D Vignaud, S Godey, X Wallart, D P Woodruff, and M C Asensio. Structural determination of bilayer graphene on SiC (0001) using synchrotron radiation photoelectron diffraction. *Scientific Reports*, 8(1):1–10, 2018.

[47] H Zhang, T Pincelli, C Jozwiak, T Kondo, R Ernstorfer, T Sato, and S Zhou. Angle-resolved photoemission spectroscopy. *Nature Reviews Methods Primers*, 2(1):54, 2022.

[48] S Bhattacharyya and A Singh. Lifshitz transition and modulation of electronic and transport properties of bilayer graphene by sliding and applied normal compressive strain. *Carbon*, 99:432–438, 2016.

[49] Y-W Son, S-M Choi, Y P Hong, S Woo, and S-H Jhi. Electronic topological transition in sliding bilayer graphene. *Physical Review B*, 84(15):155410, 2011.

[50] E Castro, K Novoselov, S Morozov, N Peres, L Dos Santos, J Nilsson, F Guinea, A Geim, and C Neto. Biased bilayer graphene: Semiconductor with a gap tunable by the electric field effect. *Physical Review Letters*, 99(21):216802, 2007.

[51] E Silva, M Santos, J Skelton, T Yang, T Santos, S Parker, and A Walsh. Electronic and phonon instabilities in bilayer graphene under applied external bias. *Materials Today: Proceedings*, 20:373–382, 2020.

[52] C Coletti, S Forti, K Emtsev, and U Starke. Tailoring the electronic structure of epitaxial graphene on SiC (0001): Transfer doping and hydrogen intercalation. In *GraphITA 2011: Selected papers from the Workshop on Fundamentals and Applications of Graphene*, pages 39–49. Springer, 2012.

[53] F Zhang, A MacDonald, and E Mele. Valley chern numbers and boundary modes in gapped bilayer graphene. *Proceedings of the National Academy of Sciences*, 110(26):10546–10551, 2013.

[54] P San-Jose and E Prada. Helical networks in twisted bilayer graphene under interlayer bias. *Physical Review B*, 88(12):121408, 2013.

[55] L Dos Santos, N Peres, and C Neto. Graphene bilayer with a twist: Electronic structure. *Physical Review Letters*, 99(25):256802, 2007.

[56] G Anagnostopoulos, C Androulidakis, E Koukaras, G Tsoukleri, I Polyzos, J Parthenios, K Papagelis, and C Galiotis. Stress transfer mechanisms at the submicron level for graphene/polymer systems. *ACS Applied Materials & Interfaces*, 7(7):4216–4223, 2015.

[57] A Summerfield, A Davies, T Cheng, V Korolkov, Y Cho, C Mellor, T Thomas Foxon, A Khlobystov, K Watanabe, T Taniguchi, L Eaves, S Novikov, and P Beton. Strain-engineered graphene grown on hexagonal boron nitride by molecular beam epitaxy. *Scientific Reports*, 6(1):1–10, 2016.

[58] T Yu, Z Ni, C Du, Y You, Y Wang, and Z Shen. Raman mapping investigation of graphene on transparent flexible substrate: The strain effect. *The Journal of Physical Chemistry C*, 112(33):12602–12605, 2008.

[59] Z H Ni, T Yu, Y H Lu, Y Y Wang, Y P Feng, and Z X Shen. Uniaxial strain on graphene: Raman spectroscopy study and band-gap opening. *ACS Nano*, 2(11):2301–2305, 2008.

[60] M Huang, H Yan, C Chen, D Song, T Heinz, and J Hone. Phonon softening and crystallographic orientation of strained graphene studied by raman spectroscopy. *Proceedings of the National Academy of Sciences*, 106(18):7304–7308, 2009.

[61] C Androulidakis, E Koukaras, G Paterakis, G Trakakis, and C Galiotis. Tunable macroscale structural superlubricity in two-layer graphene via strain engineering. *Nature Communications*, 11(1):1–11, 2020.

[62] C Androulidakis, E Koukaras, J Parthenios, G Kalosakas, K Papagelis, and C Galiotis. Graphene flakes under controlled biaxial deformation. *Scientific Reports*, 5(1):18219, 2015.

[63] V Pereira, C Neto, and N Peres. Tight-binding approach to uniaxial strain in graphene. *Physical Review B*, 80(4):045401, 2009.

[64] T Mohiuddin, A Lombardo, R Nair, A Bonetti, G Savini, R Jalil, N Bonini, D Basko, C Galiotis, N Marzari, K Novoselov, A Geim, and A Ferrari. Uniaxial strain in

graphene by Raman spectroscopy: G peak splitting, Grüneisen parameters, and sample orientation. *Physical Review B*, 79:205433, 2009.

[65] G Tsoukleri, J Parthenios, K Papagelis, R Jalil, A Ferrari, A Geim, K Novoselov, and C Galiotis. Subjecting a graphene monolayer to tension and compression. *Small*, 5(21):2397–2402, 2009.

[66] O Frank, M Bousa, I Riaz, R Jalil, K Novoselov, G Tsoukleri, J Parthenios, L Kavan, K Papagelis, and C Galiotis. Phonon and structural changes in deformed bernal stacked bilayer graphene. *Nano Letters*, 12(2):687–693, 2012.

[67] T Jiang, R Huang, and Y Zhu. Interfacial sliding and buckling of monolayer graphene on a stretchable substrate. *Advanced Functional Materials*, 24(3):396–402, 2014.

[68] Y Jin, Q Ren, J Liu, Y Zhang, H Zheng, and P Zhao. Stretching graphene to 3.3% strain using formvar-reinforced flexible substrate. *Experimental Mechanics*, 62(5):761–767, 2022.

[69] M Mucha-Kruczyński, I Aleiner, and V Fal'ko. Strained bilayer graphene: Band structure topology and landau level spectrum. *Physical Review B*, 84(4):041404, 2011.

[70] H Zhang, J-W Huang, J Velasco Jr, K Myhro, M Maldonado, D D Tran, Z Zhao, F Wang, Y Lee, G Liu, W Bao, and C N Lau. Transport in suspended monolayer and bilayer graphene under strain: A new platform for material studies. *Carbon*, 69:336–341, 2014.

[71] A Popov, I Lebedeva, A Knizhnik, Y Lozovik, and B Potapkin. Commensurate-incommensurate phase transition in bilayer graphene. *Physical Review B*, 84(4):045404, 2011.

[72] Y Frenkel. The Frenkel-Kontorova model: Concepts, methods, and applications. *Phys Z Sowietunion*, 13:1, 1938.

[73] L Ju, Z Shi, N Nair, Y Lv, Chenhao Jin, J Velasco, C Ojeda-Aristizabal, H Bechtel, M Martin, A Zettl, J Analytics, and F Wang. Topological valley transport at bilayer graphene domain walls. *Nature*, 520(7549):650–655, 2015.

[74] T Naimer, K Zollner, M Gmitra, and J Fabian. Twist-angle dependent proximity induced spin-orbit coupling in graphene/transition metal dichalcogenide heterostructures. *Physical Review B*, 104(19):195156, 2021.

[75] R Majidi and K Ghafoori Tabrizi. Electronic properties of defect-free and defective bilayer graphene in an electric field. *Fullerenes, Nanotubes, and Carbon Nanostructures*, 19(6):532–539, 2011.

[76] B Liu, L-J Wu, Y-Q Zhao, L-Z Wang, and M-Q Cai. First-principles investigation of the schottky contact for the two-dimensional MoS_2 and graphene heterostructure. *RSC Advances*, 6(65):60271–60276, 2016.

[77] M Van der Donck, C De Beule, B Partoens, F M Peeters, and B Van Duppen. Piezoelectricity in asymmetrically strained bilayer graphene. *2D Materials*, 3(3):035015, 2016.

[78] M Anđelković, L Covaci, and F M Peeters. DC conductivity of twisted bilayer graphene: Angle-dependent transport properties and effects of disorder. *Physical Review Materials*, 2(3):034004, 2018.

[79] W Yao, E Wang, C Bao, Y Zhang, K Zhang, K Bao, C K Chan, C Chen, J Avila, M Asensio, J Zhu, and S Zhou. Quasicrystalline 30° twisted bilayer graphene as an incommensurate superlattice with strong interlayer coupling. *Proceedings of the National Academy of Sciences*, 115(27):6928–6933, 2018.

[80] S Dai, Y Xiang, and D Srolovitz. Twisted bilayer graphene: Moiré with a twist. *Nano Letters*, 16(9):5923–5927, 2016.

[81] H Yoo, R Engelke, S Carr, S Fang, K Zhang, P Cazeaux, S H Sung, R Hovden, A Tsen, T Taniguchi, K Watanabe, G C Yi, M Kim, M Luskin, E Tadmor, E Kaxiras,

and P Kim. Atomic and electronic reconstruction at the van der Waals interface in twisted bilayer graphene. *Nature Materials*, 18(5):448–453, 2019.

[82] K Uchida, S Furuya, J-I Iwata, and A Oshiyama. Atomic corrugation and electron localization due to Moiré patterns in twisted bilayer graphenes. *Physical Review B*, 90(15):155451, 2014.

[83] M Van Wijk, A Schuring, M Katsnelson, and A Fasolino. Relaxation of Moiré patterns for slightly misaligned identical lattices: Graphene on graphite. *2D Materials*, 2(3):034010, 2015.

[84] N Nam and M Koshino. Lattice relaxation and energy band modulation in twisted bilayer graphene. *Physical Review B*, 96(7):075311, 2017.

[85] S Carr, D Massatt, S Torrisi, P Cazeaux, M Luskin, and E Kaxiras. Relaxation and domain formation in incommensurate two-dimensional heterostructures. *Physical Review B*, 98(22):224102, 2018.

[86] X Lin, D Liu, and D Tománek. Shear instability in twisted bilayer graphene. *Physical Review B*, 98(19):195432, 2018.

[87] F Guinea and N Walet. Continuum models for twisted bilayer graphene: Effect of lattice deformation and hopping parameters. *Physical Review B*, 99(20):205134, 2019.

[88] L McGilly, A Kerelsky, N Finney, K Shapovalov, E-M Shih, A Ghiotto, Y Zeng, S Moore, W Wu, Y Bai, K Watanabe, T Taniguchi, M Stengel, L Zhou, J Hone, X Zhu, D Basov, C Dean, C Dreyer, and A Pasupathy. Visualization of Moiré superlattices. *Nature Nanotechnology*, 15(7):580–584, 2020.

[89] M Fleischmann, R Gupta, F Wullschläger, S Theil, D Weckbecker, V Meded, S Sharma, B Meyer, and S Shallcross. Perfect and controllable nesting in minimally twisted bilayer graphene. *Nano Letters*, 20(2):971–978, 2019.

[90] N Walet and F Guinea. The emergence of one-dimensional channels in marginal-angle twisted bilayer graphene. *2D Materials*, 7(1):015023, 2019.

[91] P Lucignano, D Alfè, V Cataudella, D Ninno, and G Cantele. Crucial role of atomic corrugation on the flat bands and energy gaps of twisted bilayer graphene at the magic angle $\theta \sim 1.08^\circ$. *Physical Review B*, 99(19):195419, 2019.

[92] B Tsim, N Nam, and M Koshino. Perfect one-dimensional chiral states in biased twisted bilayer graphene. *Physical Review B*, 101(12):125409, 2020.

[93] H Nguyen, D Paszko, M Lamparski, B Van Troeye, V Meunier, and J-C Charlier. Electronic localization in small-angle twisted bilayer graphene. *2D Materials*, 8(3):035046, 2021.

[94] Y Cao, V Fatemi, S Fang, K Watanabe, T Taniguchi, E Kaxiras, and P Jarillo-Herrero. Unconventional superconductivity in magic-angle graphene superlattices. *Nature*, 556(7699):43–50, 2018.

[95] P Stepanov, I Das, X Lu, A Fahimniya, K Watanabe, T Taniguchi, F Koppens, J Lischner, L Levitov, and D Efetov. Untying the insulating and superconducting orders in magic-angle graphene. *Nature*, 583(7816):375–378, 2020.

[96] G Schleder, M Pizzochero, and E Kaxiras. One-dimensional Moiré physics and chemistry in heterostrained bilayer graphene. *The Journal of Physical Chemistry Letters*, 14(39):8853–8858, 2023.

[97] W Jaskólski, M Pelc, L Chico, and A Ayuela. Existence of nontrivial topologically protected states at grain boundaries in bilayer graphene: Signatures and electrical switching. *Nanoscale*, 8(11):6079–6084, 2016.

[98] P Yasaei, B Kumar, R Hantehzadeh, M Kayyalha, A Baskin, N Repnin, C Wang, R Klie, Y Chen, P Král, and A Salehi-Khojin. Chemical sensing with switchable transport channels in graphene grain boundaries. *Nature Communications*, 5(1):1–8, 2014.

[99] D Efimkin and A MacDonald. Helical network model for twisted bilayer graphene. *Physical Review B*, 98(3):035404, 2018.

[100] C De Beule, F Dominguez, and P Recher. Network model and four-terminal transport in minimally twisted bilayer graphene. *Physical Review B*, 104(19):195410, 2021.

[101] J Verbakel, Q Yao, K Sotthewes, and H Zandvliet. Valley-protected one-dimensional states in small-angle twisted bilayer graphene. *Physical Review B*, 103(16):165134, 2021.

[102] S Huang, K Kim, D Efimkin, T Lovorn, T Taniguchi, K Watanabe, A MacDonald, E Tutuc, and B LeRoy. Topologically protected helical states in minimally twisted bilayer graphene. *Physical Review Letters*, 121:037702, 2018.

[103] A Vaezi, Y Liang, D Ngai, L Yang, and E-A Kim. Topological edge states at a tilt boundary in gated multilayer graphene. *Physical Review X*, 3(2):021018, 2013.

[104] J Alden, A Tsen, P Huang, R Hovden, L Brown, J Park, D Muller, and P McEuen. Strain solitons and topological defects in bilayer graphene. *Proceedings of the National Academy of Sciences*, 110(28):11256–11260, 2013.

[105] M Kapfer, B Jessen, M Eisele, M Fu, D Danielsen, T Darlington, S Moore, N Finney, A Marchese, V Hsieh, P Majchrzak, Z Jiang, D Biswas, P Dudin, J Avila, K Watanabe, T Taniguchi, S Ulstruo, P Boggild, P Schuck, D Basov, J Hone, and C Dean. Programming Moiré patterns in 2D materials by bending. *arXiv:2209.10696*, 2022.

[106] M Born and R Oppenheimer. On the quantum theory of molecules. *Annalen der Physik*, 389:457, 1927.

[107] P Hohenberg and W Kohn. Inhomogeneous electron gas. *Physical Review*, 136(3B):B864, 1964.

[108] W Kohn and L J Sham. Self-consistent equations including exchange and correlation effects. *Physical Review*, 140(4A):A1133, 1965.

[109] J Perdew and A Zunger. Self-interaction correction to density-functional approximations for many-electron systems. *Physical Review B*, 23(10):5048, 1981.

[110] D Ceperley and B Alder. Ground state of the electron gas by a stochastic method. *Physical Review Letters*, 45(7):566, 1980.

[111] R Martin. *Electronic structure: Basic theory and practical methods*. Cambridge university press, 2020.

[112] J Tao, J Perdew, V Staroverov, and G Scuseria. Climbing the density functional ladder: Nonempirical meta-generalized gradient approximation designed for molecules and solids. *Physical Review Letters*, 91(14):146401, 2003.

[113] A Becke. Density-functional thermochemistry. III. The role of exact exchange. *Chem. Phys*, 98:5648, 1993.

[114] S Grimme. Semiempirical GGA-type density functional constructed with a long-range dispersion correction. *Journal of Computational Chemistry*, 27(15):1787–1799, 2006.

[115] G Kresse and J Hafner. Ab initio molecular dynamics for liquid metals. *Physical Review B*, 47(1):558, 1993.

[116] G Kresse and J Hafner. Ab initio molecular-dynamics simulation of the liquid-metal-amorphous-semiconductor transition in germanium. *Physical Review B*, 49(20):14251, 1994.

[117] G Kresse and J Furthmüller. Efficiency of ab-initio total energy calculations for metals and semiconductors using a plane-wave basis set. *Computational Materials Science*, 6(1):15–50, 1996.

[118] G Kresse and J Furthmüller. Efficient iterative schemes for ab initio total-energy calculations using a plane-wave basis set. *Physical Review B*, 54(16):11169, 1996.

[119] P Blöchl. Projector augmented-wave method. *Physical Review B*, 50(24):17953, 1994.

[120] G Kresse and D Joubert. From ultrasoft pseudopotentials to the projector augmented-wave method. *Physical Review B*, 59(3):1758, 1999.

[121] F Bloch. Über die quantenmechanik der elektronen in kristallgittern. *Zeitschrift für physik*, 52(7-8):555–600, 1929.

[122] H Monkhorst and J Pack. Special points for Brillouin-zone integrations. *Physical Review B*, 13(12):5188, 1976.

[123] D J Thouless and S Kirkpatrick. Conductivity of the disordered linear chain. *Journal of Physics C: Solid State Physics*, 14(3):235, 1981.

[124] A MacKinnon. The calculation of transport properties and density of states of disordered solids. *Zeitschrift für Physik B Condensed Matter*, 59(4):385–390, 1985.

[125] R Kundu. Tight-binding parameters for graphene. *Modern Physics Letters B*, 25(03):163–173, 2011.

[126] J-C Charlier, J-P Michenaud, X Gonze, and J-P Vigneron. Tight-binding model for the electronic properties of simple hexagonal graphite. *Physical Review B*, 44(24):13237, 1991.

[127] Y Xu, X Li, and J Dong. Infrared and Raman spectra of AA-stacking bilayer graphene. *Nanotechnology*, 21(6):065711, 2010.

[128] J Slater and G Koster. Simplified LCAO method for the periodic potential problem. *Physical Review*, 94(6):1498, 1954.

[129] N Leconte, S Javvaji, J An, A Samudrala, and J Jung. Relaxation effects in twisted bilayer graphene: A multiscale approach. *Physical Review B*, 106(11):115410, 2022.

[130] R Dillon, I Spain, and J McClure. Electronic energy band parameters of graphite and their dependence on pressure, temperature and acceptor concentration. *Journal of Physics and Chemistry of Solids*, 38(6):635–645, 1977.

[131] E Economou. *Green's functions in quantum physics*, volume 7. Springer Science & Business Media, 2006.

[132] MP L Sancho, JM L Sancho, and J Rubio. Quick iterative scheme for the calculation of transfer matrices: Application to Mo (100). *Journal of Physics F: Metal Physics*, 14(5):1205, 1984.

[133] C Caroli, R Combescot, P Nozieres, and D Saint-James. Direct calculation of the tunneling current. *Journal of Physics C: Solid State Physics*, 4(8):916, 1971.

[134] K Wang, W Ouyang, W Cao, M Ma, and Q Zheng. Robust superlubricity by strain engineering. *Nanoscale*, 11(5):2186–2193, 2019.

[135] J Perdew, K Burke, and M Ernzerhof. Generalized gradient approximation made simple. *Physical Review Letters*, 77(18):3865, 1996.

[136] W Tao, G Qing, L Yan, and S Kuang. A comparative investigation of an AB- and AA-stacked bilayer graphene sheet under an applied electric field: A density functional theory study. *Chinese Physics B*, 21(6):067301, 2012.

[137] J-K Lee, S-C Lee, J-P Ahn, S-C Kim, J Wilson, and P John. The growth of AA graphite on (111) diamond. *The Journal of Chemical Physics*, 129(23):234709, 2008.

[138] J R Dahn, R Fong, and M J Spoon. Suppression of staging in lithium-intercalated carbon by disorder in the host. *Physical Review B*, 42(10):6424, 1990.

[139] S-M Choi, S-H Jhi, and Y-W Son. Controlling energy gap of bilayer graphene by strain. *Nano Letters*, 10(9):3486–3489, 2010.

[140] H Raza. Edge and passivation effects in armchair graphene nanoribbons. *Physical Review B*, 84(16):165425, 2011.

[141] K Nakada, M Fujita, G Dresselhaus, and M Dresselhaus. Edge state in graphene ribbons: Nanometer size effect and edge shape dependence. *Physical Review B*, 54(24):17954, 1996.

[142] M Fujita, K Wakabayashi, K Nakada, and K Kusakabe. Peculiar localized state at zigzag graphite edge. *Journal of the Physical Society of Japan*, 65(7):1920–1923, 1996.

[143] K Wakabayashi, M Fujita, H Ajiki, and M Sigrist. Electronic and magnetic properties of nanographite ribbons. *Physical Review B*, 59(12):8271, 1999.

[144] L Gong, R Young, I Kinloch, I Riaz, R Jalil, and K Novoselov. Optimizing the reinforcement of polymer-based nanocomposites by graphene. *ACS Nano*, 6(3):2086–2095, 2012.

[145] D. Efimkin and A MacDonald. Helical network model for twisted bilayer graphene. *Physical Review B*, 98:035404, 2018.

[146] J A Crosse. Strain-dependent conductivity in biased bilayer graphene. *Physical Review B*, 90(23):235403, 2014.

[147] J Oostinga, H Heersche, X Liu, A Morpurgo, and L Vandersypen. Gate-induced insulating state in bilayer graphene devices. *Nature Materials*, 7(2):151–157, 2008.

[148] Y Zhang, T-T Tang, C Girit, Z Hao, M Martin, A Zettl, M Crommie, R Shen, and F Wang. Direct observation of a widely tunable bandgap in bilayer graphene. *Nature*, 459(7248):820–823, 2009.

[149] J Li, K Wang, K McFaul, Z Zern, Y Ren, K Watanabe, T Taniguchi, Z Qiao, and J Zhu. Gate-controlled topological conducting channels in bilayer graphene. *Nature Nanotechnology*, 11(12):1060–1065, 2016.

[150] P Rickhaus, J Wallbank, S Slizovskiy, R Pisoni, H Overweg, Y Lee, M Eich, M-H Liu, K Watanabe, T Taniguchi, T Ihn, and K Ensslin. Transport through a network of topological channels in twisted bilayer graphene. *Nano Letters*, 18(11):6725–6730, 2018.

[151] Florie Mesple, Niels R Walet, Guy Trambly de Laissardière, Francisco Guinea, Djordje Došenović, Hanako Okuno, Colin Paillet, Adrien Michon, Claude Chape-

lier, and Vincent T Renard. Giant atomic swirl in graphene bilayers with biaxial heterostrain. *Advanced Materials*, 35(41):2306312, 2023.

[152] N Nam and M Koshino. Lattice relaxation and energy band modulation in twisted bilayer graphene. *Physical Review B*, 96:075311, 2017.

[153] J Lin, W Fang, W Zhou, A Lupini, J C Idrobo, J Kong, S Pennycook, and S Pantelides. AC/AB stacking boundaries in bilayer graphene. *Nano Letters*, 13(7):3262–3268, 2013.

[154] S Jain, V Juričić, and G Barkema. Structure of twisted and buckled bilayer graphene. *2D Materials*, 4(1):015018, 2016.

[155] N Georgoulea, S Power, and N Caffrey. Strain-induced stacking transition in bilayer graphene. *Journal of Physics: Condensed Matter*, 34(47):475302, 2022.

[156] A Parhizkar and V Galitski. Strained bilayer graphene, emergent energy scales, and Moiré gravity. *Physical Review Research*, 4(2):L022027, 2022.

[157] N Georgoulea, N Caffrey, and S Power. One-dimensional topological channels in heterostrained bilayer graphene. *Physical Review B*, 109(3):035403, 2024.

[158] F Liu, P Ming, and J Li. Ab initio calculation of ideal strength and phonon instability of graphene under tension. *Physical Review B*, 76(6):064120, 2007.

[159] G Gui, J Li, and J Zhong. Band structure engineering of graphene by strain: First-principles calculations. *Physical Review B*, 78(7):075435, 2008.

[160] L Zhou, Y Wang, and G Cao. Elastic properties of monolayer graphene with different chiralities. *Journal of Physics: Condensed Matter*, 25(12):125302, 2013.

[161] J A Sánchez-Sánchez, M Navarro-Espino, Y Betancur-Ocampo, J E Barrios-Vargas, and T Stegmann. Steering the current flow in twisted bilayer graphene. *Journal of Physics: Materials*, 5(2):024003, 2022.

[162] P Jadaun, B Sahu, L Register, and S Banerjee. Density functional theory studies of interactions of graphene with its environment: Substrate, gate dielectric and edge effects. *Solid state communications*, 152(15):1497–1502, 2012.

[163] F Gargiulo and O Yazyev. Structural and electronic transformation in low-angle twisted bilayer graphene. *2D Materials*, 5(1):015019, 2017.

[164] S Carr, D Massatt, S Torrisi, P Cazeaux, M Luskin, and E Kaxiras. Relaxation and domain formation in incommensurate two-dimensional heterostructures. *Physical Review B*, 98:224102, 2018.

[165] F Zahid, L Liu, Y Zhu, J Wang, and H Guo. A generic tight-binding model for monolayer, bilayer and bulk MoS_2. *Aip Advances*, 3(5), 2013.